UNIVERSITÀ DI PARMA

UNIVERSITA' DEGLI STUDI DI PARMA

DOTTORATO DI RICERCA IN

SCIENZE DELLA TERRA

CICLO XXXIV

MANTLE HETEROGENEITIES IN RIFTING-RELATED AND SUPRA-SUBDUCTION SETTINGS: EXAMPLES FROM EXTERNAL LIGURIAN AND NEW CALEDONIA OPHIOLITES

Coordinatore:

Chiar.mo Prof. Marco Roveri

Tutore:

Chiar.ma Prof.ssa Alessandra Montanini

Co-Tutore:

Chiar.mo Prof. Riccardo Tribuzio

Dottorando: Elisa Ferrari

Anni Accademici 2018/2019 – 2020/2021

Index

Chapter 1

1.1. Introduction: contents and aims of the Thesis

The notion of mantle heterogeneity has become entrenched in the scientific community since the pioneering studies in the 1960s, which evidenced geochemical and isotopic variabilities in the oceanic basalts, one of the main products of mantle melting (Hedge and Walthall, 1963; Gast et al., 1964; Tatsumoto et al., 1965; Schilling and Winchester, 1967, 1969; Gast, 1968; Hart, 1971). Studying Mid-Ocean Ridge Basalts (MORB) and Ocean Island Basalts (OIB) has always been a widely used method to characterize mantle sources, although it is an indirect investigation approach. A direct approach is represented by sampling mantle rocks from the ocean floor, by dredging or drilling, and ophiolitic exposures, besides analysing mantle xenoliths.

Mantle heterogeneities are generally explained by the presence of pyroxenite and eclogite layers, which, to a large extent, could derive from processes of crustal recycling into the mantle (i.e., subduction and lithospheric delamination). The guiding theme of this PhD Thesis is the creation of geochemical and isotopic heterogeneities in mantle sequences from distinct geodynamic settings, in particular from rifting-related and young supra-subduction settings. Specific petrogenetic processes act in these different environments: while lithospheric extension and asthenosphere upwelling dominate the rifting-related setting, production of melts from variably depleted mantle sources modified by slab-derived components are believed to characterize the subduction onset.

Two distinct ophiolitic exposures are considered in the present study: the External Ligurian ophiolites, chosen as an example of rifting-related mantle section and the New Caledonia ophiolite, chosen as an example of supra-subduction zone mantle section.

Chapter 2 and Chapter 3 illustrate the External Ligurian case study. In particular, the main objectives of Chapter 2 are: (i) to describe the petrographic, petrological and geochemical characteristics of two poorly known mantle bodies (Monte Gavi and Monte Sant'Agostino), and (ii) to provide new insights into the behaviour of the External Ligurian subcontinental mantle during the Mesozoic rifting phase. The contents of Chapter 2 represent a paper already published: *Ferrari E., Montanini A., Tribuzio R., 2022. Rifting evolution of the lithospheric subcontinental mantle: New insights from the External Ligurian ophiolites (Northern Apennine, Italy). Lithos, 410-411: 106571*. The article is reported unchanged in the Thesis, except for the layout. Chapter 3 focuses on: (i) the melt-rock reaction process recorded by Monte Gavi mantle body, and (ii) the origin of the impregnating melt.

Chapter 4 illustrates the New Caledonia case study. The main purpose is to define the compositions of the melts percolating the forearc mantle during the subduction initiation.

1.2. References

Gast P.W., 1968. Trace element fractionation and the origin of tholeiitic and alkaline magma types. Geochimica et Cosmochimica Acta, 32:1057-1086

Gast P.W., Tilton G.R., Hedge C., 1964. Isotopic composition of lead and strontium from Ascension and Gough Islands. Science, 145:1181-1185

Hart S.R., 1971. K, Rb, Cs, Sr, Ba contents and Sr isotope ratios of ocean floor basalts. Philosophical Transactions of the Royal Society Series A, 268:573-587

Hedge C.E., Walthall F.G., 1963. Radiogenic strontium 87 as an index of geological processes. Science, 140:1214-1217

Schilling J.G., Winchester J.W., 1967. Rare-earth fractionation and magmatic processes. Mantles of Earth and Terrestrial Planets, 267-283, Runcon SK, London: Interscience Publishers

Schilling J.G., Winchester J.W., 1969. Rare earth contribution to the origin of Hawaiian lavas. Contributions to Mineralogy and Petrology, 40:231

Tatsumoto M., Hedge C.E., Engel A.E.J., 1965. Potassium, rubidium, strontium, thorium, uranium, and the ratio of strontium-87 to strontium-86 in oceanic tholeiitic basalt. Science, 150:886-888

Chapter 2
Rifting evolution of the lithospheric subcontinental mantle: New insights from the External Ligurian ophiolites (Northern Apennine, Italy)

2.1. Introduction

Magma-poor ocean-continent transitions (OCT), such as those exposed along the Iberia-Newfoundland (e.g., Whitmarsh et al., 2001) and the Australian-Antarctic systems (e.g., McCarthy et al., 2020), are characterized by wide areas of subcontinental mantle uplifted and denuded in conjunction with the late-stage rifting evolution. A key point to elucidate the rifting process leading to basin opening is therefore the tectonic, magmatic and metamorphic evolution of the subcontinental lithospheric mantle. In particular, limited direct information are available on the high temperature shearing and mode of mantle exhumation before the late coupling stage, where brittle faults cut through the extremely thinned continental crust and penetrate into the underlying mantle (Sutra and Manatschal, 2012). Samples drilled or dredged along modern OCTs testify the occurrence of heterogeneous subcontinental lithospheric mantle, which preserves geochemical signatures acquired before onset of rifting, as well as evidence for syn-rift melt-rock interaction and deformation (e.g., Chazot et al., 2005; Müntener and Manatschal, 2006). However, the relatively limited sampling compared with the regional extent of the involved areas, and the diffuse alteration of the recovered samples hampered to envisage a conceptual model for the mantle behaviour from the beginning of lithospheric thinning to crustal breakup.

Fragments of magma-poor ocean-continent transitions of Jurassic age are exposed along the Alpine-Apennine belt (e.g., Manatschal and Müntener, 2009). These fossil records provided relevant information about the rifting-related history undergone by the subcontinental mantle during lithosphere thinning and exhumation (e.g., Picazo et al., 2016). For instance, the investigation of the Platta ophiolites from Central Alps documented that the subcontinental mantle was percolated and refertilized by MORB-type melts during rifting (e.g., Müntener et al., 2010). In addition, the central body of the Lanzo mantle massif from Western Alps provides evidence for melt focusing within rifting-related plagioclase-facies shear zones (Kaczmarek and Müntener, 2010; Kaczmarek and

Tommasi, 2011). The subcontinental mantle bodies from the External Ligurian units (Northern Apennines, Fig. 1) are also part of a Jurassic magma-poor ocean-continent transition (Marroni et al., 1998). Despite some of these mantle bodies were thoroughly investigated from petrological, geochemical and microstructural viewpoints (e.g., Borghini et al., 2016; Hidas et al., 2020; Montanini et al., 2006; Rampone et al., 1995), a comprehensive rifting-related geological scenario is lacking for the External Ligurian mantle section.

The primary aim of this contribution is to provide new constraints on the evolution of the subcontinental mantle involved in a rifting process. We thus present new field, microstructural, mineral chemistry and geothermobarometric data obtained for peridotites and enclosed pyroxenites from kilometre-sized subcontinental mantle bodies from the External Ligurian units, locally recognized as Monte Gavi and Monte Sant'Agostino. To our knowledge, no petrographic and petrological data are available in the literature for these mantle sections. We document that the different mantle bodies from the External Ligurian units display distinct tectonic and thermal evolutions in the plagioclase stability field. Hence, we relate the heterogeneous behaviour of the subcontinental mantle under relatively low pressure conditions to the rifting process that ultimately developed a magma-poor Jurassic OCT. A comparison with ophiolitic mantle sections from the Alpine belt finally allowed us to shed light on the rifting-related evolution of the subcontinental lithospheric mantle at a regional scale.

2.2. Geological setting

The ophiolitic bodies exposed along the Alpine-Apennine belt are lithospheric remnants of the Western Tethys (or Ligurian-Piedmontese basin). This basin formed in the Middle to Upper Jurassic in conjunction with the opening of the Central Atlantic Ocean and separated the Europe-Iberia from the Africa-Adria plate (e.g. Schettino and Turco, 2011). The opening of Western Tethys basin was associated with uplift and denudation of subcontinental lithospheric mantle, which is presently exposed along the Alpine-Apennine belt. During rifting and oceanization, the subcontinental lithospheric mantle most likely underwent thermochemical erosion driven by reaction with ascending melts of asthenospheric origin (e.g., Müntener et al., 2010; Piccardo et al., 2004, 2007; Rampone et al., 2020).

The Alpine-Apennine ophiolites are locally associated with continental crust material and frequently include mantle sections retaining a subcontinental origin (e.g., Manatschal and Müntener, 2009; Marroni et al., 1998). The best examples of preserved subcontinental mantle were reported for the Malenco-Totalp bodies from Central Alps (Müntener et al., 2004, 2010) and for the External Ligurian units from the Northern Apennine (e.g., Montanini et al., 2006, 2012; Rampone et al., 1995).

The ophiolites comprising subcontinental mantle sections were interpreted as remnants of embryonic oceanic lithosphere formed at magma-poor ocean-continent transitions, similar to those occurring along the Iberia-Newfoundlands margins (e.g., Manatschal and Müntener, 2009). Conversely, some of the ophiolites from the Alpine-Apennine belt display structural and compositional similarities to oceanic lithosphere from slow and ultra-slow spreading ridges (Sanfilippo and Tribuzio, 2011; Tribuzio et al., 2014).

The External Ligurian ophiolites occur as large slide-blocks within sedimentary melanges related to inception of convergence-related sedimentation in Upper Cretaceous times (Marroni et al., 1998, 2017). In these ophiolites, exhumed subcontinental mantle (Montanini et al., 2006; Rampone et al., 1995) is in places associated with MOR-type gabbroic and basaltic rocks (Montanini et al., 2008; Tribuzio et al., 2004, 2016). In particular, the basalts and associated Middle to Upper Jurassic pelagic sediments are locally in primary contact relationships with granitoids of late Carboniferous-early Permian age. The mantle bodies and the continental crust rocks record retrograde tectono-metamorphic evolutions related to the rifting process that led to their exposure at the seafloor in the Middle Jurassic (see also Renna and Tribuzio, 2009).

The External Ligurian mantle bodies are up to few km in size (Fig. 2.1). Petrological and geochemical studies were carried out on few slide-blocks located in the western (Suvero, Monte Nero, Monte Ragola) and in the eastern sectors (Rio Strega-Monte Prinzera) of the External Ligurian units. The mantle bodies typically consist of chemically fertile spinel-plagioclase lherzolites with disseminated Ti-rich amphibole, and widespread pyroxenite layers (e.g., Montanini et al., 2006; Rampone et al., 1995). The lherzolites mainly display a MORB-type Nd–Hf isotope signature. However, highly radiogenic Nd and Hf values at the time of oceanization ($\varepsilon_{Nd(160Ma)}$ = 17, $\varepsilon_{Hf(160Ma)}$ = 25), coupled with unradiogenic Sr ($^{87}Sr/^{86}Sr$ = 0.7018) and ancient Os model ages (1.6–2.1 Ga) were locally found (see Borghini et al., 2013, 2016, 2021; Montanini et al., 2012; Snow et al., 2000). The literature radiogenic isotope data collectively argue for a long residence time in the subcontinental mantle. The Suvero mantle body provides evidence for having undergone: (i) pyroxenite veining in the early Paleozoic, and (ii) rifting-related spinel- to plagioclase-facies decompression under subsolidus static conditions in the Mesozoic (see also Hidas et al., 2020). The Rio Strega-Monte Prinzera mantle bodies in places include garnet pyroxenite layers documenting a stage of deep-seated lithospheric equilibration at ~2.8 GPa and ~1100 °C, and are characterized by widespread plagioclase-facies mylonitic shear zones, which occurred under subsolidus conditions in response to the Mesozoic lithosphere extension (see also Montanini et al., 2006).

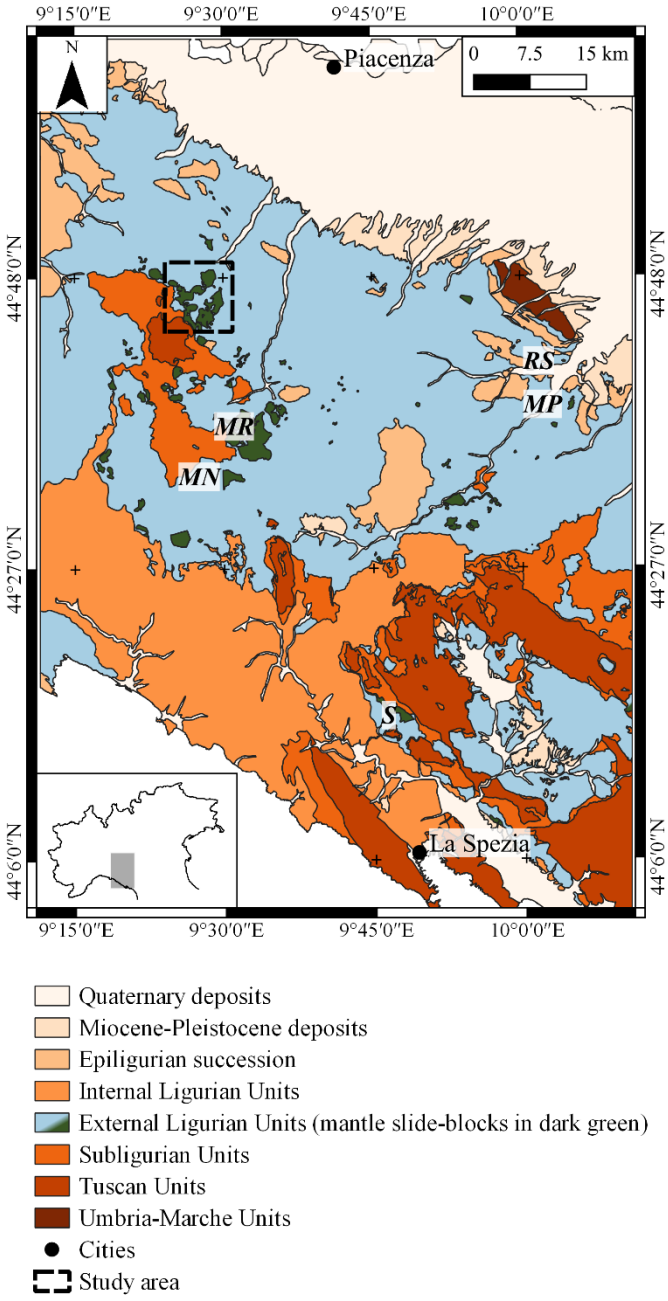

Fig. 2.1. Tectonic sketch map of the NW Apennines (modified after Conti et al., 2020). Mantle bodies investigated in previous works are also reported: MN, Monte Nero; MP, Monte Prinzera; MR, Monte Ragola; RS, Rio Strega; S, Suvero.

2.3. Field relationships

The present study focuses on the External Ligurian mantle bodies exposed between Trebbia and Perino valleys, east of Bobbio (Fig. 2.2). Here, hectometre-to kilometre-sized mantle blocks are included into a sedimentary melange, named Monte Ragola-Monte delle Tane Complex, which was formed during the inception of an intra-oceanic subduction event in the Upper Cretaceous (Marroni et al., 2017). This complex mainly consists of flyschoid sedimentary deposits composed of fine-grained clastic sequences and polymict breccias derived from gravity flows. The breccias include up to m-sized clasts of: (i) mantle-derived serpentinites, (ii) late Carboniferous-early Permian intrusive rocks, namely lower crustal gabbro-derived granulites and pyroxenites, and upper crustal granitoids, and (iii) Upper Cretaceous micritic limestones (see also Montanini and Tribuzio, 2001; Renna and Tribuzio, 2009). At the contact with the mantle body, the breccias are typically monogenic, being composed of serpentinized peridotite clasts set in a serpentine-rich clayish matrix. New field observations allowed us to distinguish two different types of mantle bodies, forming two distinct NE-SW alignments (Fig. 2.2). The first type is represented at Camminata Boselli, Monte Gavi and Monte Castello localities, which are hereafter collectively referred to as Monte Gavi mantle section. The second type is represented by the exposures of Monte Armelio, Monte Gonio, Monte Mangiapane and Monte Sant'Agostino, and are hereafter referred to as Monte Sant'Agostino mantle section.

2.3.1. Monte Gavi mantle section

These mantle bodies (Fig. 2.2) mainly consist of nearly undeformed serpentinized spinel-plagioclase peridotites including widespread spinel-plagioclase pyroxenite layers (Fig. 2.3a). The peridotites locally display a weak foliation defined by alignment of orthopyroxenes. The pyroxenite layers are typically <0.1 m thick. Near the northwestern contact of the Monte Gavi body with the enclosing sediments, there are several pyroxenite layers, which are up to 0.8 m thick and up to 20 m long. These layers, hereafter referred to as Type-I pyroxenites, have nearly concordant orientations and are characterized by alignment of 1-2 cm long pyroxene and spinel grains. Type-I pyroxenites include a high amount of spinel (up to ~15 vol%), which is rimmed by mm-scale plagioclase coronas (Fig. 2.3b-c) or appears to be almost completely replaced by plagioclase (Fig. 2.3d). Plagioclase also frequently occurs along the cleavages of the large pyroxenes (Fig. 2.3b) and locally develops anastomosing, subparallel veinlets that are up to 2 mm thick. The thin pyroxenite layers, hereafter referred to as Type-II pyroxenites, exhibit pyroxene and spinel alignment subparallel to the pyroxenite-peridotite contacts. Spinel is typically absent in the outermost portions of the Type-II pyroxenite layers.

2.3.2 Monte Sant'Agostino mantle section

Monte Sant'Agostino and the neighbouring mantle bodies (Fig. 2.2) are mostly composed of variably serpentinized, spinel-plagioclase foliated peridotites. They include porphyroclasts of dark green pyroxene (up to 1 cm across) and 1–2 mm-sized black spinel, which are set in a fine-grained olivine-rich matrix. According to Passchier and Trouw (2005), their textures vary from protomylonitic (porphyroclasts >50 vol%, Fig. 2.3e, 2.4b) to mylonitic (porphyroclasts 10–50 vol%, Fig. 2.4c) and ultramylonitic (porphyroclasts <10 vol%, Fig. 2.3f). The size of the porphyroclasts decreases from protomylonitic (~5-10 mm) to ultramylonitic peridotites (~0.25-1.5 mm). At Monte Sant'Agostino, the thickness of the ultramylonitic shear zone is estimated to be at least ~150 m. Up to 1 cm thick, stretched pyroxene-rich bands are locally present in the ultramylonites, whereas up to 8-10 cm thick, typically boudinaged, pyroxenite layers are frequent in the protomylonitic domains (Fig. 2.3e).

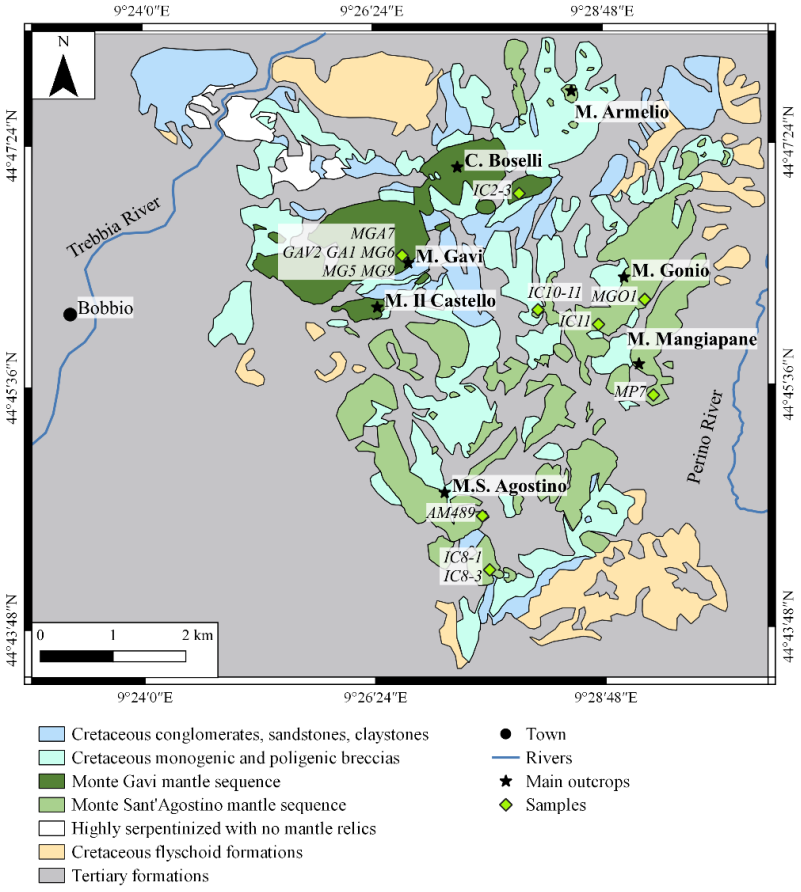

Fig. 2.2. Geological sketch map of the study area (modified after Elter et al., 1997) and location of the investigated samples.

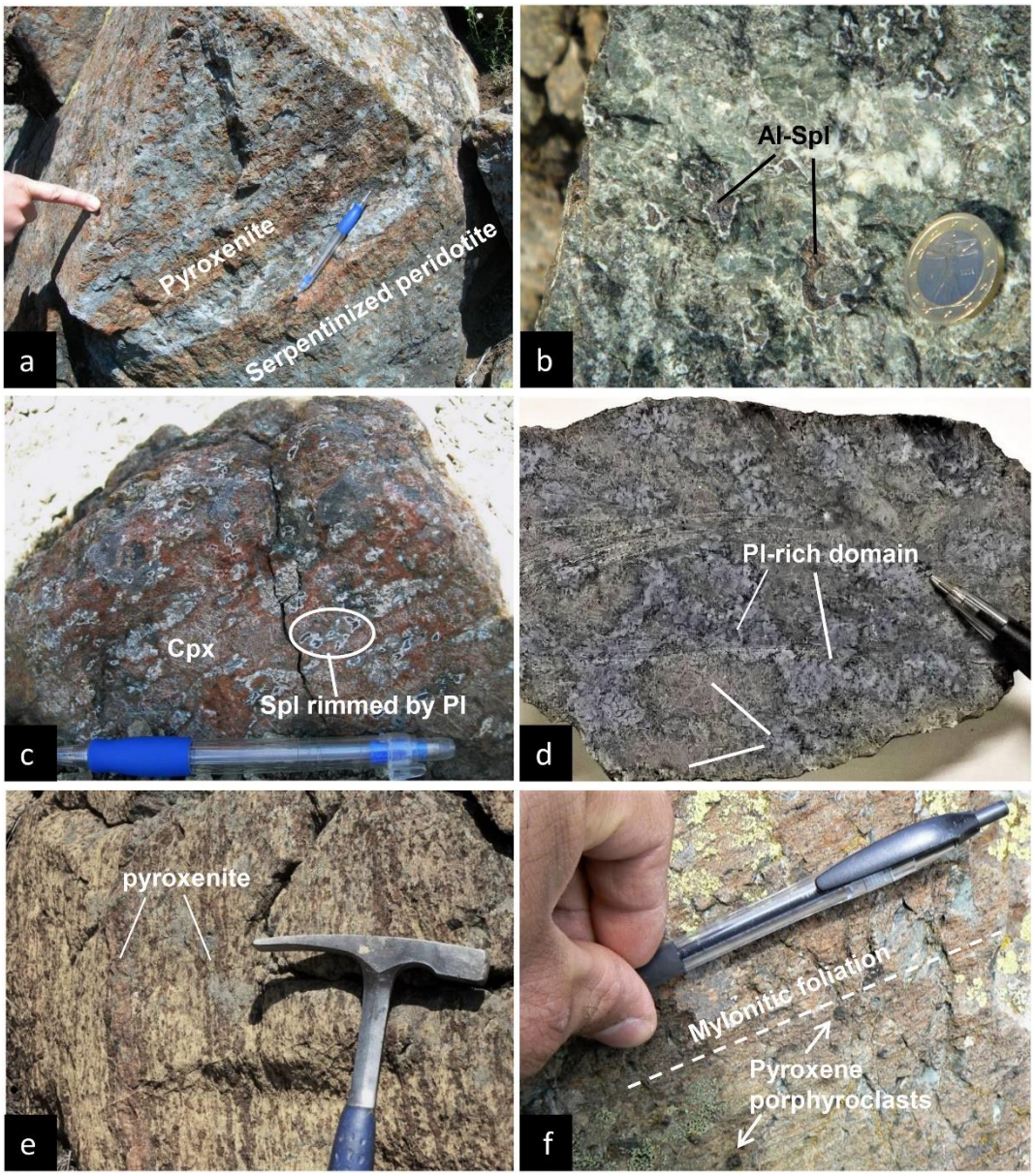

Fig. 2.3. Monte Gavi: (a) cm-scale pyroxenite layers; (b) coarse Al-Spl rimmed by plagioclase and (c) coarse clinopyroxene with plagioclase lamellae in Type-Ia pyroxenite; (d) pyroxene-rich and plagioclase-rich domains in Type-Ib pyroxenite. Monte Sant'Agostino: (e) peridotite protomylonite with boudinaged pyroxenite layers, (f) peridotite ultramylonite.

2.4. Petrographic characteristics and major element mineral chemistry

Microstructural observations were carried out on thirty-five rock samples. A summary of microstructural and mineralogical characteristics of the investigated rocks is reported in Table 2.1. Fourteen samples, whose location is shown in Fig. 2.2, were selected for major element mineral analyses (Tables 2.2-2.3-2.4). The Monte Gavi samples include one partially serpentinized peridotite (MGA7), three Type-I pyroxenites (GAV2, GA1 and MG6) and three Type-II pyroxenites (MG5, MG9, IC2/3). Samples selected for the Monte Sant'Agostino mantle section comprise four mylonitic lherzolites (MGO1, IC8–1, IC8–3, IC11) and three pyroxenites (MP7, AM489, IC10–11). The modal abundances reported in the following petrographic descriptions were visually estimated.

2.4.1. Monte Gavi peridotites

The Monte Gavi peridotites are spinel-plagioclase harzburgites, typically widely serpentinized. The least serpentinized samples are nearly isotropic and characterized by 1–2 cm long exsolved orthopyroxenes and minor amounts of clinopyroxene (5–10 vol%) and plagioclase (~5 vol%). Plagioclase occurs in two microstructural sites: (1) coronas mantling dark brown Cr-rich spinel, and (2) patches or lamellae, associated with orthopyroxene, partially replacing clinopyroxene (Fig. 2.5a). Plagioclase is altered into fine-grained aggregates of epidote + chlorite + hydrogrossular. Olivine has 90 mol% forsterite and 0.4–0.5 wt% NiO. Orthopyroxene has 89 Mg# [100 × Mg/(Mg + Fe_{tot})] and displays a core to rim decrease of Al_2O_3 and CaO, from ~6.0 wt% to ~3.1 wt% and from 1.2 to 0.8 wt%, respectively. Clinopyroxene exhibits a core to rim Mg# increase (88–89 to 90–91) and Al_2O_3 decrease (5.9–7.4 wt% to 3.5–5.1 wt%), and nearly homogeneous Na_2O contents (0.7–1.0 wt%, Fig. 2.6). Spinel has relatively high Cr# [100 × Cr/(Cr + Al)] of 33–35, and 0.3–0.5 wt% TiO_2 (Fig. 2.7).

2.4.2. Monte Gavi Type-I pyroxenites

We subdivide the Type-I pyroxenites into two sub-types, based on different extents of replacement of coarse clinopyroxene and spinel grains. Type-Ia pyroxenites, exemplified by sample GAV2, have ~1.5 cm long crystals of clinopyroxene and green spinel (Fig. 2.3b). The coarse clinopyroxene includes plagioclase and orthopyroxene along the original cleavages, with the physically associated clinopyroxene displaying embayed boundaries (Fig. 2.5b). The coarse clinopyroxene has 84–87 Mg# and exhibits a substantial outward Al_2O_3 decrease (~8.7 to ~4.6 wt%). The core locally has relatively low TiO_2 contents (0.4–0.5 wt%), which typically increase towards the rims (up to ~0.9 wt%, Fig. 2.8). The coarse clinopyroxene is mantled by aggregates made up of secondary clinopyroxene, altered orthopyroxene and minor altered plagioclase. The secondary clinopyroxene has 85–88 Mg#, core to rim Al_2O_3 decrease (from ~7.8 to ~4.7 wt%) and nearly

homogeneous TiO_2 (0.7–0.9 wt%). The coarse green spinels (Cr# = 2–4, TiO_2 < 0.10 wt%) are rimmed by 1–2 mm thick plagioclase coronas (Fig. 2.5c). The selected sample also includes smaller, submillimetre to millimetre-scale spinel grains with dark brown colour and embayed shape, rimmed by up to 1 cm wide aggregates made up of altered plagioclase and minor olivine (Fig. 2.4a). These spinels have variable and significantly higher Cr# (12–34) and TiO_2 (0.15–1.02 wt%). Notably, minor amounts of relatively large chlorite grains displaying prismatic shape and ghost cleavages, presumably representing pseudomorphs after orthopyroxene, are also present. Hence, we envision that the original mineral assemblage of these pyroxenites was mostly composed of clinopyroxene, associated with minor amounts of Al-spinel and orthopyroxene.

Type-Ib pyroxenites (samples GA1 and MG6) are characterized by the occurrence of distinct pyroxene- and plagioclase-bearing domains, which are both up to 2 cm long (Fig. 2.3d). The pyroxene-rich domains are composed of clinopyroxene (40–50 vol%), orthopyroxene (35–40 vol%) and minor plagioclase (15–20 vol%), and locally include relics of pre-existing coarse clinopyroxenes (Fig. 2.5d). Thick plagioclase + orthopyroxene lamellae are present along the cleavages of these coarse clinopyroxenes, typically forming symplectitic intergrowths (Fig. 2.5e). The coarse clinopyroxene has relatively low Mg# (79–84) and variable Al_2O_3 (5.2–9.7 wt%), TiO_2 (1.2–2.3 wt%) and Na_2O (0.4–1.7 wt%), with no clear systematic zoning (Fig. 2.8). The chemical compositions of the secondary clinopyroxenes associated with plagioclase and orthopyroxene fall within these intervals. Orthopyroxene has low Mg# (81–83), 1.9–3.7 wt% Al_2O_3, 0.6–1.3 wt% CaO and relatively high TiO_2 (0.3–0.5 wt%). Accessory brown amphibole (titanian pargasite according to the nomenclature of Leake et al., 1997) occurs as thin rims mantling resorbed clinopyroxenes and has 76–80 Mg# and 2.7–3.8 wt% TiO_2. The plagioclase-rich domains include ~30 vol% olivine and, in their inner portions, accessory amounts of small spinel grains with brownish-black colour (Fig. 2.5f). Plagioclase (71–79 mol% anorthite) and olivine (82–83 mol% forsterite) form nearly polygonal aggregates and are variably altered into sericite and serpentine, respectively. Spinel within the plagioclase-rich domain has variable Cr# (4–30) and TiO_2 (0.10–0.56 wt %, Fig. 2.7). Tiny ilmenite and altered Fe-Ni-Cu sulfides with rounded morphology are also in places present within plagioclase. Towards the contact with the pyroxene-rich domains, coarse-grained vermicular olivine + plagioclase intergrowths typically occur.

2.4.3. Monte Gavi Type-II pyroxenites

Type-II pyroxenites are medium- to coarse-grained olivine websterites. They display moderate to extensive serpentinization, which makes in places difficult to decipher their primary texture. However, in the most preserved samples, an allotriomorphic granular texture is discernible. Their

original mineral assemblage is composed of clinopyroxene (30–40 vol%), orthopyroxene (25–30 vol%), olivine (up to 25 vol%), greenish to brown spinel (5–10 vol%) and plagioclase (10–15 vol %). These pyroxenites are characterized by the presence of exsolved orthopyroxene porphyroclasts, forsterite-rich (89 mol%) olivine (Fig. 2.5g) that is locally kinked, and clinopyroxene-rich domains. These domains consist of irregularly shaped clinopyroxene grains with plagioclase + orthopyroxene lamellae (Fig. 2.5h), associated with interstitial plagioclase and trails of elongated spinels rimmed by plagioclase.

Clinopyroxene from Type-II pyroxenites has 88–90 Mg#, relatively high Cr_2O_3 (0.4–0.9 wt%) and a wide TiO_2 range (0.7–1.8 wt%; Figs. 2.8 and 2.9). Al_2O_3 and Na_2O in clinopyroxene vary from 4.5 to 7.4 wt% and from 0.5 to 0.9 wt%, respectively. Orthopyroxene displays high Mg# (87–89), 4.0–5.8 wt% Al_2O_3 and 0.6–1.0 wt% CaO. Spinel has variable Cr# (6–16) and 0.1–0.6 wt% TiO_2 (Fig. 2.7). Plagioclase is in most places replaced by sericite, but small preserved domains with ~65 mol% anorthite were found in sample IC2/3. Accessory brown amphibole (titanian pargasite) occurs as rim around pyroxenes and is characterized by 85–87 Mg# and 3.1–4.0 wt% TiO_2.

2.4.4. Monte Sant'Agostino deformed peridotites

The Monte Sant'Agostino peridotites mostly consist of plagioclase-facies mylonitic lherzolites including small (cm- to dm-sized) domains made up of spinel-facies tectonites. Microstructural evidence for a spinel-facies recrystallization event are preserved in these low-strain domains (Fig. 2.10a), where up to 1 cm in size porphyroclasts of clinopyroxene and orthopyroxene are surrounded by fine-grained granoblastic aggregates made up of pyroxenes + light brown spinel ± orange-brown amphibole. Mutual exsolutions are displayed by the orthopyroxene and the clinopyroxene porphyroclasts (Fig. 2.10a-b), and the overall clinopyroxene mode varies between 10 and 15 vol%. In the less serpentinized samples, mm-sized olivine porphyroclasts surrounded by neoblastic olivine are still recognizable. Holly leaf brown spinels are also locally preserved.

The spinel-facies assemblage is widely overprinted by a plagioclase-facies mylonitic fabric. The mylonite microstructure is characterized by porphyroclasts of orthopyroxene and clinopyroxene aligned along the foliation (Fig. 2.10b–c). Cr-spinel and rare brown amphibole may also occur as porphyroclasts. Porphyroclastic orthopyroxene typically displays up to ~10 aspect ratio (Fig. 2.10c). Porphyroclastic clinopyroxene is smaller and more equant than associated porphyroclastic orthopyroxene. Both pyroxene porphyroclasts provide evidence for deformation, like undulose extinction, bending and kinking, and are set into a polyphase olivine-rich matrix with extremely fine grain-size (20–50 μm, Fig. 2.10b-c-d). Besides olivine, this matrix includes neoblastic clinopyroxene and orthopyroxene, plagioclase and, in places, Cr-spinel. Plagioclase also occurs as thin rims mantling

the spinel porphyroclasts. The extremely fine-grained matrix is dominant in the ultramylonites (Fig. 2.10e), which contain sporadic pyroxene and brown amphibole porphyroclasts with rounded shape (Table 2.3).

Both porphyroclastic and matrix olivine have 89–90 mol% forsterite and 0.4–0.5 wt% NiO. Porphyroclastic clinopyroxene has 90–91 Mg# and high Al_2O_3 and Na_2O contents (7.0–8.4 wt% and 1.6–2.1 wt%, respectively), slightly decreasing from the core to the rim (Fig. 6). Clinopyroxene neoblasts have higher Mg# values (91–92) and lower Al_2O_3 and Na_2O (2.3–3.2 and ~0.6 wt%, respectively) than porphyroclasts (see also Fig. 2.6). Orthopyroxene porphyroclasts have 89–90 Mg#, 4.4–5.6 wt% Al_2O_3 and 0.7–0.9 wt% CaO. The tiny orthopyroxene from the mylonitic matrix is distinct in the low Al_2O_3 (0.5–2.4 wt%) and CaO (0.25–0.36 wt%). Spinel has low Cr# (9–16) and $TiO_2 \leq 0.20$ wt% (Fig. 2.7). Plagioclase in the mylonitic matrix has 38–50 mol% anorthite. Porphyroclastic amphibole is titanian pargasite, with 84–86 Mg# and 3.1–4.6 wt% TiO_2. Accessory amphibole with relatively low TiO_2 (~1.8 wt%, Table 2.3) is also present in the matrix of the ultramylonites.

2.4.5. Monte Sant'Agostino spinel-plagioclase websterites

These pyroxenites typically have protomylonitic texture (Fig. 2.10f-g). Porphyroclasts of exsolved clinopyroxene and orthopyroxene (up to 0.5 cm in size), and of Al-spinel are set into a fine-grained neoblastic matrix displaying an average grain size of ~0.1 mm (Fig. 2.10f-g). Comparable amounts of clinopyroxene and orthopyroxene porphyroclasts are generally observed. The clinopyroxene porphyroclasts (Fig. 2.10g) locally display thin exsolution lamellae of orthopyroxene ± plagioclase, and the orthopyroxene porphyroclasts are frequently stretched along the main foliation. The neoblastic mineral assemblage consists of clinopyroxene and orthopyroxene associated with minor to accessory amounts of green spinel, plagioclase, olivine and brown amphibole. The neoblastic minerals commonly display grain boundary alignment parallel to the mylonitic foliation. Websterite MP7 also includes rounded symplectitic domains (Fig. 2.10h) made up of vermicular Cr-poor spinel (Cr# ~1), Al-poor orthopyroxene (Al_2O_3 = 2.8–3.9 wt%) and minor plagioclase (52–54 mol% anorthite).

Taken as a whole, clinopyroxenes and orthopyroxenes have 84–88 Mg# and 83–88 Mg#, respectively (Table 2.4). Clinopyroxene porphyroclast cores have high amounts of Al_2O_3 (9–10 wt%) and, accordingly, high proportions of Ca-Tschermak substitution (up to ~15 mol%), which are coupled with 0.8–1.1 wt% Na_2O (Fig. 8). Orthopyroxene is also Al_2O_3-rich (4.9–6.8 wt%), with rather uniform CaO (0.5–0.7 wt%). For both pyroxenes, a decrease of Al_2O_3 is observed in porphyroclast rims and in neoblastic grains with respect to porphyroclastic cores. Green spinel has generally low

Cr# (< 0.15 wt% TiO_2, Fig. 2.7). Olivine and plagioclase in the mylonitic matrix have 80–88 mol% forsterite and 54–55 mol% anorthite. Brown amphibole is titanian pargasite to kaersutite with 79–83 Mg# and 3.2–5.4 wt% TiO_2.

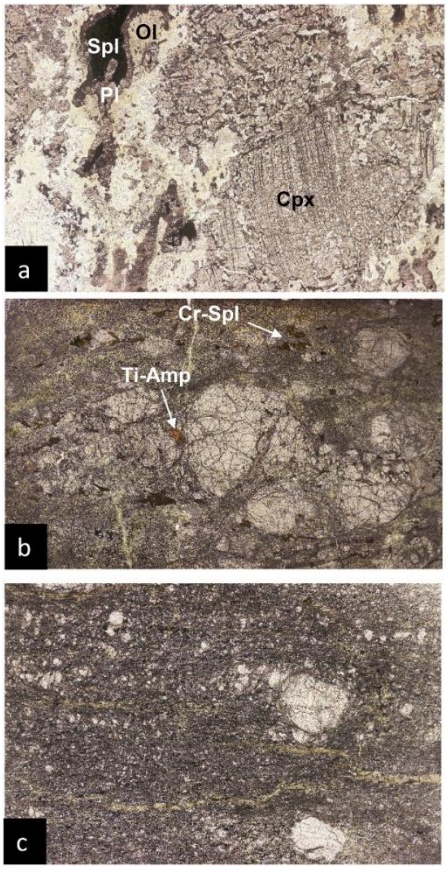

Fig. 2.4. Thin section (4.6 mm × 2.6 mm) images of: (a) Type-Ia pyroxenite (sample GAV2), (b) protomylonitic lherzolite (sample IC12–3), (c) mylonitic lherzolite (sample MGO1).

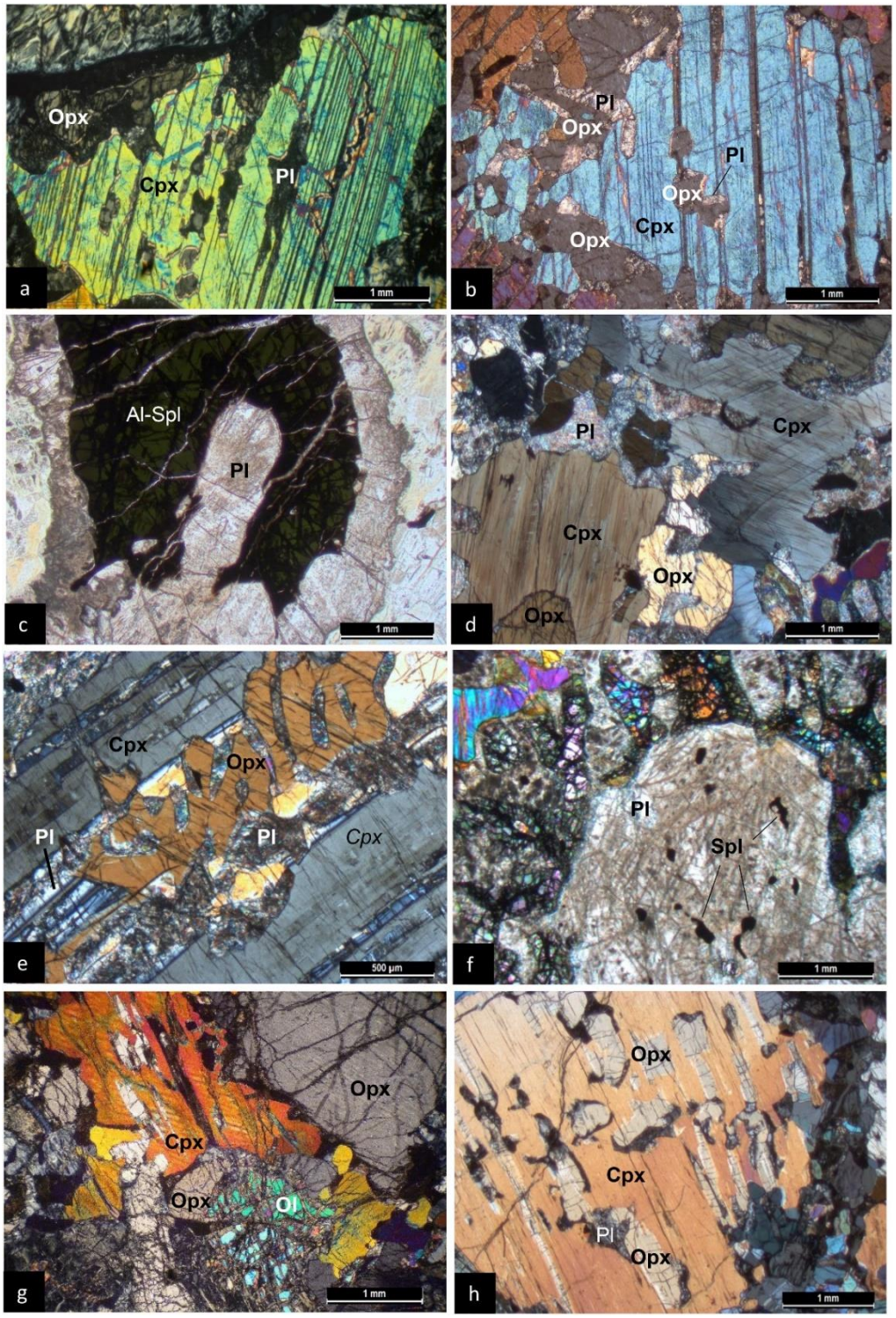

Fig. 2.5. Thin section photomicrographs under cross-polarized (a-b-d-e-f-g-h) and plane-polarized light (c) of Monte Gavi samples. (a) embayed clinopyroxene partially replaced by orthopyroxene + (altered) plagioclase, peridotite MGA7; (b) orthopyroxene + (sericitized) plagioclase replacing clinopyroxene, Type-Ia pyroxenite GAV2; (c) Al-spinel rimmed by plagioclase, Type-Ia pyroxenite GAV2; (d) pyroxene-rich domain, Type-Ib pyroxenite MG6; (e) symplectitic orthopyroxene-plagioclase intergrowth in clinopyroxene, Type-Ib pyroxenite MG6; (f) plagioclase-rich domain, Type-Ib pyroxenite GA1; (g) Mg-rich olivine, Type-II pyroxenite IC2–3; (h) Orthopyroxene and plagioclase coarse lamellae in clinopyroxene, Type-II pyroxenite IC2–3.

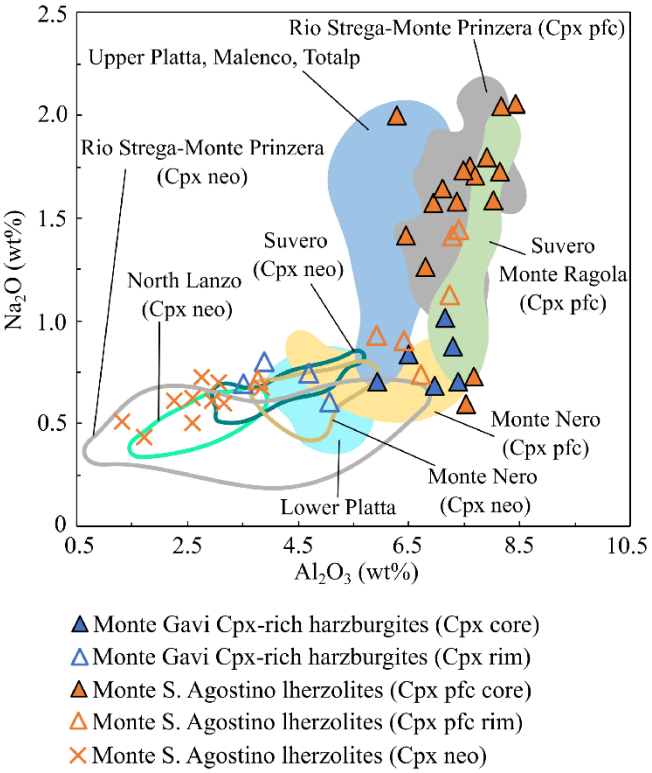

Fig. 2.6. Variation of Na_2O vs. Al_2O_3 for clinopyroxenes from Monte Gavi and Monte Sant'Agostino peridotites; pfc = porphyroclast, neo = neoblast. Data sources for other External Ligurian peridotites: Borghini et al., 2011, Borghini et al., 2013; Montanini et al. (2006); Rampone et al. (1995). North Lanzo data from Kaczmarek et al. (2008); Upper Platta, Malenco and Totalp data from Müntener et al. (2010).

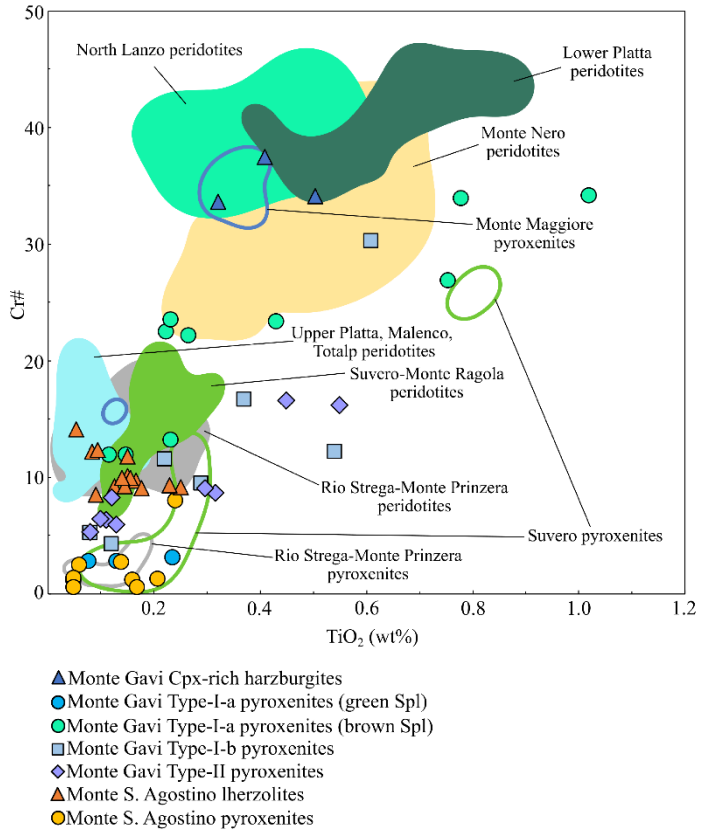

Fig. 2.7. Variation of Cr # (100 ·[Cr/(Cr + Al)]) vs. TiO2 for spinel from Monte Gavi and Monte Sant'Agostino peridotites and pyroxenites. Data sources for other External Ligurian peridotites and pyroxenites: Borghini et al. (2011, 2013, 2016); Montanini et al. (2006); Rampone et al. (1995). Data for North Lanzo peridotites from Kaczmarek and Müntener (2008); Upper Platta, Lower Platta, Malenco and Totalp peridotites after Müntener et al. (2010). Data for Monte Maggiore pyroxenites (Corsica) from Basch et al. (2019).

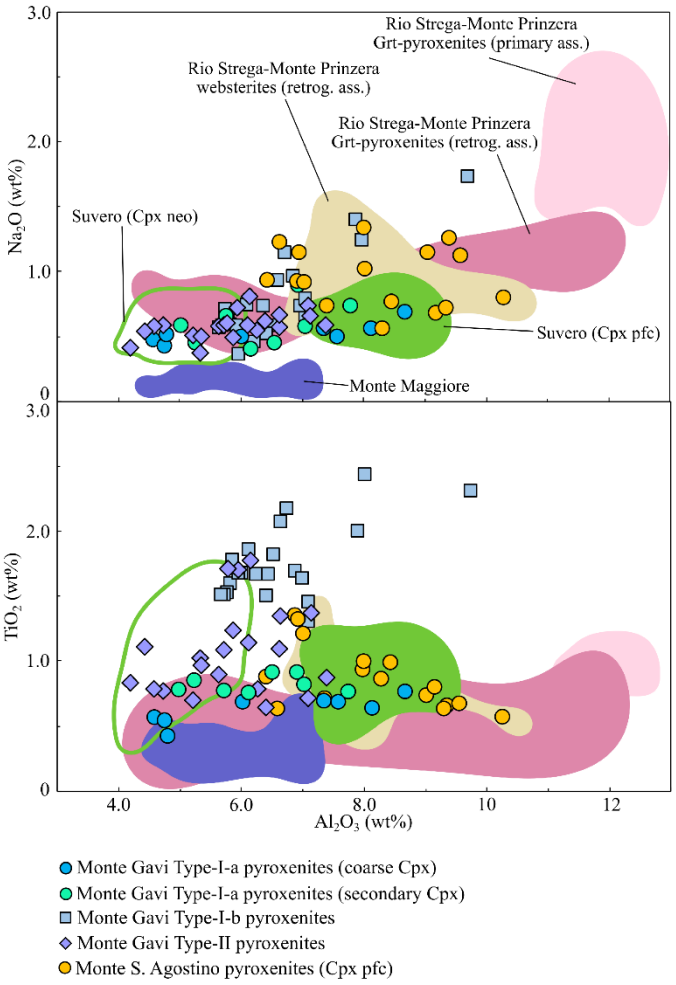

Fig. 2.8. Variation of Na_2O and TiO_2 vs. Al_2O_3 for clinopyroxenes from Monte Gavi and Monte Sant'Agostino pyroxenites; pfc = porphyroclast, neo = neoblast, 1 = cpx in primary garnet-bearing assemblage, 2 = cpx in retrograde, garnet-free assemblage. Data sources for other External Ligurian pyroxenites: Borghini et al. (2016), Montanini et al. (2006). Data for Monte Maggiore pyroxenites (Corsica) from Basch et al. (2019).

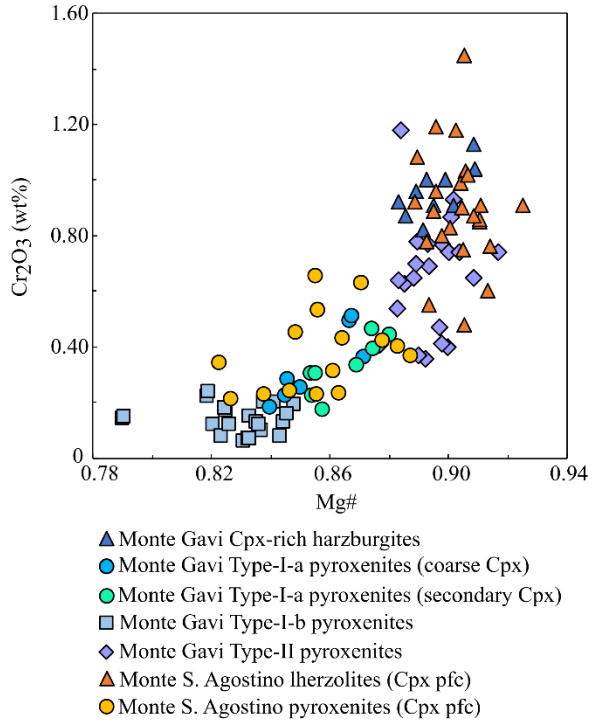

Fig. 2.9. Variation of Cr_2O_3 vs. Mg# (100 ·[Mg/(Mg + Fe_{tot})]) for clinopyroxenes from Monte Gavi and Monte Sant'Agostino peridotites and pyroxenites; pfc = porphyroclast.

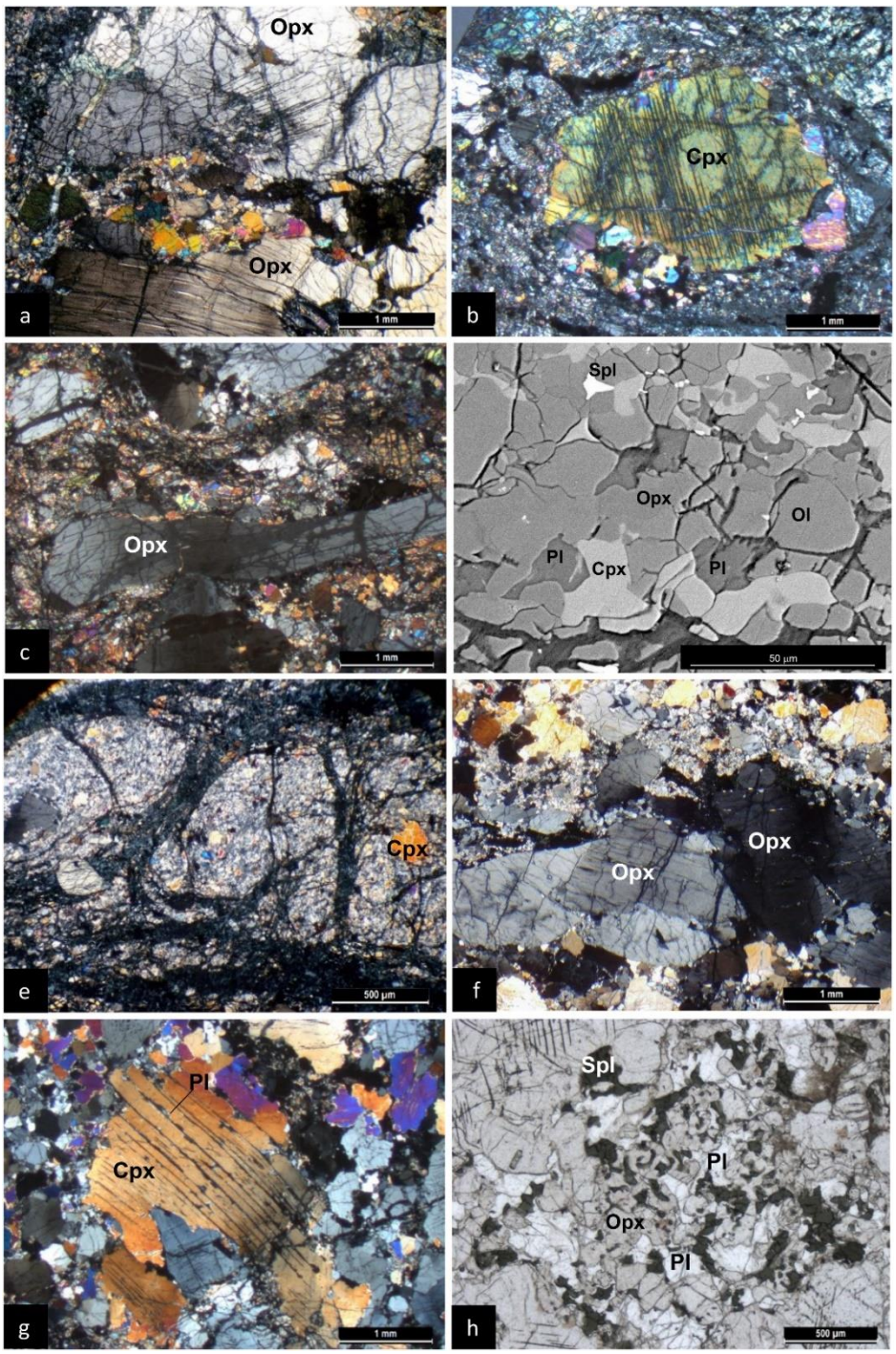

Fig. 2.10. Thin section photomicrographs under cross-polarized light (a-b-c-e-f-g), plane-polarized light (h) and BSE (back-scattered electron) image (d) of Monte Sant'Agostino samples. (a) Preserved porphyroclastic domain in peridotite with deformed orthopyroxene mantled by fine-grained neoblastic aggregates of orthopyroxene + clinopyroxene + spinel (protomylonite IC12–3); (b-c) Exsolved clino- and orthopyroxene porphyroclasts in polyphase plagioclase-bearing mylonitic matrix (lherzolite IC8–1); (d) BSE image of polyphase plagioclase-bearing mylonitic matrix (lherzolite sample IC 8–3); (e) peridotite ultramylonite with rounded pyroxene porphyroclasts cut by serpentine veins (sample IC11); (f) Orthopyroxene porphyroclasts in websterite with protomylonitic texture (sample AM489); (g) Exsolved clinopyroxene porphyroclast in websterite with protomylonitic texture (sample MP7); (h) Symplectitic orthopyroxene-spinel-plagioclase domain after garnet (sample MP7).

2.5. Geothermobarometric estimates

Temperature evaluations for the different equilibration stages recorded by the Monte Gavi and Monte Sant'Agostino peridotites and enclosed pyroxenite layers were obtained using conventional pyroxene geothermometry (Table 2.5). In particular, the two-pyroxene geothermometer (Brey and Kohler, 1990 and Taylor, 1998, referred to as T_{BK90} and T_{Ta98}, respectively) and Ca-in-orthopyroxene geothermometer (Brey and Kohler, 1990, referred to as $T_{Ca\text{-}in\text{-}Opx}$) were applied. For the Monte Gavi Type-I pyroxenites and the Monte Sant'Agostino websterites, we also calculated the equilibration temperatures (T_{HB94}) based on the amphibole-plagioclase method of Holland and Blundy (1994).

A valuable tool applicable to the plagioclase-bearing peridotites of the present study is the geobarometer of Fumagalli et al. (2017), which relies on the pressure-sensitive equilibrium Forsterite + Anorthite = Ca-Tschermak + Enstatite (FACE) and has a standard error of 0.05 GPa. Notably, the application of the FACE geobarometer to pyroxenites has been recently evaluated by Basch et al. (2020), who obtained slightly higher pressure estimates for websterites than for enclosing peridotites. In particular, a systematic pressure difference of ~0.1 GPa was related to the lower Cr# of the websterites compared with the peridotites, which led to higher Ca-Tschermak activity in the websterite clinopyroxene. Considering the uncertainties reported by Basch et al. (2020), we applied the FACE geobarometer to not only the peridotites but also the enclosed pyroxenites (Table 2.5).

2.5.1. Monte Gavi mantle section

Temperature estimates for Monte Gavi samples were calculated for:

(i) Large orthopyroxene-clinopyroxene grains from peridotite MGA7 and Type-II pyroxenite IC2/3. The cores of exsolved orthopyroxene porphyroclasts yielded $T_{Ca\text{-}in\text{-}Opx}$ of 950–1110 °C, assuming a confining pressure of 1.5 GPa. Temperature estimates obtained from two-pyroxene geothermometry for the peridotite MGA7 are shifted to lower values (897–938 °C).

(ii) Non-exsolved orthopyroxenes formed in conjunction with plagioclase in Type-I and Type-II pyroxenites. The obtained temperatures ($T_{Ca\text{-}in\text{-}Opx}$) fall in a wide range (910–1065 °C), regardless of different textural occurrences of orthopyroxene. The temperatures intervals obtained from adjacent clinopyroxene-orthopyroxene pairs (T_{Ta98} = 845–983 °C, T_{BK90} = 876–1015 °C) are slightly lower than $T_{Ca\text{-}in\text{-}Opx}$. However, the average $T_{Ca\text{-}in\text{-}Opx}$ (974 ± 47 °C) are within error of the average T_{Ta98} (913 ± 52 °C) and T_{BK90} (937 ± 47 °C).

(iii) Coexisting amphibole and plagioclase in Type-I pyroxenite GA1, which gave temperature estimates of 1030 °C using the method of Holland and Blundy (1994).

Pressure estimates by FACE geobarometer (Fumagalli et al., 2017) were only computed for the Monte Gavi pyroxenites, as the enclosing peridotites lack preserved plagioclase. We used the same clinopyroxene-orthopyroxene pairs employed for two-pyroxene geothermometric calculations and obtained pressure values ranging from 0.67 to 0.78 GPa.

2.5.2 Monte Sant'Agostino mantle section

Exsolved porphyroclast cores from mylonitic lherzolites gave relatively low clinopyroxene-orthopyroxene (T_{Ta98} = 832–886 °C, T_{BK90} = 857–950 °C) and Ca-in-Opx temperature estimates (930–970 °C). Temperature evaluations falling in the same intervals or slightly shifted towards higher values were obtained for the websterite porphyroclastic assemblage (T_{Ta98} = 914–958 °C, T_{BK90} = 940–960 °C and $T_{Ca\text{-}in\text{-}Opx}$ = 919–985 °C).

The extremely fine-grained pyroxenes from the matrix of mylonitic and ultramylonitic lherzolites yielded T_{Ta98} and T_{BK90} of 756–873 °C and $T_{Ca\text{-}in\text{-}Opx}$ of 750–780 °C. In addition, an amphibole-plagioclase pair from ultramylonitic lherzolite IC11 gave a value of 778 °C based on the Holland and Blundy (1994) method. In the websterites, we obtained: (i) T_{Ta98} = 856–880 °C, T_{BK90} = 905–938 °C and $T_{Ca\text{-}in\text{-}Opx}$ = 870–930 °C from the neoblastic pyroxenes associated with plagioclase, and (ii) 880–907 °C based on the plagioclase-amphibole method by Holland and Blundy (1994).

Application of the FACE geobarometer (Fumagalli et al., 2017) indicate shallow conditions for the development of plagioclase-bearing assemblage in the mylonitic lherzolites. Pressure values of 0.54–0.55 GPa and 0.34 GPa were obtained from lherzolites IC8–1 and IC8–3 and IC11, respectively. The websterites gave pressure stimates of 0.77–0.90 GPa.

2.6. Discussion

2.6.1. Monte Gavi: a mantle section recording reactive melt infiltration in the plagioclase stability field

The Monte Gavi harzburgite-pyroxenite association is nearly undeformed and characterized by extensive crystallization of plagioclase ± orthopyroxene at the expense of spinel and clinopyroxene. In both the harzburgites and the enclosed pyroxenites, plagioclase not only occurs as coronas around spinel but also within large clinopyroxene grains as patches or thick lamellae associated with orthopyroxene (Fig. 2.5a-b-h), locally forming symplectitic intergrowths (Fig. 2.5e). An exsolution origin of this plagioclase-orthopyroxene association is unlikely, given the high proportions of these

phases, which in places dismember the original clinopyroxene (Fig. 2.5b-d-e). Plagioclase rims around spinel in peridotites may form either during subsolidus decompression from spinel- to plagioclase-facies conditions (see Borghini et al., 2010), or in response to a reaction with an infiltrating melt in the plagioclase stability field (e.g., Rampone et al., 1997). The plagioclase-rimmed spinel of Monte Gavi harzburgites displays high TiO_2 contents (up to 0.5 wt%) and high Cr# (Fig. 2.7, Table 2.2), which contrasts with the low Cr# of coexisting orthopyroxene and clinopyroxene (Table 2.2). Similarly, spinel from Type-II pyroxenites is mantled by plagioclase and exhibits high TiO_2 and Cr# values (Fig. 2.7). These spinel chemical characteristics are typically attributed to a process of reactive melt infiltration under plagioclase-facies conditions (e.g., Kaczmarek and Müntener, 2008; Seyler and Bonatti, 1997). In Type-I pyroxenites, the reactive melt migration is documented by plagioclase ($An_{71–79}$) + orthopyroxene embayments partially replacing clinopyroxene (Fig. 2.5b-d-e).

The reaction of the pyroxenite with the infiltrating melt most likely also gave rise to the plagioclase-rich ($An_{71–79}$) and olivine-bearing ($Fo_{81–82}$) domains in Type-Ib pyroxenites. The inner sector of these domains include tiny Cr-spinel with lobate habit (Fig. 2.5f), thereby suggesting reaction of original Al-rich spinel, which is preserved in Type-Ia pyroxenites, with an infiltrating corroding melt. The accessory sulfides from these plagioclase-olivine domains may be related to crystallization from a sulphur-saturated melt exsolved during the late stages of the inferred reaction. The occurrence of both orthopyroxene and olivine-producing melt-rock reactions in Type-Ib pyroxenites was probably driven by the major role of the reacting minerals in the coarse-grained protolith. The reaction between cm-scale clinopyroxene and the infiltrating melt gave rise to a secondary mineral associations consisting of new clinopyroxene, orthopyroxene and minor plagioclase, as also observed in the enclosing harzburgites. We propose that the development of minor olivine associated with plagioclase and accessory Cr-spinel, within the cm-scale Al-spinel domains, was controlled by the Si-poor composition of the local reacting system.

Clinopyroxene from both Type-I and Type-II pyroxenites displays wide variations in Al_2O_3, TiO_2 and Na_2O (Fig. 2.8). This variability is controlled by a number of parameters, such as the chemical heterogeneity of the original spinel-facies clinopyroxene, the spinel-facies modal composition of the pyroxenites (e.g., highly variable spinel amounts) and the varying melt/pyroxenite ratio. Despite this complex scenario, we observed that clinopyroxene is Ti-enriched in response to the inferred process of reactive melt migration. For instance, secondary clinopyroxene from Type-Ia pyroxenites has higher TiO_2 than the associated coarse clinopyroxene (Fig. 2.8). Notably, a substantial TiO_2 enrichment in a mantle-infiltrating melt could be achieved through the process of percolative fractional crystallization (Bodinier et al., 2008). Hence, we speculate that the high TiO_2 contents of

most pyroxenite clinopyroxenes resulted from a plagioclase-facies reaction with a Ti-rich melt. The higher TiO_2 of coarse clinopyroxene in Type-Ib than in Type-Ia pyroxenites probably reflects a high melt/pyroxenite ratio during the reaction process forming the Type-Ib pyroxenites.

The geothermometric estimates obtained from the Monte Gavi mantle rocks do not indicate heating to near-asthenospheric conditions. The temperature evaluations based on the Ca content of exsolved orthopyroxenes for the Monte Gavi harzburgites and Type-II pyroxenites gave up to 1110 °C (Table 2.5), probably recording an old stage of spinel-facies equilibration. The results of pyroxene geothermometry applied to the secondary orthopyroxene associated with plagioclase ($T_{Ca\text{-}in\text{-}}$Opx = 910–1065 °C) and to coexisting clinopyroxenes (T_{Ta98} and T_{BK90} = 845–1015 °C) for both Type-I and -II pyroxenites likely reflects a process of subsolidus re-equilibration after the melt infiltration event. Application of the FACE geobarometer (Fumagalli et al., 2017) allowed us to constrain at 0.7–0.8 GPa the pressure conditions of plagioclase formation by melt-rock reaction in the Monte Gavi Type-Ia and Type-II pyroxenites.

In summary, the widespread formation of plagioclase in different microstructural domains of the Monte Gavi mantle harzburgites and enclosed pyroxenite layers was due to reaction with an infiltrating Ti-rich melt. Unlike the other External Ligurian peridotites, which are mostly lherzolites with 10–15 vol% clinopyroxene (Montanini et al., 2006; Rampone et al., 1995), the clinopyroxene modal abundance in the Monte Gavi harzburgites is relatively low (5–10 vol%). Notably, the envisaged melt-peridotite reaction is expected to consume clinopyroxene, thereby implying that the Monte Gavi harzburgites could be reconciled with original spinel lherzolite protoliths. The Monte Gavi harzburgites are also distinct in the absence of Ti-amphibole, in agreement with the temperature conditions recorded by $T_{Ca\text{-}in\text{-}Opx}$ geothermometer, which in some cases exceed the thermal stability of Ti-pargasite (Niida and Green, 1999).

2.6.2. Monte Sant'Agostino: a deformed mantle section

The Monte Sant'Agostino mantle section mostly consists of plagioclase-facies mylonitic lherzolites with cm-scale pyroxenite layering. Within the plagioclase mylonites, there are cm-scale porphyroclastic domains preserving an earlier, spinel-facies syn-kinematic assemblage (Fig. 2.10a). In the lherzolites, the formation of protomylonitic to ultramylonitic textures is accompanied by intracrystalline deformation of pyroxene porphyroclasts associated with development of extremely fine-grained aggregates (10–50 μm) made up of olivine + pyroxenes + plagioclase. In particular, the ultramylonites (more than 90 vol% neoblasts) are found along shear zones having a minimum thickness of ~150 m. The grain size reduction in the mylonites and ultramylonites might be supported

by grain boundary sliding related to the plagioclase-forming reactions (e.g., Kaczmarek and Tommasi, 2011).

The fertile nature of the Monte Sant'Agostino lherzolites is attested by the occurrence of Na-Al-rich clinopyroxene porphyroclasts coexisting with Cr-poor spinels (Table 2.3, Fig. 2.6). In particular, high Al_2O_3 and Na_2O contents (up to 8.4 and 2.1 wt%, respectively) are displayed by the cores of the clinopyroxene porphyroclasts, similar to other lherzolite bodies from the External Ligurian ophiolites (i.e., Monte Ragola, Rampone et al., 1995, and Rio Strega-Monte Prinzera, Montanini et al., 2006). The neoblastic clinopyroxenes from the Monte Sant'Agostino lherzolites have are distinct in their low Al_2O_3 and Na_2O (Fig. 2.6), as observed for the clinopyroxenes formed in response to the spinel- to plagioclase-facies subsolidus transition (e.g., Borghini et al., 2010).

Minimum temperatures of the spinel-facies stage preceding the plagioclase-facies recrystallization are recorded by the cores of orthopyroxene porphyroclasts, which yielded $T_{Ca\text{-}in\text{-}Opx}$ of 930–970 and 920–985 °C in the lherzolites and the websterites, respectively. The pressure-temperature calculated for the plagioclase-bearing neoblastic domains of the websteritic layers are 0.8–0.9 GPa and 870–930 °C (Table 2.5). These pressure-temperature values are significantly higher than those obtained from the enclosing mylonitic lherzolites, which gave 0.3–0.6 GPa and 750–780 °C. Notably, the pressure discrepancy is well beyond the systematic difference of ~0.1 GPa between websterites and host lherzolites found by Basch et al. (2020), who applied the FACE geobarometer to the External Ligurian Suvero mantle body and attributed this difference to an inaccurate calibration of the geobarometer for the pyroxenite chemistry. Formation of the plagioclase-bearing assemblage in the websterites at higher depth compared to the ultrafine-grained mylonitic matrix of the lherzolites (Fig. 2.11) is consistent with the notion that plagioclase starts to form at higher pressures in Al-rich and Cr-poor lithologies like pyroxenites (Borghini et al., 2010). The pressure estimates obtained from the websterites could thus reflect a recrystallization event preceding the formation of plagioclase-facies shear zones in the peridotites. Subsolidus spinel- to plagioclase transition, associated with grain-size reduction, may have caused weakening and initial strain localization in the pyroxenites, as proposed by Hidas et al. (2013) for the Ronda websterites. The pyroxenites could therefore trigger a decrease of the lithospheric mantle strength, thereby promoting subsequent involvement of the peridotites in the deformation event and development of thick mylonitic shear zones.

The Monte Sant'Agostino lherzolites do not display microstructural evidence for melt-rock reaction, even in the porphyroclastic domains that escaped the plagioclase-facies mylonitic deformation. The low Cr# (9–16) and TiO_2 (≤0.20 wt%) of spinel from the Monte Sant'Agostino lherzolites are also consistent with the notion that these rocks did not interact with melts. Likewise, the low temperature estimates obtained from the tiny pyroxenes of the mylonitic matrix cannot be

reconciled with a melt-present deformation. We thus propose that plagioclase formed under subsolidus conditions during exhumation of the Monte Sant'Agostino mantle section, in conjunction with formation of mylonitic shear zones.

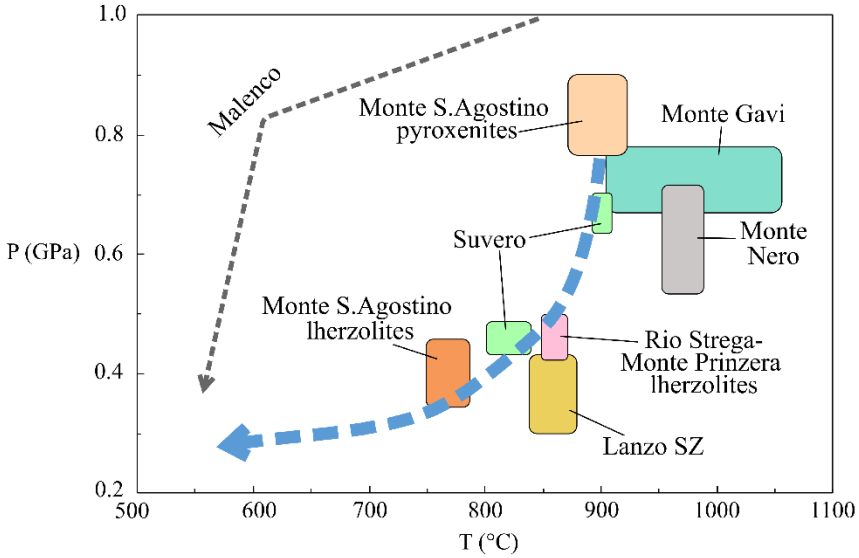

Fig. 2.11. Pressure-temperature equilibration conditions in the plagioclase stability field for the mantle sections of this study and other mantle bodies from the Western Tethys OCT, based on the P-T intervals reported in Table 5 (see text for further explanations). P-T trajectory of the EL mantle (ST and PM domains) obtained combining the P-T data of this work for the plagioclase-facies equilibration and the low-T decompression evolution reconstructed by Montanini et al. (2006). P-T trajectory for the Malenco peridotites after Müntener et al. (2000).

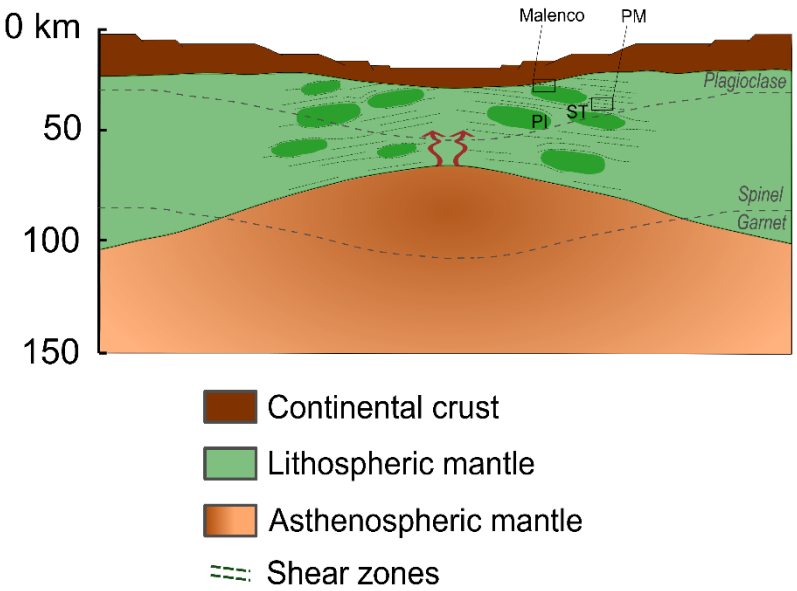

Fig. 2.12. Interpretative section of the subcontinental mantle at the onset of rifting in late Triassic displaying the different plagioclase-bearing mantle domains recognized for the External Ligurian mantle section (ST: plagioclase-spinel tectonite; PM: plagioclase mylonite, PI: plagioclase impregnated); the plagioclase-free Malenco mantle is also reported for comparison. See text for further explanations.

2.6.3. The diverse nature of pyroxenites from the External Ligurian mantle sections

The frequent occurrence of pyroxenite layers in the External Ligurian mantle bodies was recognized since the early studies of the Northern Apennine ophiolites (e.g., Beccaluva et al., 1984). Recent investigations focussed on the Suvero (Borghini et al., 2013, 2016, 2020, 2021; Hidas et al., 2020) and Rio Strega-Monte Prinzera mantle bodies (Montanini et al., 2006, 2010, 2012; Montanini and Tribuzio, 2015) highlighted the presence of different pyroxenite types, thereby providing petrological, geochemical and isotopic characterizations of the heterogeneities within the External Ligurian mantle section.

The Suvero pyroxenites include porphyroclastic spinel-bearing websterites and clinopyroxenites occurring as layers subparallel to the foliation of the enclosing spinel-facies tectonitic lherzolites (Borghini et al., 2016). The pyroxenites were partially re-equilibrated in the plagioclase stability field, with no concomitant deformation (Hidas et al., 2020). A primary garnet-bearing mineral assemblage, completely replaced by spinel-facies subsolidus recrystallization, was inferred from the rare earth element geochemical signature of bulk rock and clinopyroxene. The Suvero pyroxenites were interpreted as second-stage pyroxenites originated from reaction of the host lherzolite with tholeiitic melts derived from a hybrid eclogite-bearing peridotite source. An early Paleozoic timing of melt infiltration and pyroxenite emplacement was proposed based on a Sm-Nd whole-rock errorchron (Borghini et al., 2013).

The Rio Strega-Monte Prinzera mantle bodies include garnet clinopyroxenite and websterite layers that underwent a complex history of retrogression and deformation, which was partly related to Mesozoic lithospheric extension and thinning (Montanini et al., 2006). The garnet clinopyroxenite protoliths are characterized by a bimineralic assemblage of garnet + Al-Na-rich clinopyroxene. Garnet is typically partially replaced by symplectitic intergrowths made up of orthopyroxene, spinel, plagioclase and secondary clinopyroxene. The websterites are orthopyroxene-rich (40–50 vol%) spinel-bearing rocks. Evidence for an early garnet bearing assemblage in the websterites is provided by rounded symplectites consisting of orthopyroxene, clinopyroxene and spinel. In retrogressed garnet clinopyroxenites and websterites, the clinopyroxenes display exsolved lamellae of plagioclase. The origin of both pyroxenite types was related to recycling of old (>1.0 Ga) crustal mafic protoliths through partial melting of gabbro-derived eclogites and different extents of melt-peridotite interaction (see also Montanini et al., 2012 and Montanini and Tribuzio, 2015).

The spinel-plagioclase websterite layers from the Monte Sant'Agostino mantle section locally include pyroxene-spinel-plagioclase symplectites (Fig. 2.10h), similar to the replacement intergrowths observed in the garnet clinopyroxenites from the Rio Strega-Monte Prinzera mantle

bodies (Montanini et al., 2006). The Monte Sant'Agostino websterites also have highly aluminous clinopyroxene porphyroclasts with plagioclase + orthopyroxene exsolutions, similar to those derived from retrogression of primary Na-Al-rich clinopyroxene originally in equilibrium with garnet. In addition, both the Monte Sant'Agostino and the Rio Strega-Monte Prinzera websterites (see also Montanini and Tribuzio, 2015) are characterized by similar two-pyroxene equilibration temperatures obtained for the porphyroclastic spinel-facies assemblage (i.e., T_{BK90} of 940–960 °C and 900–980 °C, respectively), and protomylonitic textures developed in the plagioclase stability field.

The Monte Gavi pyroxenites do not display high temperature deformation microstructures and provide evidence for pervasive melt infiltration under plagioclase-facies conditions, contrary to what was observed for the other External Ligurian mantle bodies. On the other hand, the presence of pyroxenites with distinct thickness and Mg#, as suggested by the clinopyroxene chemistry (79–87 and 88–90 in Type-I and Type-II pyroxenites, respectively; Fig. 2.9), was also recognized for the Rio Strega-Monte Prinzera lherzolite-pyroxenite section (Montanini et al., 2006). The primary modal composition of Type-I (thick, Fe-rich) pyroxenites is difficult to establish, due to the extensive transformations related to the process of melt-rock reaction. We speculate that the Type-I pyroxenite protoliths were coarse-grained spinel-rich orthopyroxene-poor websterites. In addition, the low Mg# of clinopyroxene suggests crystallization in a melt-dominated system, with a negligible mass contribution from enclosing lherzolites. Type-II (thin, Mg-rich) pyroxenites were spinel-bearing olivine websterites. The presence of deformed forsterite-rich olivine and Mg-rich exsolved orthopyroxene in Type-II pyroxenites, similar to those occurring in the host peridotites, documents formation by melt/peridotite hybridization, presumably through a process leading to olivine consumption and concomitant crystallization of Mg-rich clinopyroxene + spinel.

Contrary to the pyroxenites from the Rio Strega-Monte Prinzera mantle bodies, no paragenetic or textural evidence for the presence of an earlier garnet-bearing assemblage was observed for the Monte Gavi mantle pyroxenites. Assuming that the Mg# value of the clinopyroxene cores from Type-I pyroxenites was not significantly modified by interaction with the infiltrating melts, and no Fe–Mg subsolidus exchange with associated mafic minerals occurred, we calculated the Mg# of the clinopyroxene equilibrium melts following the equation of Wood and Blundy (1997). Computed melt Mg# (49–64) are substantially lower than the Mg# of melts in equilibrium with a peridotite source. The high Al contents observed in some clinopyroxene cores of Type-I pyroxenites and the high modal proportion of Al-rich spinel (Fig. 2.8) also indicate that the pyroxenite-forming melts were characterized by low Si/Al ratios (Della-Pasqua et al., 1995). We speculate that these melts formed by partial melting of precursor mafic/pyroxenite lithology or of a mixed pyroxenite/peridotite source.

In summary, the Monte Sant'Agostino websterites are structurally and compositionally similar to the websterites, in places retaining garnet relics, from the Rio Strega-Monte Prinzera mantle bodies (Montanini et al., 2006). The Monte Gavi pyroxenites have no apparent analogues in the other mantle bodies so far described for the External Ligurian ophiolites, although new geochemical data are needed to establish their origin.

2.6.4. The heterogeneity of the External Ligurian subcontinental mantle

The mantle bodies from the External Ligurian ophiolites represent different domains of a large-scale subcontinental mantle section that was variably affected by retrogression, deformation and chemical modifications during lithospheric extension and concomitant asthenospheric ascent in response to the rifting process that led to opening of the Jurassic Western Tethys (Hidas et al., 2020; Montanini et al., 2006; Piccardo et al., 2004). Based on the main characteristics of investigated External Ligurian mantle bodies, we subdivide this subcontinental mantle section into three main domain types.

1- Plagioclase-bearing spinel tectonite domain (ST), represented by the Suvero mantle body (Fig. 2.1). The Suvero lherzolites and the enclosed pyroxenites record a deformation event developed under spinel-facies and high temperature conditions (1000–1050 °C), which yielded porphyroclastic textures associated with a penetrative tectonic foliation in lherzolites (Borghini et al., 2011; Rampone et al., 1995). The Suvero lherzolites underwent melt infiltration forming pyroxenitic heterogeneities during the early Paleozoic (Borghini et al., 2013, 2016). Melt migration and pyroxenite formation was syn- to late-kinematic with respect to the spinel-facies deformation and produced a localized metasomatic imprint in the host lherzolites (see also Borghini et al., 2021; Hidas et al., 2020). This event was inferred to have occurred under relatively high pressure conditions (>1.5 GPa) based on the geochemical evidence for a primary garnet-bearing assemblage in the pyroxenites, which was completely replaced during the subsequent decompression evolution. The Suvero mantle body provides evidence for a plagioclase-facies re-equilibration under static conditions, in response to a relatively cold decompression (Hidas et al., 2020). In particular, two recrystallization stages were recognized, from 0.6–0.7 GPa and 890–910 °C to 0.4–0.5 GPa and 800–840 °C (Fumagalli et al., 2017, see Fig. 2.11). Internal Sm-Nd isochrons (clinopyroxene-plagioclase-bulk rock) obtained from four pyroxenites gave an average age of 178 ± 8 Ma for the plagioclase-facies recrystallization (Borghini et al., 2016).

2- Plagioclase mylonite (PM) domain, including the Monte Sant'Agostino (this study) and the Rio Strega-Monte Prinzera (Fig. 2.1) mantle sections. In the lherzolites from these mantle bodies, a tectonitic texture developed under spinel-facies conditions was widely overprinted by a dynamic

plagioclase-facies recrystallization associated with development of a pervasive mylonitic foliation. Similar to the lherzolites, the enclosed pyroxenites record different extents of spinel- and plagioclase-facies deformation. Using the mineral chemistry data reported in Montanini et al. (2006), we obtained pressure and temperature estimates of 0.4–0.5 GPa and 850–870 °C ($T_{Ca\text{-}in\text{-}Opx}$) for the plagioclase-facies mylonitic deformation of the Rio Strega-Monte Prinzera lherzolites (Table 2.5). These pressure-temperature evaluations may be reconciled with the pressure-temperature evolution recognized for the Monte Sant'Agostino mantle section (Fig. 2.11), assuming that the ~0.5 GPa mantle uplift in the plagioclase stability field was associated with a polyphase deformation (Fig. 2.11). Radiometric constraints on the age of the plagioclase-facies shearing affecting the Rio Strega-Monte Prinzera mantle bodies were placed by a Lu–Hf mineral isochron of 220 ± 13 Ma obtained from a garnet pyroxenite (Montanini et al., 2006). This isochron was interpreted as a cooling age, implying that the garnet pyroxenite passed through the Lu–Hf blocking temperature of 800–900 °C (i.e., under plagioclase facies conditions) at ~220 Ma. Accordingly, we relate the polyphase plagioclase-facies deformation recorded by the PM mantle domain to large-scale lithospheric shear zones developed in the late Triassic. An early Jurassic Sm-Nd mineral isochron of 186 ± 2 Ma (defined by plagioclase, clinopyroxene, garnet and whole-rock) was also acquired from the Rio Strega-Monte Prinzera garnet pyroxenite, and interpreted to reflect a process of slow cooling in the plagioclase stability field (Montanini et al., 2006).

3- Plagioclase-impregnated domain (PI), represented by the Monte Nero mantle body (Fig. 2.1) and the Monte Gavi mantle section (this study). The former mainly consists of weakly foliated lherzolites characterized by interstitial crystallization of plagioclase and pyroxenes, and extensive replacement of Cr-spinel by plagioclase (Rampone et al., 1995). According to Piccardo et al. (2004), the formation of plagioclase in the lherzolites was related to reaction with a pervasively migrating melt. The application of the FACE geobarometer (Fumagalli et al., 2017) to (i) plagioclase-facies granoblastic aggregates, and (ii) rims of large orthopyroxenes and clinopyroxenes, and associated plagioclase (data after Rampone et al., 1995) yielded pressures of 0.6–0.7 GPa and $T_{Ca\text{-}in\text{-}Opx}$ of 960-980 °C (Table 2.5). We also applied the geothermometer of Liang et al. (2013), based on slowly diffusing trace elements like rare earth elements and Y, to clinopyroxene-orthopyroxene pairs from the Monte Nero plagioclase-facies granoblastic assemblage (Piccardo et al., 2004). The obtained temperatures (1120–1140 °C) are significantly higher than those recorded by conventional pyroxene thermometers. Such results are consistent with impregnation by asthenospheric melts, followed by slow cooling (Dygert and Liang, 2015) associated with subsolidus recrystallization. The infiltration of asthenospheric melts during the rifting-related exhumation at Monte Nero mantle body might be related to the local occurrence of cm-scale gabbroic irregular veins (Montanini et al., 2008). Notably,

this mantle body also encloses up to meter-scale gabbroic intrusions and is in places crosscut by basalt dykes, with both gabbros and basalts displaying MORB-type chemical signature (Montanini et al., 2008). The Sm–Nd clinopyroxene-plagioclase two-point alignments of 163 ± 20 Ma and 165 ± 20 Ma obtained by Rampone et al. (1995) presumably record the timing of cooling after MORB impregnation associated with plagioclase formation. The Monte Nero and Monte Gavi mantle bodies share similar pressure and $T_{Ca\text{-}in\text{-}Opx}$ estimates for the event of melt-rock reaction under plagioclase-facies conditions (Fig. 2.11), and provide no evidence for shearing in the plagioclase stability field. Contrary to the Monte Nero peridotites, however, the Monte Gavi peridotite-pyroxenite association is not intruded by gabbros nor is crosscut by basalt dikes. New geochronological constraints are therefore required to elucidate if the melt impregnation event recorded by the Monte Gavi mantle body occurred in the Jurassic or during a preceding stage (e.g., late Triassic) of the rifting evolution.

Fig. 2.11 compares the plagioclase-facies pressure-temperature evolution of the mantle sections considered in this study and of the Suvero mantle body (Borghini et al., 2011; Fumagalli et al., 2017). It also reports the pressure-temperature estimates obtained in the present study for the Rio Strega-Monte Prinzera and the Monte Nero peridotites. The ST and PM mantle domains document a relatively cold plagioclase-facies history characterized by a significant pressure decrease. We thus propose that these domains shared a common evolution in the late Triassic-early Jurassic. In this framework, the Suvero mantle body represents a nearly undeformed domain (ST), whereas plagioclase-facies strain localization produced the PM mantle domain characterized by extensive mylonitic deformation (Fig. 2.12).

The PI mantle domain records higher plagioclase-facies thermal conditions than the ST-PM mantle domains (Fig. 2.11). We relate the distinct plagioclase-facies thermal gradients recorded by the External Ligurian mantle bodies to melt-present vs. melt-absent conditions during their decompression history in the extending lithosphere. The three different mantle domains were part of a subcontinental mantle section that was involved into the development of an ocean-continent transition, towards the Adria plate, in the Middle Jurassic (Marroni et al., 1998; Montanini et al., 2006). Tectonic dismembering during convergence-related formation of sedimentary melanges in Upper Cretaceous (Marroni et al., 2017) hampered the preservation of primary relationships among the different mantle domains. We speculate that the PI domain enclosing the MOR-type crustal rocks (i.e., the Monte Nero mantle body) was located oceanward with respect to the ST-PM domains in the Middle Jurassic.

2.6.5. Constraints on the mantle evolution in the Western Tethys ocean-continent transition

Here we provide a brief overview of the lithospheric mantle bodies belonging to the ocean-continent transitional domains of the Western Tethys. In particular, we compare the rifting evolution of the External Ligurian mantle section with that inferred from the investigations carried out for the subcontinental mantle bodies from Western (Lanzo massif) and Central Alps (Malenco, Platta and Totalp). Similar to the External Ligurian mantle section, these bodies were exhumed along the OCT of the Adria margin (e.g., Guarnieri et al., 2012; Kaczmarek and Müntener, 2008; Manatschal and Müntener, 2009; Müntener et al., 2004, 2010). Their evolution from the post-Varisic orogenic collapse to the Mesozoic extensional phases and basin opening were reviewed by Picazo et al. (2016), who pointed out how their pristine compositional heterogeneity was amplified during the rifting and oceanization processes. They proposed a conceptual model with two main types of lithospheric mantle sections, namely (1) "inherited" and (2) "refertilized", exemplified by the Malenco-Totalp-Upper Platta and the Lower Platta bodies, respectively. In their view, the refertilized mantle is a subcontinental mantle section located oceanwards from the inherited subcontinental mantle.

The inherited mantle is dominated by fertile, amphibole-bearing spinel peridotites, typically interlayered with pyroxenites that are in places garnet-bearing (Müntener and Hermann, 1996). The inherited mantle is interpreted as old lithospheric mantle that was beneath the continental crust before onset of rifting. This interpretation is supported by the preservation of primary contacts between the Malenco mantle body and underplated gabbros of early Permian age (Hermann et al., 1997; Müntener and Hermann, 1996). In the inherited peridotites, no evidence for plagioclase formation, either of subsolidus or melt-rock reaction origin, was reported. Notably, the Malenco, Totalp and Upper Platta mantle bodies are characterized by similar results of REE-in-two-pyroxene and major element pyroxene thermometers (850–950 °C, Dygert and Liang, 2015), as expected for a slowly cooling, subcontinental lithospheric mantle.

In the refertilized lithospheric mantle, which also includes the Lanzo South body (Picazo et al., 2016), the peridotites mainly are plagioclase-enriched clinopyroxene-poor lherzolites (Müntener et al., 2004, 2010; Piccardo et al., 2007). These rocks enclose: (i) dunite-harzburgite bodies of replacive origin that are up to tens of meters in scale, and (ii) cm- to m-scale gabbroic veins and dykes (see also Sanfilippo et al., 2014, 2019). Pyroxene thermometry applied to spinel-facies peridotite minerals gave equilibration temperatures of 1030–1180 °C (Müntener et al., 2010), higher than those calculated for the inherited mantle. The plagioclase formation was related to infiltration of MORB-type melts associated with crystallization of new orthopyroxene after olivine and/or partial replacement of clinopyroxene by orthopyroxene and plagioclase (see also Kaczmarek and Müntener, 2008). The refertilized plagioclase-peridotites and the inherited fertile spinel-peridotites have distinct mineral compositions (Picazo et al., 2016). For instance, clinopyroxene from the refertilized peridotites has

lower Al_2O_3 and Na_2O than clinopyroxene from the inherited fertile peridotites. In addition, spinel has higher Cr# and TiO_2 in the refertilized peridotites than in the inherited fertile peridotites.

The Lanzo massif shows a peculiar transition from a domain mostly composed of old inherited lithospheric mantle in the northern part (e.g., Guarnieri et al., 2012) to a deeply melt-modified mantle section in the southern part (Piccardo et al., 2007; Sanfilippo et al., 2014, 2019). The two domains are separated by a major shear zone (up to ~1.5 km thick), in which porphyroclastic peridotites provide evidence for plagioclase-facies melt-rock reactions, in turn overprinted by plagioclase mylonites recording solid state deformation (e.g., Kaczmarek and Müntener, 2008; Kaczmarek and Tommasi, 2011). The mylonites were interpreted as the footwall of an extensional detachment fault that accomodated exhumation of the Lanzo mantle and acted as a permeability barrier between the inherited (northern Lanzo) and refertilized (Southern Lanzo) domains. We applied the FACE geobarometer to the neoblastic plagioclase-bearing assemblage of the Lanzo mylonitic peridotites (Kaczmarek and Müntener, 2008), thereby yielding remarkably low pressure values of 0.3 GPa (Table 2.5, Fig. 2.11). These pressure estimates are coupled with $T_{Ca\text{-}in\text{-}Opx}$ (Brey and Kohler, 1990) of 840–870 °C, indicating a high geothermal gradient, presumably related to extreme lithospheric thinning and asthenosphere ascent. We obtained slightly higher pressure-temperature values from the porphyroclastic peridotites of 0.4 GPa and 890 °C sampled along the margins of the shear zone.

Picazo et al. (2016) placed the External Ligurian mantle bodies in the refertilized lithospheric mantle, because of the widespread occurrence of plagioclase-bearing peridotites. However, only some mantle bodies from the External Ligurian units include plagioclase originated by reaction with infiltrating melts (i.e., the PI domain defined in the preceding section). The refertilized mantle of Picazo et al. (2016) and the External Ligurian PI domain actually share several structural and compositional similarities, namely: (i) the presence of microstructures indicating melt-rock reactions in the plagioclase stability field, (ii) the clinopyroxene and spinel composition (Figs. 2.6 and 2.7), and (iii) the relatively high temperatures computed for the plagioclase re-equilibration (Fig. 2.11). Conversely, the External Ligurian plagioclase-bearing spinel tectonites and plagioclase mylonites (ST and PM domains, respectively) record formation of plagioclase in response to subsolidus decompression, with no melt involvement. However, the reconstruction of the Jurassic OCT by Picazo et al. (2016) does not include the occurrence of a plagioclase-bearing mantle section with no melt-rock reaction evidence.

The fertile spinel peridotites considered as inherited subcontinental mantle by Picazo et al. (2016) bear several similarities with the spinel tectonite and mylonite protoliths of the External Ligurian mantle bodies. Taken as a whole, these peridotites are characterized by a fertile geochemical signature, presence of Al- and Na-rich clinopyroxene (Fig. 2.6) and disseminated Ti-amphibole.

Pyroxenite layers, in places garnet-bearing, are also widespread in both mantle section types. Following the subdivision of the Tethyan OCT mantle into two main types (Picazo et al., 2016), we therefore place the ST and PM mantle domains of the External Ligurian units into the inherited subcontinental mantle.

The Malenco-Totalp-Upper Platta mantle bodies and the External Ligurian ST and PM mantle domains underwent distinct pressure-temperature evolutions during the post-Variscan lithospheric extension and the subsequent Mesozoic rifting (Fig. 2.11). A cold exhumation path was depicted for the Malenco mantle body, considered as the type locality of inherited mantle (Müntener et al., 2000). The Malenco peridotites underwent a near-isobaric cooling to ~600 °C in the late Paleozoic, followed by near-isothermal decompression from ~0.8 to ~0.4 GPa, associated with formation of chlorite and Mg-hornblende, locally along mylonitic shear zones (see also Müntener and Hermann, 2001). Based on $^{40}Ar/^{39}Ar$ amphibole investigations (Villa et al., 2000), the decompression was inferred to have started in the late Triassic (~225 Ma) and was related to the onset of the rifting evolution leading to opening of the Western Tethys.

The External Ligurian PM domain provides evidence for a two-stage high temperature decompression starting from the base of continental lithosphere (Montanini et al., 2006). The early decompression from ~2.8 GPa and ~1100 °C to the spinel lherzolite stability field was associated with cooling to ~950 °C and was followed by a polyphase shearing under plagioclase-facies conditions ending at 0.3–0.6 GPa and 750–780 °C (Fig. 2.11). Whereas the age of the high temperature decompression to spinel-facies lherzolite conditions is unconstrained, the Lu–Hf cooling age of 220 ± 13 Ma (Montanini et al., 2006) indicate that the spinel to plagioclase-facies transition was related to the Mesozoic rifting event (see also §2.6.3). The similar $^{40}Ar/^{39}Ar$ and Lu–Hf cooling ages obtained respectively for the Malenco mantle body and the External Ligurian PM domain suggest different thermal conditions in the late Triassic, namely the Malenco was ~250–300 °C colder than the External Ligurian PM domain. The distinct exhumation histories might reflect different mantle depths at the time of the rifting inception. In this view, the External Ligurian PM domain was exhumed from deeper (and hotter) conditions than the spinel peridotites from the Malenco mantle body (Fig. 2.12).

The plagioclase-facies shear zones within the External Ligurian PM domain document a major deformation event that accommodated exhumation of the spinel-facies subcontinental mantle in the plagioclase stability field. These shear zones cannot be considered as counterparts of those occurring in the central Lanzo massif. The porphyroclastic spinel protoliths of the External Ligurian mylonites do not provide evidence for melt infiltration and refertilization before or during shearing. The Lanzo plagioclase-facies shear zones are also distinct for being crosscut by MOR-type gabbros and basalts.

Notably, available geochronological data for the replacive harzburgites and the gabbros of the Lanzo Massif cluster in the Middle Jurassic (Kaczmarek et al., 2008; Sanfilippo et al., 2019). Hence, the Lanzo shear zones were most likely related to an advanced stage of the rifting evolution, which ultimately formed an oceanward OCT sector.

In summary, the onset of the Tethyan rifting involved uplift of subcontinental mantle in the late Triassic, as documented by the Malenco body (e.g., Müntener and Hermann, 2001) and the External Ligurian PM domain (Montanini et al., 2006). This scenario is consistent with the information acquired from the lower continental crust section of the Ivrea-Verbano Zone, which formed a distal sector of the extending Adria continental margin in the Middle Jurassic (e.g., Beltrando et al., 2015). The Ivrea-Verbano Zone actually documents that the rifting evolution started in the late Triassic (see also Ferrari et al., 2021) and was associated with localized infiltration of mantle-derived melts with overall alkaline signature (Bonazzi et al., 2020; Schaltegger et al., 2015; Stahle et al., 1990). Notably, the alkaline magmatism in the Ivrea-Verbano Zone continued until the early Jurassic (see also Galli et al., 2019 and Grieco et al., 2001). From the late Triassic, the rifting evolution probably comprised asthenosphere ascent, melt production and refertilization of the subcontinental mantle, with a Middle Jurassic climax developing MORB-type melts and opening of the Western Tethys.

2.7. Conclusions

The subcontinental mantle section from the External Ligurian units (Northern Appennine) consists of three distinct mantle domains, developed in response to the rifting evolution that ultimately formed a Middle Jurassic ocean-continent transition: (1) a spinel tectonite domain that underwent no significant deformation and melt-rock reaction under plagioclase-facies conditions, characterized by static plagioclase development under decreasing pressure conditions, (2) a plagioclase mylonite domain experiencing melt-absent deformation under decreasing pressure conditions, and (3) a nearly undeformed domain that underwent melt infiltration and reaction under plagioclase-facies conditions. We relate mantle domains (1, 2) to a rifting-driven uplift in the late Triassic accommodated by large-scale shear zones consisting of plagioclase mylonites.

We distinguish different mantle exhumation styles for the onset of the Tethyan rifting. A cold mantle exhumation is exemplified by the Malenco mantle body (Central Alps), in which low temperature hydrous mylonites developed at the expense of porphyroclastic spinel lherzolites. The External Ligurian mantle domains (1, 2) highlight mantle exhumation accommodated by large-scale shear zones consisting of anhydrous, melt-absent plagioclase-facies mylonites. The role of these shear zones in mantle exhumation along modern and fossil OCTs has been overlooked and needs further reconsideration in future studies. From the late Triassic, the Tethyan rifting evolution probably

involved asthenosphere ascent, melt production and refertilization of the subcontinental lithospheric mantle. The crustal breakup was associated with a major event of formation of MORB-type melts in the Middle Jurassic, with the mantle exhumation partly driven by a melt-present plagioclase-facies deformation, as documented by the Lanzo mantle body from Western Alps.

2.8. References

Basch V., Borghini G., Fumagalli P., Rampone E., Gandolfo A., Ferrando C., 2020. Plagioclase-facies thermobarometric evolution of the External Liguride pyroxenite-bearing mantle (Suvero, Italy). Ofioliti 45, 1-12

Basch V., Rampone E., Borghini G., Ferrando C., Zanetti A., 2019. Origin of pyroxenites in the oceanic mantle and their implications on the reactive percolation of depleted melts. Contributions to Mineralogy and Petrology 174, 97

Beccaluva L., Macciotta G., Piccardo G.B. and Zeda O., 1984. Petrology of lherzolitic rocks from the Northern Apennine ophiolites. Lithos 17, 299-316

Beltrando M., Stockli D.F., Decarlis A. and Manatschal G., 2015. A crustal-scale view at rift localization along the fossil Adriatic margin of the Alpine Tethys preserved in NW Italy. Tectonics 34, 1927-1951

Bodinier J.-L., Garrido C.J., Chanefo I., Bruguier O. and Gervilla F., 2008. Origin of pyroxenite-peridotite veined mantle by refertilization reactions: Evidence from the Ronda peridotite (Southern Spain). Journal of Petrology 49, 999-1025

Bonazzi M., Langone A., Tumiati S., Dellarole E., Mazzucchelli M., Giovanardi T. and Zanetti A., 2020. Mantle-Derived Corundum-Bearing Felsic Dykes May Survive Only within the Lower (Refractory/Inert) Crust: Evidence from Zircon Geochemistry and Geochronology (Ivrea-Verbano Zone, Southern Alps, Italy). Geosciences 10, 281

Borghini G., Fumagalli P. and Rampone E., 2010. The Stability of Plagioclase in the Upper Mantle: Subsolidus Experiments on Fertile and Depleted Lherzolite. Journal of Petrology 51, 229-254

Borghini G., Fumagalli P. and Rampone E., 2011. The geobarometric significance of plagioclase in mantle peridotites: A link between nature and experiments. Lithos 126, 42-53

Borghini G., Rampone E., Class C., Goldstein S., Cai Y., Cipriani A., Hofmann A.W., Bolge L., 2021. Enriched Hf–Nd isotopic signature of veined pyroxenite-infiltrated peridotite as a possible source for E-MORB. Chemical Geology 586, 120591

Borghini G., Rampone E., Zanetti A., Class C., Cipriani A., Hofmann A.W. and Goldstein S.L., 2013. Meter-scale Nd isotopic heterogeneity in pyroxenite-bearing Ligurian peridotites encompasses global-scale upper mantle variability. Geology 41, 1055-1058

Borghini G., Rampone E., Zanetti A., Class C., Cipriani A., Hofmann A.W. and Goldstein S.L., 2016. Pyroxenite Layers in the Northern Apennines' Upper Mantle (Italy)-Generation by Pyroxenite Melting and Melt Infiltration. Journal of Petrology 57,625-653

Borghini G., Rampone E., Zanetti A., Class C., Fumagalli P., Godard M., 2020. Ligurian pyroxenite-peridotite sequences (Italy) and the role of melt-rock reaction in creating enriched-MORB mantle sources. Chemical Geology 532, 119252

Brey G.P. and Köhler T., 1990. Geothermobarometry in four phase lherzolites II. New thermobarometers, and practical assessment of existing thermobarometers. Journal of Petrology 31, 1353-1378

Chazot G., Charpentier S., Kornprobst J., Vannucci R. and Luais B., 2005. Lithospheric Mantle Evolution During Continental Break-Up: The West Iberia Non-Volcanic Passive Margin. Journal of Petrology 46, 2527-2568

Conti P., Cornamusini G. and Carmignani L., 2020. An outline of the geology of the Northern Apennines (Italy), with Geological Map at 1:250,000 scale. Italian Journal of Geosciences 139, 149-194

Della-Pasqua F.N., Kamenetsky V.S., Gasparon M., Crawford A.J. and Varne R., 1995. Al-spinels in primitive arc volcanics. Mineralogy and Petrology 53, 1-26

Dygert N. and Liang Y., 2015. Temperatures and cooling rates recorded in REE in coexisting pyroxenes in ophiolitic and abyssal peridotites. Earth and Planetary Science Letters 420, 151-161

Elter P., Ghiselli F., Marroni M. and Ottria G., 1997. Note illustrative del Foglio 198 "Bobbio" della Carta Geologica d'Italia in scala 1:50.000

Ferrari E., Tribuzio R., Bosch D. and Bruguier O., 2021. Constraints on the post-Variscan thermal evolution of the Ivrea crustal section (Italian-Swiss Alps) from U-Pb dating of relict rutile in middle crust amphibolites. Lithos 406-407, 106500

Fumagalli P., Borghini G., Rampone E. and Poli S., 2017. Experimental calibration of Forsterite–Anorthite–CaTscherm.ak–Enstatite (FACE) geobarometer for mantle peridotites. Contributions to Mineralogy and Petrology 172, 38

Galli A., Grassi D., Sartori G., Gianola O., Burg J.P. and Schmidt M.W., 2019. Jurassic carbonatite and alkaline magmatism in the Ivrea zone (European Alps) related to the breakup of Pangea. Geology 47, 199-202

Grieco G., Ferrario A., Von Quadt A., Köppel V. and Mathez E.A., 2001. The Zircon-bearing Chromitites of the Phlogopite Peridotite of Finero (Ivrea Zone, Southern Alps): Evidence and Geochronology of a Metasomatized Mantle Slab. Journal of Petrology 42, 89-101

Guarnieri L., Nakamura E., Piccardo G.B., Sakaguchi C., Shimizu N., Vannucci R. and Zanetti A., 2012. Petrology, Trace Element and Sr, Nd, Hf Isotope Geochemistry of the North Lanzo Peridotite Massif (Western Alps, Italy). Journal of Petrology 53, 2259-2306

Hermann J., Müntener O., Trommsdorff V., Hansmann W., Piccardo G.B., 1997. Fossil crust-to-mantle transition, Val Malenco (Italian Alps). Journal of Geophysical Research-Solid Earth 102, 20123-20132

Hidas K., Borghini G., Tommasi A., Zanetti A. and Rampone E., 2020. Interplay between melt infiltration and deformation in the deep lithospheric mantle (External Liguride ophiolite, North Italy). Lithos 380-381, 105855

Hidas K., Garrido C., Tommasi A., Padrón-Navarta J.A., Thielmann M., Konc Z., Frets E. and Marchesi C., 2013. Strain Localization in Pyroxenite by Reaction-Enhanced Softening in the Shallow Subcontinental Lithospheric Mantle. Journal of Petrology 54, 1997-2031

Holland T. and Blundy J., 1994. Non-ideal interactions in calcic amphiboles and their bearing on amphibole-plagioclase thermometry. Contributions to Mineralogy and Petrology 116, 433-447

Kaczmarek M.-A. and Müntener O., 2008. Juxtaposition of Melt Impregnation and High-Temperature Shear Zones in the Upper Mantle; Field and Petrological Constraints from the Lanzo Peridotite (Northern Italy). Journal of Petrology 49, 2187-2220

Kaczmarek M.-A. and Müntener O., 2010. The variability of peridotite composition across a mantle shear zone (Lanzo massif, Italy): interplay of melt focusing and deformation. Contributions to Mineralogy and Petrology 160, 663-679

Kaczmarek M.-A., Müntener O. and Rubatto D., 2008. Trace element chemistry and U–Pb dating of zircons from oceanic gabbros and their relationship with whole rock composition (Lanzo, Italian Alps). Contributions to Mineralogy and Petrology 155, 295-312

Kaczmarek M.-A. and Tommasi A., 2011. Anatomy of an extensional shear zone in the mantle, Lanzo massif, Italy. Geochemistry, Geophysics, Geosystem, 12(8)

Leake B.E., Woolley A.R., Arps C.E., Birch W.D., Gilbert M.C., Grice J.D., Hawthorne F.C., Kato A., Kisch H.J., Krivovichev V.G., Linthout K., Laird J., Mandarino J., Maresch W.V., Nickel E.H., Tock N.M.S., Schumacher J.C., Smith D.C., Stephenson N.C.N., Ungaretti L., Whittaker E.J.W. and Youzhi G., 1997. Nomenclature of amphiboles; report of the Subcommittee on Amphiboles of the International Mineralogical Association Commission on new minerals and mineral names. Mineralogical Magazine 61, 295-310

Liang Y., Sun C. and Yao L., 2013. A REE-in-two-pyroxene thermometer for mafic and ultramafic rocks. Geochimica Cosmochimica Acta 102, 246-260

Manatschal G. and Müntener O., 2009. A type sequence across an ancient magma-poor ocean–continent transition: the example of the western Alpine Tethys ophiolites. Tectonophysics 473, 4-19

Marroni M., Meneghini F. and Pandolfi L., 2017. A revised subduction inception model to explain the Late Cretaceous, double-vergent orogen in the precollisional western Tethys: Evidence from the Northern Apennines. Tectonics 36, 2227-2249

Marroni M., Molli G., Montanini A. and Tribuzio R., 1998. The association of continental crust rocks with ophiolites in the Northern Apennines (Italy): implications for the continent-ocean transition in the Western Tethys. Tectonophysics 292, 43-66

McCarthy A., Falloon T.J., Sauermilch I., Whittaker J.M., Niida K. and Green D.H., 2020. Revisiting the Australian-Antarctic ocean-continent transition zone using petrological and geophysical characterization of exhumed subcontinental mantle. Geochemistry Geophysics Geosystem 21, 1-25

Montanini A. and Tribuzio R., 2001. Gabbro-derived granulites from the Northern Apennines (Italy): Evidence for lower-crustal emplacement of tholeiitic liquids in post-Variscan times. Journal of Petrology 42, 2259-2277

Montanini A. and Tribuzio R., 2015. Evolution of recycled crust within the mantle: Constraints from the garnet pyroxenites of the External Ligurian ophiolites (northern Apennines, Italy). Geology 43, 911-914

Montanini A., Tribuzio R. and Anczkiewicz R., 2006. Exhumation History of a Garnet Pyroxenite-bearing Mantle Section from a Continent-Ocean Transition (Northern Apennine Ophiolites, Italy). Journal of Petrology 47, 1943-1971

Montanini A., Tribuzio R. and Bersani D., 2010. Insights into the origin of mantle graphite and sulphides in garnet pyroxenites from the External Liguride peridotites (Northern Apennine, Italy). Geological Society Special Publications 337, 87-105

Montanini A., Tribuzio R. and Thirlwall M., 2012. Garnet clinopyroxenite layers from the mantle sequences of the Northern Apennine ophiolites (Italy): Evidence for recycling of crustal material. Earth and Planetary Science Letters 351-352, 171-181

Montanini A., Tribuzio R. and Vernia L., 2008. Petrogenesis of basalts and gabbros transition (external Liguride from an ancient continent-ocean ophiolites, northern Italy). Lithos 101, 453-479

Müntener O. and Manatschal G., 2006. High degrees of melt extraction recorded by spinel harzburgite of the Newfoundland margin: The role of inheritance and consequences for the evolution of the southern North Atlantic. Earth and Planetary Science Letters 252, 437-452

Müntener O., Manatschal G., Desmurs L. and Pettke T., 2010. Plagioclase Peridotites in Ocean-Continent Transitions: Refertilized Mantle Domains Generated by Melt Stagnation in the Shallow Mantle Lithosphere. Journal of Petrology 51, 255-294

Müntener O. and Hermann J., 1996. The Val Malenco lower crust- upper mantle complex and its field relations (Italian Alps). Schweiz Miner Petrog 76, 475-500

Müntener O. and Hermann J., 2001. The role of lower crust and continental upper mantle during formation of non-volcanic passive margins: evidence from the Alps. Geological Society Special Publications 187, 267-288

Müntener O., Hermann J. and Trommsdorff V., 2000. Cooling History and Exhumation of Lower-Crustal Granulite and Upper Mantle (Malenco, Eastern Central Alps). Journal of Petrology 41, 175-200

Müntener O., Pettke T., Desmurs L., Meier M. and Schaltegger U., 2004. Refertilization of mantle peridotite in embryonic ocean basins: trace element and Nd isotopic evidence and implications for crust-mantle relationships. Earth and Planetary Science Letters 221, 293-308

Niida K. and Green D.H., 1999. Stability and chemical composition of pargasitic amphibole in MORB pyrolite under upper mantle conditions. Contributions to Mineralogy and Petrology 135, 18-40

Passchier C.W. and Trouw R.A.J., 2005. Microtectonics. Springer, pp. 106

Picazo S., Müntener O., Manatschal G., Bauville A., Karner G. and Johnson C, 2016. Mapping the nature of mantle domains in Western and Central Europe based on clinopyroxene and spinel chemistry: Evidence for mantle modification during an extensional cycle. Lithos 266–267, 233-263

Piccardo G.B., Müntener O., Zanetti A. and Pettke T., 2004. Ophiolitic Peridotites of the Alpine-Apennine System: Mantle Processes and Geodynamic Relevance. International Geology Review 46 (12), 1119-1159

Piccardo G.B., Zanetti A. and Müntener O., 2007. Melt/peridotite interaction in the Southern Lanzo peridotite: Field, textural and geochemical evidence. Lithos 94, 181-209

Rampone E., Borghini G. and Basch V., 2020. Melt migration and melt-rock reaction in the Alpine-Apennine peridotites: Insights on mantle dynamics in extending lithosphere. Geoscience Frontiers 11, 151-166

Rampone E., Hofmann A.W., Piccardo G.B., Vannucci R., Bottazzi P. and Ottolini L., 1995. Petrology, Mineral and Isotope Geochemistry of the External Liguride Peridotites (Northern Apennines, Italy). Journal of Petrology 36, 81-105

Rampone E., Piccardo G.B., Vannucci R. and Bottazzi P, 1997. Chemistry and origin of trapped melts in ophiolitic peridotites. Geochimica Cosmochimica Acta 61, 4557-4569

Renna M.R. and Tribuzio R., 2009. Petrology, geochemistry and U–Pb zircon geochronology of lower crust pyroxenites from northern Apennine (Italy): insights into the post-collisional Variscan evolution. Contributions to Mineralogy and Petrology 157, 813-835

Sanfilippo A., Salters V., Tribuzio R. and Zanetti A., 2019. Role of ancient, ultra-depleted mantle in Mid-Ocean-Ridge magmatism. Earth and Planetary Science Letters 511, 89-98

Sanfilippo A. and Tribuzio R., 2011. Melt transport and deformation history in a nonvolcanic ophiolitic section, northern Apennines, Italy: Implications for crustal accretion at slow spreading settings. Geochemistry Geophysics Geosystem, 12(7)

Sanfilippo A., Tribuzio R. and Tiepolo M., 2014. Mantle-crust interactions in the oceanic lithosphere: Constraints from minor and trace elements in olivine. Geochimica Cosmochimica Acta 141, 423-439

Schaltegger U., Ulianov A., Müntener O., Ovtcharova M., Peytcheva I., Vonlanthen P., Vennemann T., Antognini M. and Girlanda F., 2015. Megacrystic zircon with planar fractures in miaskite-type nepheline pegmatites formed at high pressures in the lower crust (Ivrea Zone, southern Alps, Switzerland). American Mineralogist 100, 83-94

Schettino A. and Turco E., 2011. Tectonic history of the western Tethys since the Late Triassic. Geological Society American Bullettin 123, 89-105

Seyler M. and Bonatti E., 1997. Regional-scale melt-rock interaction in lherzolitic mantle in the Romanche Fracture Zone (Atlantic Ocean). Earth and Planetary Science Letters 146, 273-287

Snow J.E., Schmidt G. and Rampone E., 2000. Os isotopes and highly siderophile elements (HSE) in the Ligurian ophiolites, Italy. Earth and Planetary Science Letters 175, 119-132

Stähle V., Frenzel G., Kober B., Michard A., Puchelt H. and Schneider W. 1990. Zircon syenite pegmatites in the Finero peridotite (Ivrea zone): Evidence for a syenite from a mantle source. Earth and Planetary Science Letters 101, 196-205

Sutra E. and Manatschal G., 2012. How does the continental crust thin in a hyperextended rifted margin? Insights from the Iberia margin. Geology 40, 139-142

Taylor W.R., 1998. An experimental test of some geothermometer and geobarometer formulations for upper mantle peridotites with application to the thermobarometry of fertile lherzolite and garnet websterite. Neues Jb Miner Abh 172, 381-408

Tribuzio R., Garzetti F., Corfu F., Tiepolo M. and Renna M.R., 2016. U-Pb zircon geochronology of the Ligurian ophiolites (Northern Apennine, Italy): Implicatins for continental breakup to slow seafloor spreading. Tectonophysics 666, 220-243

Tribuzio R., Renna M.R., Dallai L. and Zanetti A., 2014. The magmatic-hydrothermal transition in the lower oceanic crust: Clues from the Ligurian ophiolites, Italy. Geochimica Cosmochimica Acta 130, 188-211

Tribuzio R., Thirlwall M. and Vannucci R., 2004. Origin of the Gabbro---Peridotite Association from the Northern Apennine Ophiolites (Italy). Journal of Petrology 45, 1109-1124

Villa I.M., Hermann J., Müntener O. and Trommsdorff V., 2000. 39Ar−40Ar dating of multiply zoned amphibole generations (Malenco, Italian Alps). Contributions to Mineralogy and Petrology 140, 363-381

Whitmarsh R. B., Manatschal G. and Minshull T. A., 2001. Evolution of magma-poor continental margins from rifting to seafloor spreading. Nature 413, 150-154

Whitney D.L. and Evans B.W., 2010. Abbreviations for names of rock-forming minerals. American Mineralogist 95, 185–187

Wood B.J. and Blundy J.D., 1997. A predictive model for rare earth element partitioning between clinopyroxene and anhydrous silicate melt. Contributions to Mineralogy and Petrology 129, 166-181

2.9. Tables

Table 2.1. Summary of microstructural and mineralogical features of Monte Gavi and Monte Sant'Agostino mantle rocks

	Samples	*Lithology*	*Thickness*	*Microstructure*	*Main petrographic features*
Monte Gavi mantle sequence					
Peridotites	MGA7	Cpx-rich Spl-Pl harzburgite	-	Nearly isotropic; coarse-grained, impregnated	Evidence of melt-rock reaction: Cr-Ti-rich Spl (Cr#= 33-35, TiO_2 =0.3-0.5 wt.%) with Pl coronas; Pl + Opx as replacement of Cpx
Type Ia pyroxenites	GAV2	Spl websterite*	~10-80 cm	Isotropic, coarse-grained, granular allotriomorphic	Coarse Al-Spl (Cr# = 2-4, TiO_2 < 0.10 wt %) with thin Pl rims and smaller Cr-Spl (Cr# = 12-34, TiO_2 = 0.15-1.0 wt%); embayed coarse Cpx with Pl + Opx lamellae; Mg# of coarse Cpx = 84-86
Type Ib pyroxenites	GA1, MG6	Spl websterite*	~10-80 cm	Isotropic, coarse-grained, granular allotriomorphic	Pyroxene-rich (Cpx + Opx + Pl) and Pl-rich (Pl + Ol + Cr-Spl + Ilm + sulfide) domains relict coarse Cpx replaced by Opx + Pl as rims and lamellae; Mg# of Cpx = 79-85
Type II pyroxenites	MG5, IC2/3, MG9	Ol-Spl websterite*	~10 cm	Isotropic, medium-to coarse-grained, granular allotriomorphic	Relict exsolved Opx and Fo-rich Ol (89 mol%) from the host peridotite + Cpx-rich domains with interstitial Pl (embayed Cpx with lamellae of Pl + Opx); spinels with variable Cr# (6-16) and TiO_2 (0.1-0.6 wt%) rimmed by Pl
Monte Sant'Agostino mantle sequence					
Peridotites	MGO1, IC8-1, IC8-3, IC11	Spl- Pl lherzolite	-	Foliated, protomylonitic to ultramylonitic with spinel tectonite relics	Opx+Cpx (+Spl+Ti-Amp) porphyroclasts in a ultrafine-grained Ol+Opx+Cpx+Pl ± Amp ± Spl polyphase matrix; highly stretched Opx. Al_2O_3 (7.0-8.4 wt%) and Na_2O-rich (1.6-2.1 wt%) Cpx porphyroclasts, Cr-and Ti-poor Spl (Cr# = 8-16, TiO_2 < 0.2 wt%)
Pyroxenites	AM489, MP7, IC10-1	Spl websterites	~1-10 cm	Protomylonitic	Porphyroclasts of Cpx + Opx + Al-Spl set into a matrix of Cpx + Opx + Ol + Pl + Ti-Amp; Opx + Al-Spl + Pl symplectitic intergrowths after garnet

* protolith before melt-rock interaction; sample locations are reported in Fig. 2.2

Table 2.2. Representative major element compositions (wt%) of minerals from Monte Gavi selected samples.

	SiO_2	TiO_2	Al_2O_3	Cr_2O_3	FeO	MnO	MgO	CaO	Na_2O	K_2O	NiO	Total	Mg#	Cr#	An
MGA7 Harzburgite															
Ol	40.61	-	-	-	9.57	0.08	49.42	0.09	-	-	0.50	100.27	90	-	-
Opx core	54.49	0.09	5.40	0.67	7.20	0.11	32.38	0.79	-	-	-	101.12	89	-	-
Opx rim	55.48	0.15	3.59	0.79	7.11	0.17	32.79	0.87	-	-	-	100.95	89	-	-
Cpx core	49.90	0.58	7.29	0.92	3.49	0.06	14.77	21.65	0.88	-	-	99.53	88	-	-
Cpx rim	51.66	0.83	4.69	1.13	2.88	-	15.98	22.19	0.75	-	-	100.11	91	-	-
Spl	-	0.50	36.92	28.47	19.30	0.22	14.53	-	-	-	-	99.95	57	34	-
GAV2 Type-Ia pyroxenite															
Coarse Cpx core	48.60	0.77	8.66	0.18	4.73	0.01	13.88	21.92	0.70	-	-	99.45	84	-	-
Coarse Cpx rim	51.25	0.67	5.22	0.24	4.50	0.18	15.18	22.74	0.49	-	-	100.47	86	-	-
Small Cpx core	49.77	0.79	7.41	0.24	4.65	0.30	15.43	21.62	0.66	-	-	100.86	86	-	-
Small Cpx rim	51.11	0.80	4.97	0.30	4.54	0.04	15.76	22.74	0.44	-	-	100.69	86	-	-
Al-Spl	-	-	63.43	2.12	15.73	0.14	18.67	-	-	-	-	100.10	71	2	-
Cr-Spl	-	1.02	32.98	25.40	27.43	-	12.28	-	-	-	-	99.11	53	34	-
GA1 Type-Ib pyroxenite															
Pyroxene-rich domain															
Coarse Cpx1 core	46.48	2.33	9.71	0.14	6.85	0.12	14.43	17.64	1.73	-	-	99.43	79	-	-
Coarse Cpx2 core	48.44	2.01	7.88	0.20	5.40	0.20	15.58	17.75	1.40	-	-	98.86	84	-	-
Coarse Cpx2 rim	50.46	1.66	6.21	0.13	5.15	0.08	14.61	22.50	0.46	-	-	101.27	83	-	-
Small Cpx	49.24	1.58	6.65	0.11	5.32	0.24	14.23	21.69	0.66	-	-	99.73	83	-	-
Opx (rim of Cpx)	54.62	0.38	2.52	0.07	12.28	0.40	29.01	0.65	-	-	-	99.92	81	-	-
Opx (coarse lamella in Cpx)	54.13	0.50	2.85	0.05	11.65	0.30	29.13	0.95	-	-	-	99.56	82	-	-
Amp	42.57	3.67	12.88	0.38	7.74	0.11	15.21	11.65	3.26	-	-	97.48	78	-	-
Plagioclase-rich domain															
Pl	47.89	-	34.01	-	0.33	-	-	15.42	2.30	-	-	99.94	-	-	79
Ol	39.87	-	-	-	17.39	0.30	42.52	-	-	-	0.24	100.32	81	-	-
Spl	-	0.61	35.81	23.16	28.25	0.37	11.00	-	-	-	-	99.20	48	30	-

MG6 Type-Ib pyroxenite															
Pyroxene-rich domain															
Coarse Cpx core	48.79	1.69	7.49	0.12	5.39	0.18	15.45	20.69	0.77	-	-	100.57	84	-	-
Coarse Cpx rim	50.23	1.51	5.54	0.11	4.70	0.16	15.54	22.11	0.40	-	-	100.30	85	-	-
Small Cpx	49.67	1.58	6.16	0.19	4.81	-	15.49	21.65	0.52	-	-	100.07	85	-	-
Opx (symplectite with Pl)	54.13	0.40	2.91	0.11	10.99	0.31	30.07	0.96	-	-	-	99.88	83	-	-
Plagioclase-rich domain															
Pl	47.42	-	33.70	-	-	-	14.43	2.95	-	-	-	98.50	-	-	73
Ol	39.47	-	-	-	17.59	0.10	43.70	-	-	-	0.19	101.05	82	-	-
Spl	-	0.79	45.02	14.48	26.33	0.15	12.19	-	-	-	-	98.96	51	18	-
IC2/3 Type-II pyroxenite															
Ol	40.57	-	-	-	10.63	0.10	48.20	-	-	-	0.40	99.90	89	-	-
Exsolved Opx	54.71	0.24	5.54	0.55	7.88	0.13	30.46	0.97	0.37	-	-	100.85	87	-	-
Cpx	50.78	1.02	7.41	0.41	3.30	0.18	15.34	22.53	0.56	-	-	101.53	89	-	-
Opx (coarse lamella in Cpx)	55.68	0.26	2.07	0.46	7.44	0.25	33.39	0.72	-	-	-	100.27	89	-	-
Spl	-	0.55	52.49	15.03	15.06	0.24	16.63	-	-	-	-	100.00	66	16	-
Pl	51.82	0.01	31.16	0.05	0.04	-	0.11	13.89	3.70	-	-	100.78	-	-	67

Major element compositions of minerals were analysed using a JEOL-6400 electron microprobe equipped with a LINK-ISIS energy dispersive microanalytical system at the Department of Chemistry, Life Sciences and Environmental Sustainability of Parma University. The electron beam was produced at an accelerating voltage of 15 kV and probe current of 0.25 nA. Both natural minerals and synthetic
compounds were used as standards. pfc=porphyroclast, neo=neoblast, (-) below detection limit (< 0.10 wt%). Mineral abbreviations after Whitney and Evans (2010).

Table 2.3. Representative major element compositions (wt%) of minerals from Monte Sant'Agostino peridotites

	SiO_2	TiO_2	Al_2O_3	Cr_2O_3	FeO	MnO	MgO	CaO	Na_2O	K_2O	NiO	Total	Mg#	Cr#	An
MGO1 Mylonitic lherzolite															
Ol pfc	40.97	-	-	-	10.70	0.10	47.95	0.14	-	-	-	99.86	89	-	-
Cpx2 pfc core	51.24	0.42	8.42	0.99	2.70	0.10	14.21	19.60	2.06	-	-	99.74	90	-	-
Cpx pfc rim	51.63	0.65	5.92	0.85	2.66	-	15.11	22.52	0.93	-	-	100.27	91	-	-
Opx pfc core	54.84	0.33	4.73	0.56	6.65	-	32.83	0.70	-	-	-	100.64	90	-	-
Spl	-	0.15	59.59	9.90	11.55	0.29	18.70	-	-	-	-	100.18	74	10	-
IC8-1 Mylonitic lherzolite															
Ol pfc	41.27	-	-	-	10.31	0.07	48.37	-	-	-	0.49	100.51	89	-	-
Cpx pfc core	50.45	0.48	7.69	1.45	2.60	0.38	13.87	21.25	1.71	-	-	99.88	90	-	-
Opx pfc core	54.87	0.11	4.50	0.44	7.33	0.12	32.12	0.60	-	-	-	100.09	89	-	-
Spl pfc core	-	-	60.90	8.38	11.95	0.02	19.02	-	-	-	-	100.27	74	8	-
Amp	41.54	4.62	14.78	1.20	4.65	0.20	15.14	11.92	4.03	0.10	-	98.18	85	-	-
Ol neo	41.21	-	-	-	9.55	0.14	49.91	-	-	-	0.44	101.25	90	-	-
Cpx neo	52.80	0.51	2.94	0.27	2.75	0.10	17.00	23.20	0.56	-	-	100.13	92	-	-
Opx neo	55.82	0.10	1.62	0.25	7.23	0.32	35.61	0.34	-	-	-	101.29	90	-	-
Pl neo	55.41	-	27.78	-	0.27	-	-	8.75	7.04	-	-	99.25	-	-	41
IC8-3 Mylonitic lherzolite															
Cpx pfc core	50.65	0.52	8.02	0.55	2.95	0.17	13.83	20.69	1.76	-	-	99.14	89	-	-
Cpx pfc rim	51.56	0.42	7.39	0.76	2.52	-	14.95	20.46	1.44	-	-	99.51	91	-	-
Opx pfc core	54.59	0.25	5.01	0.44	7.00	0.17	32.10	0.70	-	-	-	100.26	89	-	-
Spl pfc core	-	0.15	57.60	11.43	12.72	0.37	17.91	-	-	-	-	100.18	72	12	-
Amp	42.19	3.59	14.54	1.02	6.00	0.17	17.17	10.91	2.81	0.26	-	98.66	84	-	-
Ol neo	40.84	-	-	-	9.86	0.18	49.31	0.10	-	-	0.30	100.59	90	-	-
Cpx neo	54.41	0.58	3.06	0.62	2.58	-	17.71	22.54	0.70	-	-	102.20	92	-	-
Opx neo	56.71	0.16	1.06	-	7.02	0.2	35.42	0.32	-	-	-	100.89	90	-	-
Pl neo	56.64	-	27.52	-	0.60	-	-	7.75	7.14	-	-	99.64	-	-	38
IC11 ultramylonitic lherzolite															
Cpx pfc core	54.75	0.56	6.54	0.83	3.93	0.10	15.14	21.11	1.44	-	-	104.40	87	-	-
Opx pfc core	55.35	0.31	3.65	0.14	6.56	0.22	33.42	0.56	-	-	-	100.21	90	-	-
Spl pfc core	-	-	57.74	10.52	11.93	0.25	19.52	-	-	-	0.36	100.32	76	11	-
Amp pfc	43.37	2.42	14.74	0.86	4.24	-	17.17	11.95	3.47	-		98.22	90	-	-
Ol neo	41.04	-	-	-	9.79	0.13	49.73	-	-	-	0.45	101.14	90	-	-
Cpx neo	54.77	0.23	2.23	0.25	2.39	-	17.92	23.37	0.54			101.70	93	-	-
Opx neo	55.70	-	0.74	0.10	7.06	0.14	35.65	0.28	-	-	-	99.67	90	-	-
Pl neo	54.17	-	-	-	0.29	-	-	10.41	5.82	-	-	70.69	-	-	50

Spl (neo)	-	-	55.13	10.49	13.47	0.12	20.49	-	-	-	0.28	99.98	80	11	-

pfc=porphyroclast, neo=neoblast, (-) below detection limit (< 0.10 wt%). Mineral abbreviations after Whitney and Evans (2010).

Table 2.4. Representative major element compositions (wt%) of minerals from Monte Sant'Agostino pyroxenites

	SiO_2	TiO_2	Al_2O_3	Cr_2O_3	FeO	MnO	MgO	CaO	Na_2O	K_2O	NiO	Total	Mg#	Cr#	An
MP7 Spinel websterite															
Cpx pfc core	49.64	0.66	9.41	0.23	4.68	0.26	13.40	20.40	1.27	-	-	99.92	84	-	-
Cpx pfc rim	49.81	0.77	8.33	0.51	3.99	0.15	14.17	20.99	0.97	-	-	99.68	86	-	-
Opx pfc core	51.81	0.13	6.86	0.07	10.67	0.43	28.97	0.62	-	-	-	99.56	83	-	-
Opx pfc rim	53.52	0.21	4.49	0.19	9.98	0.28	30.49	0.57	-	-	-	99.74	84	-	-
Cpx neo	50.24	0.77	7.33	0.18	5.07	0.20	14.25	21.72	0.77	-	-	100.52	83	-	-
Opx neo	54.30	0.20	2.72	-	11.07	0.36	30.43	0.48	-	-	-	99.57	83	-	-
Spl neo	-	0.09	65.28	1.30	16.58	0.15	17.96	-	-	-	-	101.35	66	1	-
Ol neo	38.42	-	-	-	17.07	0.31	42.79	-	-	-	-	98.59	82	-	-
Pl neo	52.48	-	29.72	-	-	-	-	10.25	4.92	-	-	97.37	-	-	54
Amp	41.32	4.23	14.36	0.64	6.71	0.13	15.06	11.91	2.93	0.45	-	97.74	80	-	-
Opx sym	54.02	0.22	3.57	-	10.91	0.35	30.44	0.52	-	-	-	100.02	83	-	-
Spl sym	-	0.09	63.55	0.74	16.86	0.27	16.95	-	-	-	-	98.46	64	1	-
Pl sym	52.90	-	30.18	-	-	-	-	10.19	5.19	0.18	-	98.64	-	-	52
AM489 Spinel websterite															
Cpx pfc core	49.79	0.63	9.17	0.34	3.35	0.21	13.51	21.82	0.73	-	-	99.55	88	-	-
Cpx pfc rim	52.61	0.58	4.42	0.57	2.64	0.15	15.83	23.02	0.52	-	-	100.35	91	-	-
Opx pfc core	54.07	-	6.52	0.23	7.57	0.19	31.40	0.51	-	-	-	100.47	88	-	-
Opx pfc rim	55.86	-	4.10	0.18	7.65	0.28	32.39	0.55	-	-	-	101.01	88	-	-
Ol neo	40.20	-	-	-	11.71	0.33	47.62	-	-	-	0.21	100.07	88		
Cpx neo	50.85	1.26	5.73		3.76	0.21	16.99	21.16	0.67	-	-	100.62	89	-	-
Opx neo	55.40	0.26	2.88		7.41	0.29	33.06	0.67	-	-	-	99.97	88	-	-
Spl neo	-	-	62.50	6.42	13.21	0.45	18.07	-	-	-	-	100.65	71	6	-
Pl neo	52.54	-	30.98	-	-	-	-	10.89	4.93	-	-	99.34	-	-	55
Amp	42.51	5.39	14.99	0.78	5.45	0.28	14.13	11.82	3.29	0.21	-	98.85	83	-	-

IC10-1 Spl websterite														
Cpx pfc core	53.94	0.30	4.75	0.15	-	9.41	0.28	30.58	0.74			100.13	85	
Opx pfc core	48.88	0.99	8.41	0.37	-	4.37	0.17	14.70	20.76	1.11		99.76	86	
Ol neo	39.86	-	-	-	13.19	0.07	45.16	0.21	-	-	-	98.48	86	
Opx neo	55.35	0.23	3.07	0.30	8.56	0.23	32.45	0.69	-	-	-	100.88	87	
Cpx neo	50.86	1.05	5.65	0.35	4.00	0.26	15.93	21.92	0.85	-	-	100.86	88	
Pl neo	52.93	-	30.06	-	0.47	-	-	10.96	5.06	-	-	99.47	-	54

pfc=porphyroclast, neo=neoblast, sym=symplectite, (-) below detection limit (< 0.10 wt%). Mineral abbreviations after Whitney and Evans (2010).

Table 2.5. Geotermobarometric estimates for the Monte Gavi and Monte Sant'Agostino mantle sections

Monte Gavi	$T_{Ca\text{-}in\text{-}Opx}$	T_{Ta98}	T_{BK90}	T_{HB94}	P_{FACE} (GPa)
Peridotites					
Exsolved Opx[(1)]- Cpx (core)	950-1110	878-916	897-938		
Type I- pyroxenites					
Non-exsolved Opx associated with Pl [(2)]	920-1030				
Opx - adjacent Cpx in Cpx-rich domain		850-954	876-989		
Pl-Amp				1030	0.67-0.78
Type II-pyroxenites					
Exsolved Opx[(1)]	1001-1047				
Non-exsolved Opx [(2)] associated with Pl	910-1065				
Opx - adjacent Cpx		970-983	996-1015		0.72
Monte S. Agostino					
Mylonitic peridotites					
Porphyroclastic Opx[(1)]- Cpx	930-970	832-886	857-950		
Neoblastic Pl-bearing mylonitic matrix [(3)]	750-780	756-825	788-873	778	0.34-0.55
Spl-Pl websterites					
Porphyroclastic Opx[(1)]- Cpx	920-985	914-958	940-960		
Neoblastic Pl-bearing matrix [(4)]	870-930	856-880	905-938		0.76-0.90
Pl-Amp				880-907	

Assumed P for $T_{Ca\text{-}in\text{-}Opx}$: [(1)] 1.5 GPa, [(2)] 0.7 GPa, [(3)] 0.4 GPa, [(4)] 0.8 GPa

Chapter 3
Insights on the Monte Gavi plagioclase-facies melt-rock reaction event

3.1. Introduction

The mantle rock bodies from the External Ligurian units (Northern Apennines, Italy) record distinct pressure-temperature evolutions, as well as deformation processes during the Mesozoic rifting stage that preceded the Jurassic Western Tethys opening. A relatively cold decompression evolution linked to the extensional tectonics is widely reported for several of these mantle bodies. Exhumation to plagioclase-facies conditions occurred statically in the Suvero mantle body (e.g., Hidas et al., 2020). Conversely, the Rio Strega-Monte Prinzera (Montanini et al., 2006) and Monte Sant'Agostino (PhD Thesis, Chapter 2) bodies provide evidence for dynamic plagioclase-facies recrystallization along hectometre-scale lithospheric shear zones. Furthermore, plagioclase-facies melt-rock reaction processes are recorded by the Monte Nero mantle body (Piccardo et al., 2004).

Plagioclase-facies melt-rock reaction processes were also reported in this PhD Thesis for the Monte Gavi mantle body (see Chapter 2). This mantle section consists of harzburgites interlayered with spinel pyroxenites levels, which were subdivided into Type-I and Type-II. Because of the melt-rock interaction event, both peridotites and pyroxenites underwent different replacement extents of: (i) clinopyroxene, by orthopyroxene + plagioclase, and (ii) spinel, by plagioclase. Type-I pyroxenites were subdivided in two sub-types (Ia and Ib) based on the different replacement extents. In particular, Type-Ib pyroxenites are characterized by (i) pyroxene-rich domains in which coarse clinopyroxene relics are associated to newly formed secondary orthopyroxene + plagioclase + clinopyroxene, and (ii) plagioclase-rich domains constituted by plagioclase + olivine + Cr-spinel presumably representing the reaction products between the percolating melt and original Al-spinel-rich domains. Conversely, in Type-Ia pyroxenites coarse clinopyroxene and spinel grains are well preserved, despite the local crystallization of orthopyroxene and plagioclase. Along with the petrographic evidence, mineral major element compositions also registers the effects of melt impregnation. In particular, an increase of Cr# values (up to 34) and TiO_2 contents (up to 1 wt%) is recorded by spinels from pyroxenites and enclosing peridotites. Moreover, reacted clinopyroxenes from pyroxenites display an increase in TiO_2 contents (up to 2.3 wt%). Overall, the percolating melt should have been

silica(orthopyroxene)-saturated and Ti-rich. According to the FACE geobarometer of Fumagalli et al. (2017), the plagioclase-facies melt-rock reaction process occurred at 0.7-0.8 GPa.

The aim of this Chapter is to assess the Monte Gavi melt impregnation event. New geochemical data on whole rocks and mineral phases will give additional insights on the nature of the percolating melt. Nd-Hf isotopic data from pyroxenite samples will be used to discuss the possible sources of this melt, besides providing age constraints on the melt-rock reaction event.

3.2. Geological and petrological framework

The Alpine-Apennine ophiolites represent lithospheric remnants of the Jurassic Western Tethys basin (also referred to as Ligurian-Piedmontese basin). Some ophiolites from the Central Alps (Malenco and Totalp; Müntener et al., 2004, 2010) and Northern Apennines (External Ligurian units; Rampone et al., 1995; Montanini et al., 2006, 2012) expose mantle bodies showing a subcontinental origin and were interpreted to be exhumed along the Western Tethys magma-poor ocean-continent transition. Other ophiolites from the Alpine-Apennine system (e.g. those from the Internal Ligurian Units) show affinities with oceanic lithosphere from slow and ultra-slow spreading ridges (Sanfilippo and Tribuzio, 2011; Tribuzio et al., 2014).

The External Ligurian (EL) ophiolites occur as slide blocks within Late Cretaceous sedimentary melanges formed during the convergence phase that led to the closure of the Western Tethys basin (e.g., Marroni et al., 2017). The cm- to km-sized slide blocks comprise subcontinental mantle rocks (e.g., Piccardo et al., 2004), Jurassic MOR-type gabbros and basalts (Tribuzio et al., 2004, 2016; Montanini et al., 2008) and associated pelagic sediments, Late Carboniferous-Early Permian granitoids (Ferrara and Tonarini, 1985) and mafic granulites (Meli et al., 1996).

Mantle rocks are mainly constituted by fertile spinel-plagioclase lherzolites (e.g., Rampone et al., 1995) locally bearing accessory amphibole (kaersutite to titanian pargasite). Peridotites are in places interlayered with garnet and spinel pyroxenites (Montanini et al., 2006, 2012; Montanini and Tribuzio, 2015; Borghini et al., 2016).

As reported in the previous Chapter 2, the External Ligurian subcontinental mantle sequences could be grouped in three main domains according to their rifting-related evolution preceding the opening of the Jurassic Western Tethys basin. A plagioclase-bearing spinel tectonite (ST) domain, exemplified by the Suvero section (e.g., Rampone et al., 1995), recorded a high-temperature (1000-1050 °C) spinel-facies deformation. A subsequent plagioclase-facies recrystallization occurred in Jurassic times under melt-absent static conditions (Borghini et al., 2016; Hidas et al., 2020). Two recrystallization stages were recognized, from 0.6-0.7 GPa and 890-910 °C to 0.4-0.5 GPa and 800-840 °C (Fumagalli et al., 2017) and were ascribed to the rifting-related decompression evolution. A

plagioclase mylonite (PM) domain, exemplified by the Rio Strega-Monte Prinzera (e.g., Montanini et al., 2006) and Monte Sant'Agostino sequences (PhD Thesis, Chapter 2), underwent extensive plagioclase-facies recrystallization which overprinted almost all the older tectonitic spinel-facies texture. Recrystallization is associated with mylonitic to ultramylonitic textures developed in hectometre-scale lithospheric shear zones. Deformation occurred at 0.3-0.6 GPa and 750-850 °C under melt-absent conditions. Montanini et al. (2006) reported Late Triassic ages for the plagioclase-facies deformation event. A plagioclase-impregnated (PI) domain, exemplified by Monte Nero (Rampone et al., 1995; Piccardo et al., 2004) and Monte Gavi (PhD Thesis, Chapter 2) sequences, is characterized by the reactive crystallization of plagioclase resulting from the interaction with a percolating melt at 0.6-0.8 GPa. No deformation structures are detected in these mantle sequences. The melt infiltration event is inferred to have occurred in Jurassic times, as indicated by the Sm-Nd clinopyroxene-plagioclase cooling ages of 163 ± 20 Ma and 165 ± 20 Ma obtained by Rampone et al. (1995).

The External Ligurian peridotites are mainly characterized by MORB-type Nd-Sr isotopic compositions, but highly radiogenic Nd isotopic compositions coupled to unradiogenic Sr and ancient Os model ages were locally observed (Snow et al., 2000; Montanini et al., 2012; Borghini et al., 2013, 2016) and argue for a long residence time in the subcontinental mantle. Nd-Hf isotopic compositions of pyroxenites cover a wide range of values, from highly depleted to enriched (Montanini et al., 2012; Montanini and Tribuzio, 2015; Borghini et al., 2021).

3.3. Methodology

Whole rock powders were prepared in order to analyse major, trace element and Nd-Hf isotopic compositions. Before making the powders, alteration was carefully removed from each rock sample using the diamond saw. Each rock sample was ground with a mortar until reaching a size less than 2 mm. The obtained granulate was reduced to powder (grain size < 2 μm) using an agate mill. Two additional powders were made for Type-Ib pyroxenite GA1, corresponding to pyroxene- and plagioclase-rich domains of this sample (see §2.4. Petrographic characteristics and major element mineral chemistry, Chapter 2). As the domains are well distinguishable on the hand specimen, a meticulous separation of the two was achieved using the diamond saw. The related powders are named GA1 Px-Rich Fraction and GA1 Pl-Rich Fraction. The mortar, the sieves and the agate mill were cleaned with water and alcohol between one sample and another to avoid any contamination.

Clinopyroxene separates from pyroxenite samples were obtained in order to get Nd and Hf isotopic compositions. After grinding and sieving of rock samples, clinopyroxenes were separated from the 355/180 μm granulate fractions by electromagnetic separation and handpicking.

Whole rock major and trace elements were analysed at Activation Laboratories (Ancaster, Ontario, Canada) by inductively coupled plasma (ICP) optical emission spectroscopy and ICP mass spectrometry. Precision and accuracy are estimated to be better than 2% for SiO_2, Al_2O_3, Fe_2O_3 and MgO and better than 5% for the other major elements. Precision and accuracy of trace element analyses are assessed to be within 10%.

Whole rock powders and clinopyroxene separates were processed in a clean laboratory at the Laboratoire Géosciences Océan (Université de Bretagne Occidentale, Brest, France) prior to Nd and Hf isotopic analyses. Chemical digestion of samples occurred in Anton Paar bombs using HF + $HClO_4$ for ~200 mg of rock powder and 150 mg of clinopyroxene separates. After digestion, each sample was leached in several steps by adding HF, HNO_3 and HCl. The leached sample was loaded on a Bio-Rad® AG1-X8 column that produced two elution. One elution was loaded on a Bio-Rad® AG50-X8 column to concentrate Rare Earth Elements which were subsequently purified for Nd by means of a LnSpec Eichrom resin column. The other elution was used for Hf purification, achieved by means of a Bio-Rad® AG50-X8 200-400 mesh column. Nd isotope ratios were quantified using a Thermo Scientific Triton Thermal Ionization Mass Spectrometer (TIMS) located at the Institut Universitaire Européen de la Mer (Brest, France). Internal standard La Jolla was repeatedly measured in order to test instrument accuracy. Hf isotope ratios were analysed using a Thermo Neptune MultiCollector Inductively Coupled Plasma Mass Spectrometer (MC-ICP-MS) located at the Ifremer Institute (Brest, France). AMES and JMC 475 were used as internal standards.

In situ trace element analyses of mineral phases were carried out using laser ablation ICP mass spectrometry at Istituto di Geoscienze e Georisorse - C.N.R., Unità di Pavia. The laser probe consisted of a Q-switched Nd:YAG laser, model Quantel (Brilliant), whose fundamental emission in the near-IR region (1064 nm) was converted into 213 nm wavelength using three harmonic generators (Jeffries et al., 1998). Spot diameter was typically ~40 μm. The ablated material was analysed by using an Elan DRC-e quadrupole mass spectrometer. Helium was utilized as carrier gas and mixed with Ar downstream of the ablation cell. NIST SRM 610 was used as external standard. The CaO content determined by electron microprobe was utilized as internal standard, scaled on the $^{44}Ca+$ signal. Precision and accuracy were assessed from repeated analyses of the BCR2-g standard and resulted better than 10% at ppm concentration level. Detection limits were typically in the range of 1.0-0.5 ppm for Cr and Ti, 0.5-0.1 ppm for Sc, 100-10 ppb for Sr, Zr, Ba, Rb, V and Gd, 10-1 ppb for Y, Nb, REE, Hf and Ta.

3.4. Whole rock compositions

Bulk rock major and trace element compositions of Monte Gavi pyroxenite samples are listed in Table 3.1. Major element compositions were recalculated on anhydrous basis and normalized to 100.

Monte Gavi pyroxenites show distinct Mg# values. In particular, Mg# values of Type-Ib samples cluster at 79-82, whilst higher values are displayed by the other pyroxenites (Type-Ia Mg# = 86, Type-II Mg# = 87-89). Mg# values variations in the three types of whole rocks are mirrored by similar variations in the Mg# values of clinopyroxenes (see §2.4. Petrographic characteristics and major element mineral chemistry, Chapter 2). Type-Ib rocks also show the highest TiO_2, Al_2O_3 and Na_2O contents (0.42-0.48, 14.06-14.44 and 0.49-0.54 wt%, respectively; Fig. 3.1). Collectively, Type-Ib and Type-II pyroxenites have higher TiO_2 contents compared to Type-Ia. This is consistent with the observation that Type-Ia pyroxenites were less affected by the interaction with the Ti-rich percolating melt (see also the Introduction).

The relatively low Mg# values of Type-Ib pyroxenites are coupled to lower Cr contents (620-890 ppm) compared to the other samples (2400-3300 ppm).

Similar Rare Earth Element concentrations (~1 to 10 times chondritic values) are displayed by the three pyroxenite groups, although three distinct patterns can be distinguished (Fig. 3.2). Type-Ib and Type-II have markedly LREE depleted patterns (La_N/Sm_N = 0.14-0.25 and 0.28-0.32, respectively) compared to the slight depletion shown by Type-Ia sample (La_N/Sm_N = 0.50). In addition, higher HREE concentrations are displayed by Type-Ib (Yb_N = 8.18-9.94) and Type-II (Yb_N = 6.00-6.88) whole rocks compared to Type-Ia (Yb_N = 3.29). On a Primitive Mantle normalized extended incompatible trace elements diagram (Fig. 3.3), all the pyroxenites exhibit increasing concentrations from La to Lu. Steeper patterns are displayed by Type-Ib and Type-II samples, which have distinct higher absolute concentrations from Zr to Lu compared to Type-Ia. Prominent Ti negative anomalies are shown by Type-Ib samples.

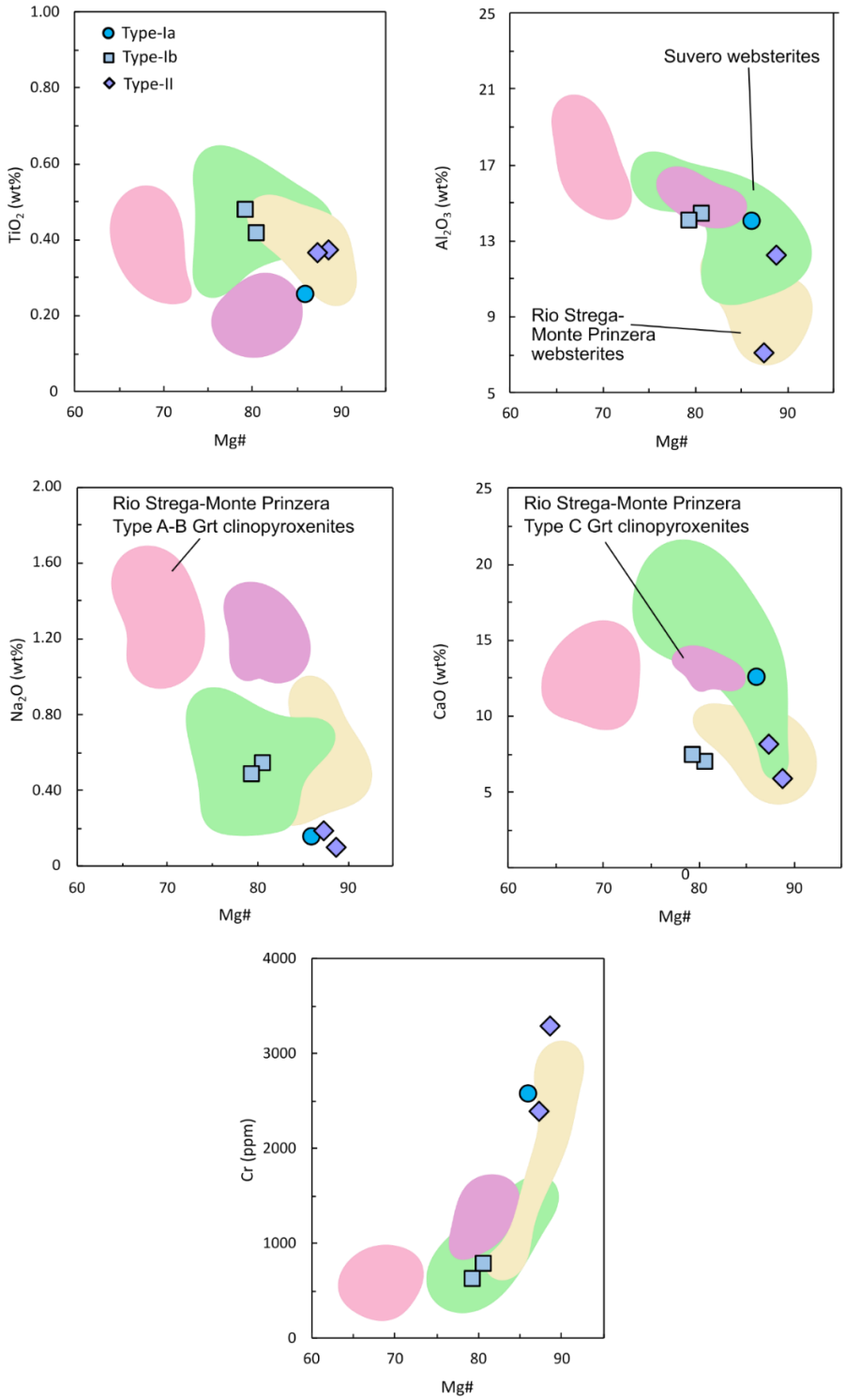

Fig. 3.1. Whole rock TiO_2, Al_2O_3, Na_2O, CaO and Cr contents vs. Mg# values plots of Monte Gavi pyroxenites. Data from External Ligurian Suvero (Borghini et al., 2016) and Rio Strega-Monte Prinzera (Montanini et al., 2012; Montanini and Tribuzio, 2015) pyroxenites are shown for comparison.

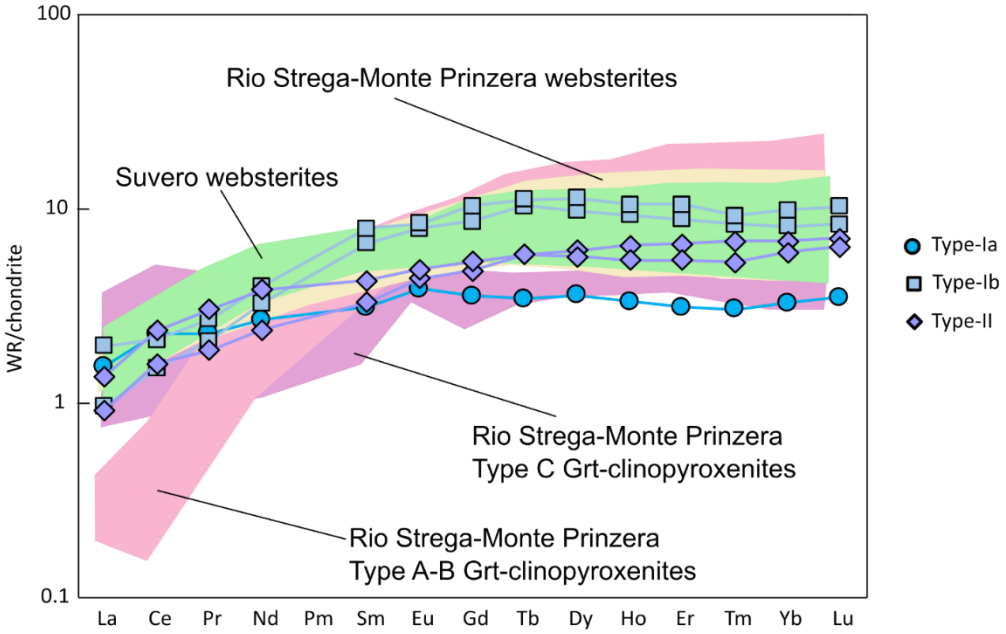

Fig. 3.2. Whole rock Rare Earth Elements patterns of Monte Gavi pyroxenites normalized to chondrite (normalizing values after Sun and McDonough, 1989). Data from External Ligurian Suvero (Borghini et al., 2016) and Rio Strega-Monte Prinzera (Montanini et al., 2012; Montanini and Tribuzio, 2015) pyroxenites are shown for comparison.

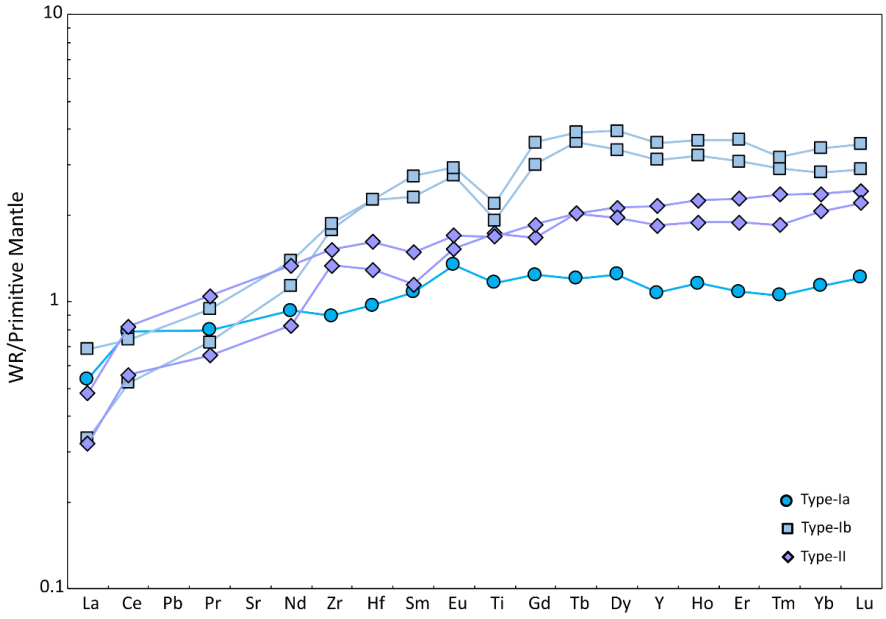

Fig. 3.3. Whole rock incompatible trace element diagram of Monte Gavi pyroxenites normalized to primitive mantle (normalizing values after Sun and McDonough, 1989).

3.5. Mineral trace element compositions

Representative trace element compositions are listed in Table 3.2. They have been carried out for (i) Monte Gavi harzburgite MGA7, (ii) Type-Ia pyroxenite GAV2, Type Ib pyroxenites GA1 and MG6 and (iii) Type-II pyroxenite MG5. Trace element analyses were mainly performed on clinopyroxene grains. A few representative analyses of orthopyroxene and plagioclase grains are also described.

Clinopyroxene from Monte Gavi peridotite shows LREE depletion (La_N/Sm_N = 0.09-0.13) and nearly flat to slightly depleted HREE (Gd_N/Yb_N = 1.1-1.4). Two distinct REE patterns are displayed by the clinopyroxenes from the pyroxenitic samples. Clinopyroxene from Type-Ia pyroxenite (Fig. 3.4b) has depleted LREE (La_N/Sm_N = 0.2-0.3) and flat to fractionated MREE-HREE (Gd_N/Yb_N = 1.0-1.7). Clinopyroxenes from Type-Ib and Type-II pyroxenites show distinct REE patterns. In particular, they have a marked LREE depletion (La_N/Sm_N = 0.01-0.05), a strong negative Eu anomaly (Eu/Eu* = 0.5-0.7) and flat to slightly depleted HREE (Gd_N/Yb_N = 1.0-1.3). M- and HREE concentrations are up to ~10 times higher than those in Type-Ia clinopyroxene, reaching ~100 times chondritic values (Fig. 3.4). Another distinctive feature of Type-Ib and Type-II clinopyroxenes is the more pronounced negative Sr anomaly compared to that of Type-Ia clinopyroxene (Fig. 3.5). In addition, the two groups of clinopyroxenes have distinct Zr/Nd and Ce/Y ratios (Fig. 3.6). In particular, Type-Ib and Type-II clinopyroxenes show higher Zr/Nd ratios coupled to lower Ce/Y ratios. No compositional variations were observed between core and rim.

Orthopyroxenes from the harzburgite sample MGA7 have REE compositions progressively increasing from LREE to HREE (from ~0.05 to ~5 times chondritic values) describing a fairly gentle concave upward pattern (Ce_N/Yb_N = 0.01-0.02; Fig. 3.7). Orthopyroxene and plagioclase from Type-Ib pyroxenites were also analysed. Orthopyroxene has compositions gradually increasing from LREE to HREE (from ~0.05 to ~15 times chondritic values). Its REE pattern is characterized by a slightly enriched La-Ce segment and a negative Eu anomaly (Eu/Eu* = 0.4). Plagioclase has a marked positive Eu anomaly (Eu/Eu* = 4.9-7.6) and a concave upward La-Sm segment. Its REE concentrations are mostly comprised between 1 and 10 times chondritic values (Fig. 3.8).

Trace element compositions of pyroxenes from Monte Sant'Agostino mylonitic lherzolites (MGO1, IC8-1 and IC8-3) and one spinel websterite (AM489) are reported in Table 3.3 and Figures 3.4,3.5,3.6,3.7 for comparative purposes. Clinopyroxene from peridotites is slightly depleted in LREE (La_N/Sm_N = 0.3-0.6) and has mostly flat HREE (Gd_N/Yb_N = 0.9-1.1). Orthopyroxene REE concentrations increase from ~0.001 to ~5 times chondritic values, from L- to HREE, showing steep patterns (La_N/Lu_N = 0.001-0.04). Clinopyroxene from spinel websterite AM489 displays LREE

depletion (La_N/Sm_N = 0.1-0.3) coupled to variably enriched HREE (Gd_N/Yb_N = 0.4-0.9) and no to weak negative Eu anomalies (Eu/Eu* = 0.7-1.1). Strong negative Sr anomalies and small negative Hf anomalies are also visible. Orthopyroxenes display progressively increasing concentrations from LREE to HREE (from ~0.01 to ~10 times chondritic values). No compositional variations were observed between core and rim of pyroxenes from both lherzolites and websterites.

3.6. Geothermometric estimates

Trace element analyses of pyroxenes and plagioclase were employed to calculate temperatures based on slowly diffusing elements (REE, Y) according to the calibrations of Liang et al. (2013) and Sun and Liang (2017). The former is based on the REE-Y partitioning between coexisting clinopyroxene and orthopyroxene, whilst the latter is based on the REE-Y partitioning between coexisting clinopyroxene and plagioclase. The obtained estimates are reported in Table 3.4.

Porphyroclastic clinopyroxene-orthopyroxene pairs from Monte Gavi harzburgite MGA7 yielded values of 1245 ± 90 °C. Calculated temperatures for coarse clinopyroxene and associated orthopyroxene in Type-Ib MG6 pyroxenite returned 1278 ± 32 °C. By using the calibration of Sun and Liang (2017) for Type-Ib coarse clinopyroxene grains and plagioclase, temperatures of 1257 ± 48 (MG6) and 1170 ± 14 °C (GA1) were obtained.

The geothermometer of Liang et al. (2013) was also applied on the porphyroclastic clinopyroxene-orthopyroxene pairs from Monte Sant'Agostino samples for comparative purposes. Three mylonitic lherzolites (MGO1, IC8-1, IC8-3) returned a weighted average temperature of 1044 ± 43 °C (MSWD = 0.39). The spinel websterite AM489 yielded values of 1103 ± 78 °C.

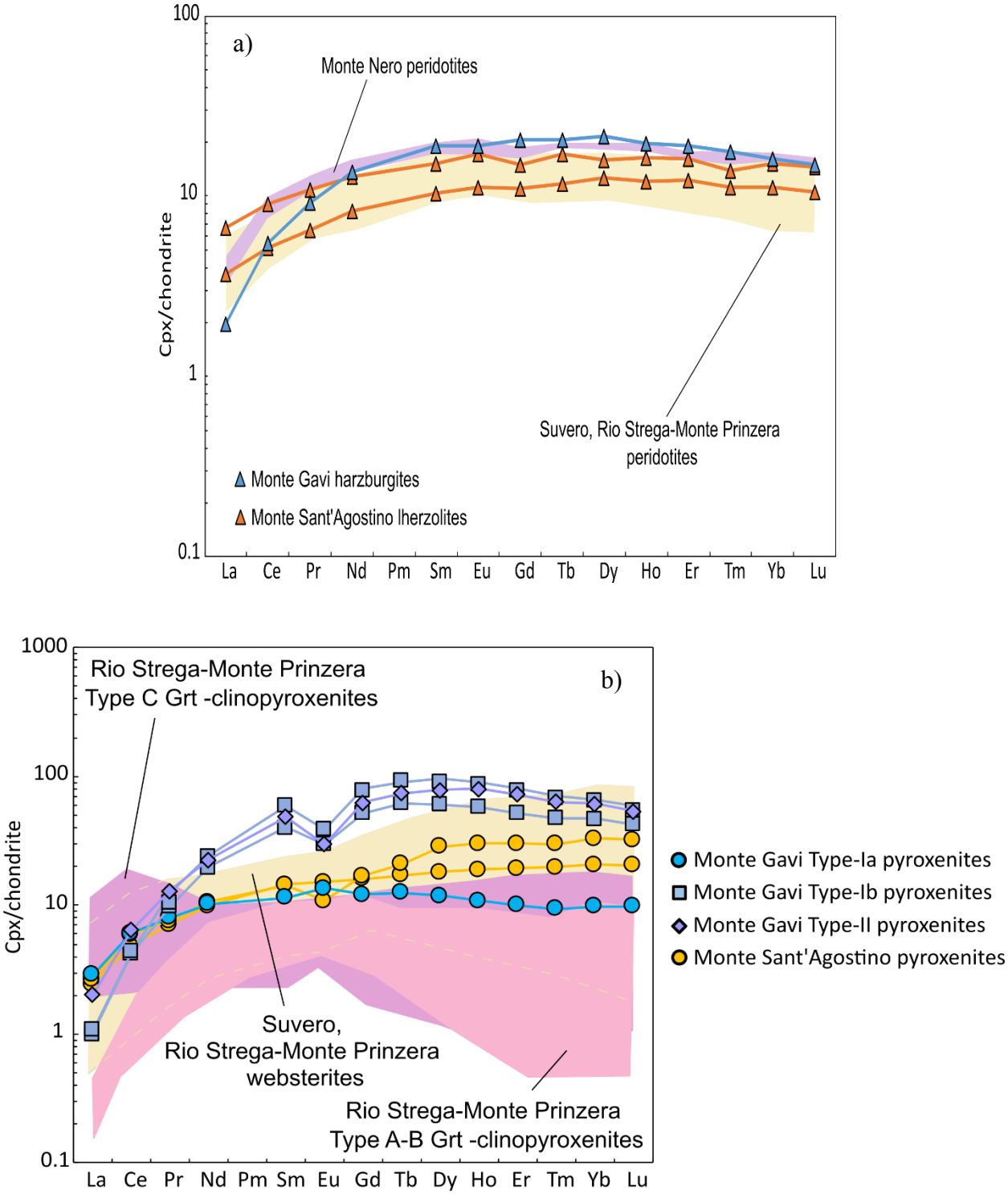

Fig. 3.4. Representative Rare Earth Element compositions normalized to chondrite (normalizing values after Sun and McDonough, 1989) of clinopyroxene cores from Monte Gavi (a) peridotites and (b) pyroxenites. Data from Suvero (Borghini et al., 2016, 2020), Rio Strega-Monte Prinzera (Montanini et al., 2012; Montanini and Tribuzio, 2015; Montanini unpublished data) and Monte Nero (Piccardo et al., 2004) External Ligurian mantle sequences are shown for comparison. Representative clinopyroxene REE compositions from Monte Sant'Agostino section are also reported. Noteworthy, clinopyroxenes from Monte Sant'Agostino lherzolites have REE patterns similar to Suvero and Rio Strega-Monte Prinzera peridotites; clinopyroxenes from Monte Sant'Agostino spinel websterites have REE patterns comparable to the other External Ligurian websterites.

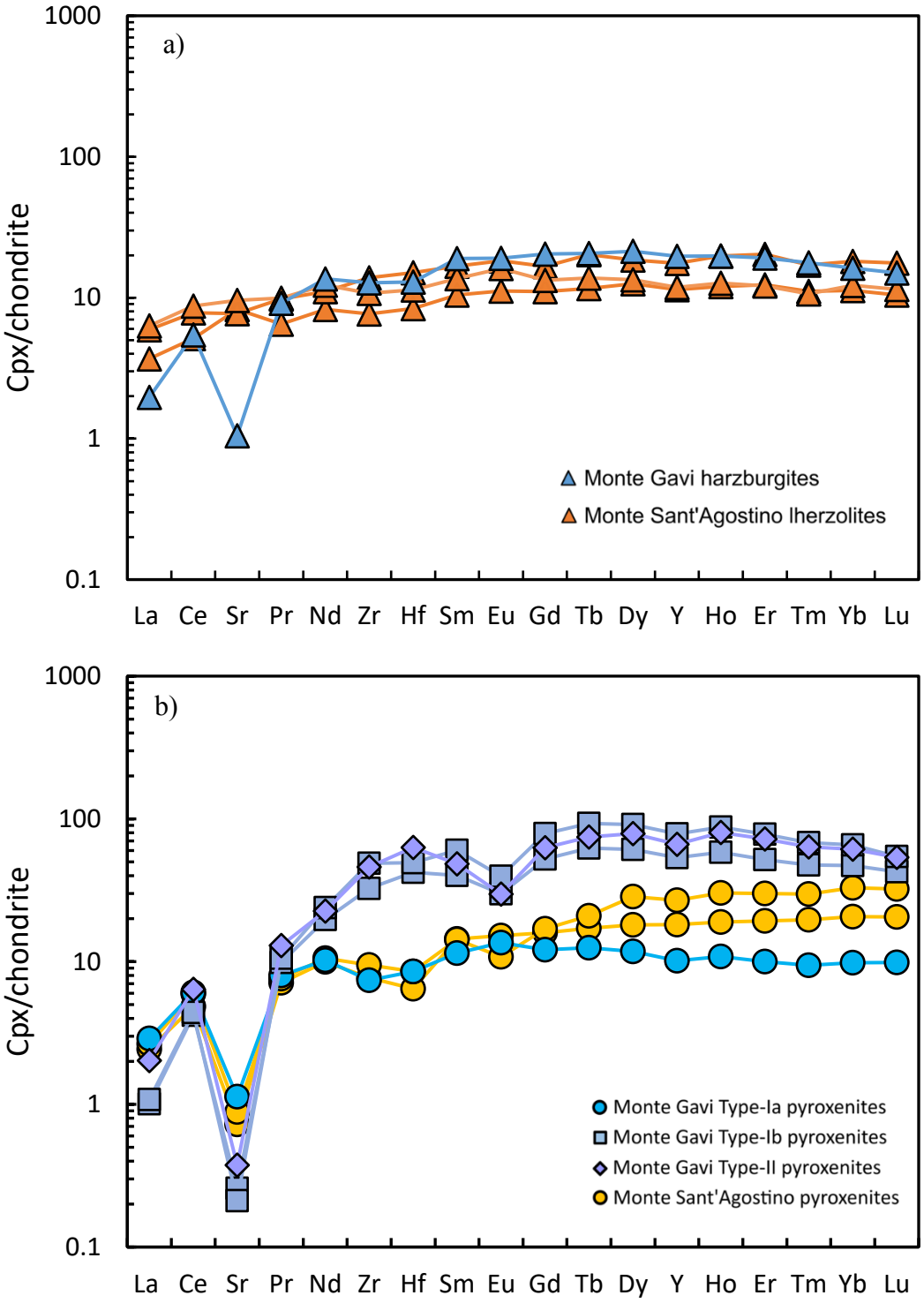

Fig. 3.5. Representative extended incompatible elements compositions normalized to chondrite (normalizing values after Sun and McDonough, 1989) of clinopyroxene cores from Monte Gavi (a) peridotites and (b) pyroxenites. Representative clinopyroxene REE compositions from Monte Sant'Agostino section are also reported for comparative purposes.

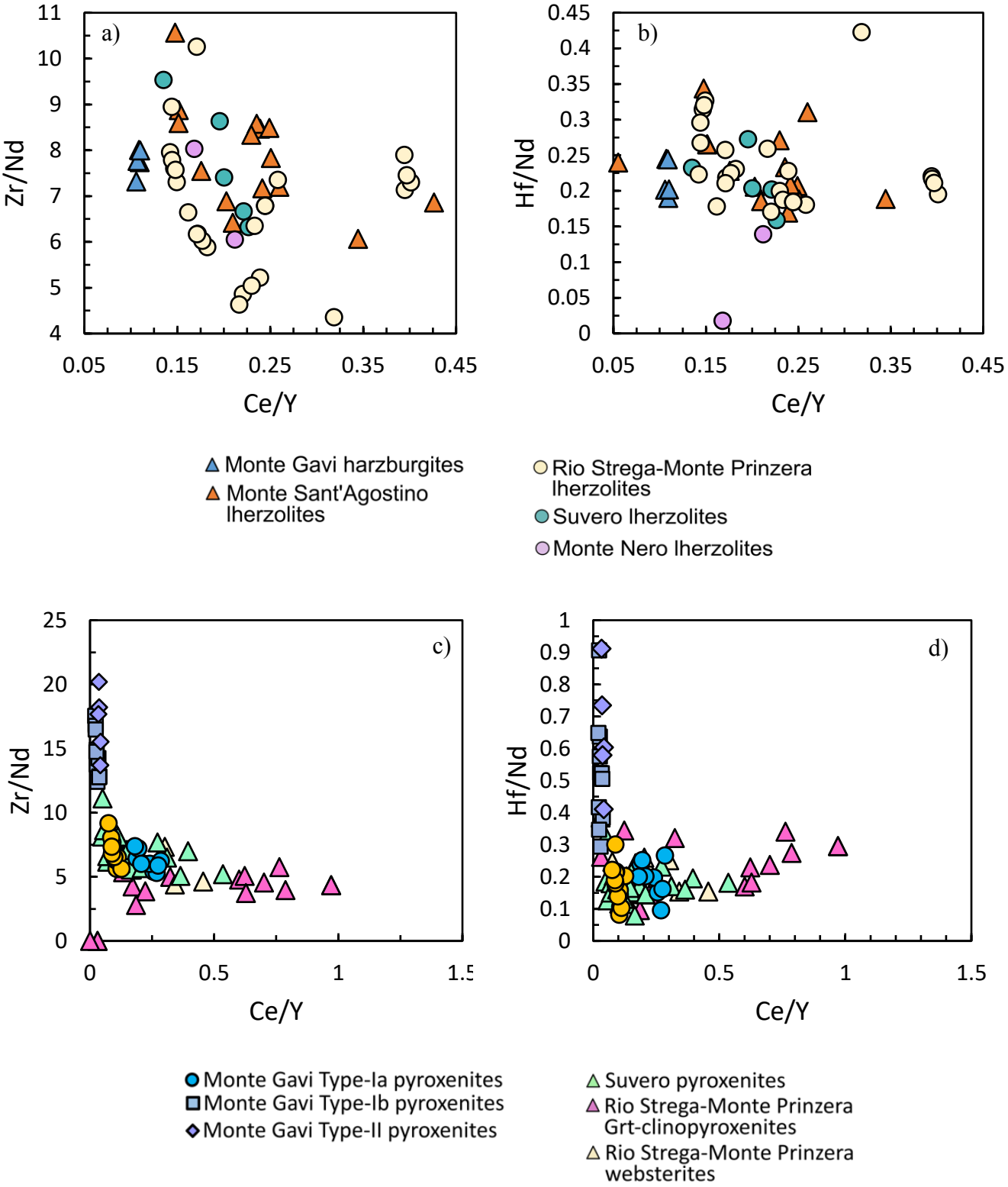

Fig. 3.6. Zr/Nd and Hf/Nd vs. Ce/Y plots of clinopyroxenes from Monte Gavi (a, b) peridotites and (c, d) pyroxenites. Data from Monte Sant'Agostino, Suvero, Rio Strega-Monte Prinzera and Monte Nero mantle sequences are shown for comparison.

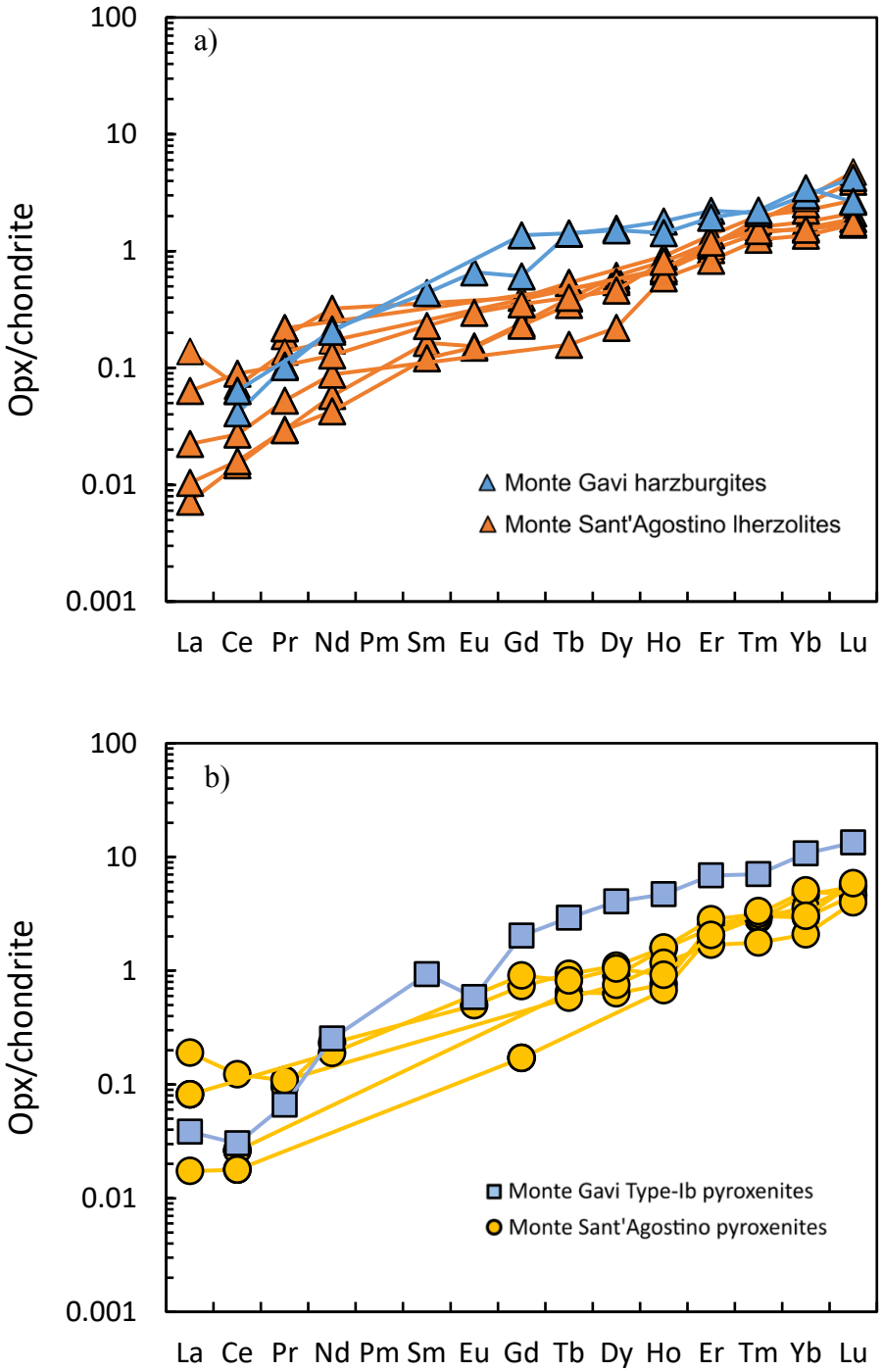

Fig. 3.7. Representative Rare Earth Element compositions normalized to chondrite (normalizing values after Sun and McDonough, 1989) of orthopyroxene cores from Monte Gavi (a) peridotites and (b) pyroxenites. Data from Monte Sant'Agostino are shown for comparison.

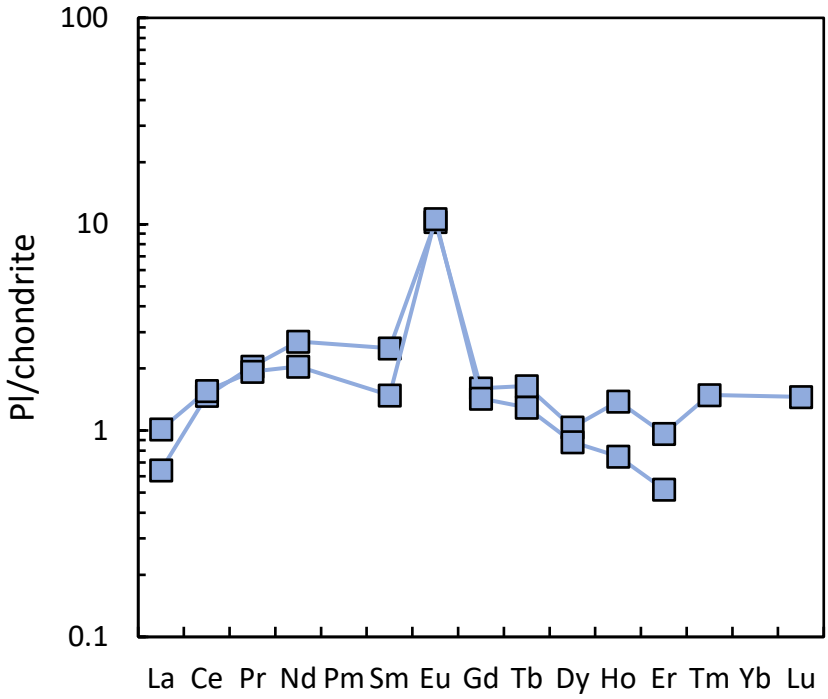

Fig. 3.8. Representative Rare Earth Element compositions normalized to chondrite (normalizing values after Sun and McDonough, 1989) of Monte Gavi plagioclase from Type-Ib pyroxenites.

3.7. Nd-Hf isotopic compositions

Sm-Nd isotope analyses were performed on 6 whole rock powders (GAV2, GA1, GA1 Px-Rich Fraction, GA1 Pl-Rich Fraction, MG6, IC2/3) and 4 clinopyroxene separates (GAV2, GA1, MG6, MG5) from both Type-I and Type-II pyroxenite samples. Additional Lu-Hf isotopic compositions were obtained for the same clinopyroxene separates (Tab. 3.5).

Present-day $^{143}Nd/^{144}Nd$ ratios of Type-Ia whole rock and clinopyroxene (sample GAV2) describe a narrow range (0.513148 and 0.513133, respectively) coupled to similar $^{147}Sm/^{144}Nd$ ratios (0.27 and 0.22, respectively). A positive correlation between $^{143}Nd/^{144}Nd$ and $^{147}Sm/^{144}Nd$ ratios is depicted by Type-Ib samples (Fig. 3.9) which show a wide range of $^{143}Nd/^{144}Nd$ (0.512816-0.513252) and $^{147}Sm/^{144}Nd$ (0.17-0.50) values. The lowest Sm-Nd ratios are displayed by GA1 Plagioclase-Rich Fraction. Type-II pyroxenites have $^{143}Nd/^{144}Nd$ and $^{147}Sm/^{144}Nd$ values ranging from 0.512896 to 0.513166 and from 0.22 to 0.43, respectively. Type-II pyroxenite samples plot along the alignment described by Type-Ib samples.

A consistent errorchron of 210 ± 20 Ma (n = 8; initial ε_{Nd} = +4.25; MSWD = 9.8) was obtained by plotting all Type-Ib and Type-II samples together (Fig. 3.10). The four GA1 samples (whole rock, Plagioclase-Rich Fraction, Pyroxene-rich Fraction and clinopyroxene separate) define an errorchron (Fig. 3.11) which yielded a similar age (217 ± 36 Ma, initial ε_{Nd} = +3.75; MSWD = 9.2).

Type-Ib clinopyroxenes show $^{176}Hf/^{177}Hf$ values ranging from 0.282934 to 0.283008 and $^{176}Lu/^{177}Hf$ values varying within a small range (0.03-0.04). Type-II clinopyroxene has $^{176}Hf/^{177}Hf$ ratios (0.282983) at $^{176}Lu/^{177}Hf$ values (0.03) similar to Type-Ib clinopyroxenes. Type-Ia clinopyroxene shows higher $^{176}Hf/^{177}Hf$ ratios (0.283339) at nearly similar $^{176}Lu/^{177}Hf$ ratios (0.04) compared to Type-Ib samples.

Initial Nd-Hf compositions of clinopyroxene separates were then computed at 210 Ma, which is the value returned by the Sm-Nd errorchron defined by Type-Ib and Type-II pyroxenites. Type-Ib and Type-II samples show a narrow interval of $\varepsilon_{Nd(210)}$ values (+3.97 to +4.18) at $\varepsilon_{Hf(210)}$ values varying from +5.29 to +8.80. Overall, the Nd-Hf isotopic composition of the Monte Gavi pyroxenites recalculated for the age provided by the Sm-Nd errorchron are poorly radiogenic and plot close or slightly below the mantle Nd-Hf array (Fig. 3.12). In contrast, Type-Ia clinopyroxene GAV2 has distinctly higher $\varepsilon_{Nd(210)}$ (+8.93) and $\varepsilon_{Hf(210)}$ (+19.25) values, falling in the more depleted portion of the MORB field, above the mantle array.

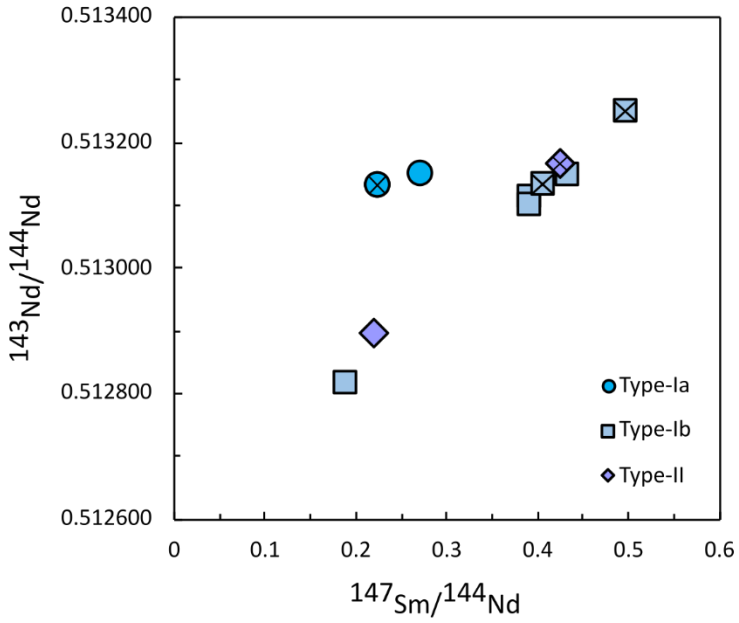

Fig. 3.9. Sm-Nd plot for whole rocks and clinopyroxene separates of Monte Gavi pyroxenite samples (clinopyroxene separates are distinguished by a cross).

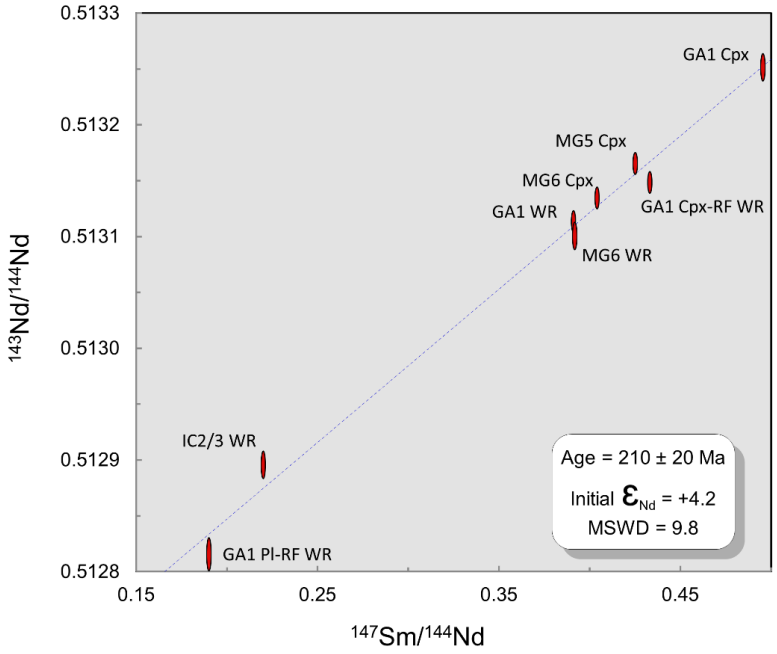

Fig. 3.10. $^{143}Nd/^{144}Nd$ vs. $^{147}Sm/^{144}Nd$ correlation diagram for all Type-Ib and Type-II pyroxenites. Data-point error ellipses are 2σ.

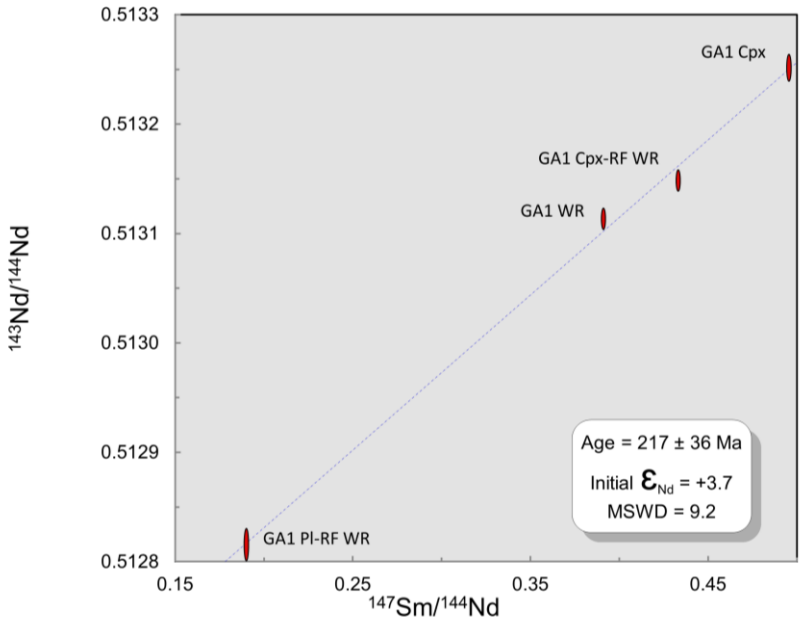

Fig. 3.11. $^{143}Nd/^{144}Nd$ vs. $^{147}Sm/^{144}Nd$ correlation diagram for GA1 samples. Data-point error ellipses are 2σ.

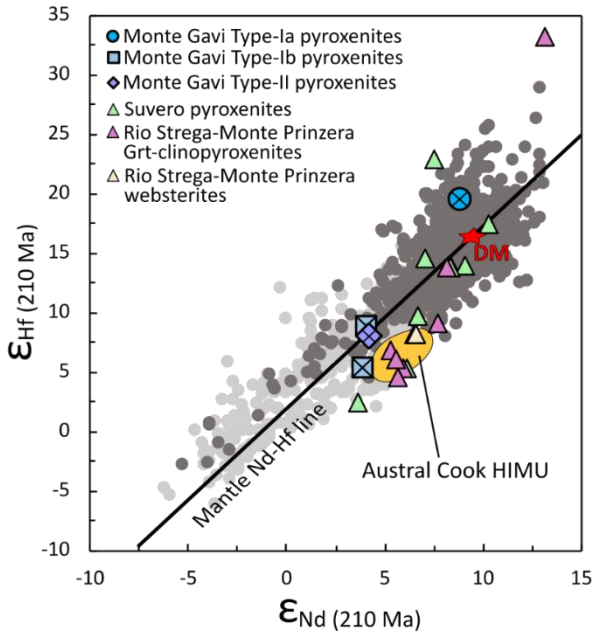

Fig. 3.12. ε_{Hf}-ε_{Nd} diagram for clinopyroxene separates of Monte Gavi pyroxenite samples. ε_{Hf} and ε_{Nd} values are calculated at 210 Ma. MORB (dark grey dots), OIB (light grey dots) and HIMU fields and the mantle Nd-Hf line are from Stracke (2012). The Depleted Mantle (DM) values are after Faure (1986) and Griffin et al. (2000).

3.8. Discussion

3.8.1. Geochemical response to plagioclase-facies melt infiltration

Melt-rock reaction in the Monte Gavi mantle section triggered some major elements modifications in spinels (Cr# values and TiO_2 contents) and clinopyroxenes (TiO_2 contents) from both peridotites and pyroxenites (see §2.6.1. Monte Gavi: a mantle section recording reactive melt infiltration in the plagioclase stability field, Chapter 2). Trace element compositions of clinopyroxene bear further evidence of the melt infiltration process. Clinopyroxenes from Monte Gavi harzburgites display distinct REE patterns compared to the clinopyroxenes of the other External Ligurian peridotites not affected by plagioclase-facies melt impregnation (e.g., Suvero, Rio Strega-Monte Prinzera and Monte Sant'Agostino mantle sequences; Fig. 3.4). In particular, Monte Gavi clinopyroxenes are more LREE-depleted and show higher HREE concentrations. Their REE patterns also differ from those of Monte Nero peridotites, the other External Ligurian plagioclase-impregnated mantle domain (see §2.6.4. The heterogeneity of the External Ligurian subcontinental mantle, Chapter 2). This suggests that the Monte Gavi and Monte Nero mantle sections interacted with geochemically distinct melts.

Clinopyroxenes from Monte Gavi peridotites testify the melt-rock reaction event also in having relatively high Zr contents coupled with relatively low Sr contents (Fig. 3.13). Following Müntener et al. (2010), who studied plagioclase peridotites from the Lower Platta unit, the high Zr/Sr ratios of Monte Gavi clinopyroxenes cannot be explained by a peridotite melting model. Instead, they are consistent with refertilization models, i.e. interaction with an infiltrating melt. The plagioclase-impregnated Monte Nero peridotites follow this trend as well, whilst the other External Ligurian peridotites generally exhibit higher Sr contents coupled with lower Zr contents.

Monte Gavi Type-I and Type-II pyroxenites recorded different extents of melt-rock interaction. Specifically, textural and mineral major elements evidence indicate that Type-Ia pyroxenites were not significantly affected by reaction with a percolating melt (see §2.6.1. Monte Gavi: a mantle section recording reactive melt infiltration in the plagioclase stability field, Chapter 2). Therefore, the REE patterns of Type-Ia clinopyroxenes presumably represent the composition prior to melt-rock reaction. Melt impregnation extensively modified the REE compositions of Type-Ib and Type-II clinopyroxenes, producing strong depletions in LREE, marked Eu anomalies and HREE enrichments (Fig. 3.4). Type-Ib and Type-II clinopyroxenes share analogous patterns, implying that the two distinct types of Monte Gavi pyroxenites reacted with the same percolating melt. Such clinopyroxene REE patterns are not displayed by the other External Ligurian pyroxenites (Fig. 3.4). The geochemical

modifications produced by the melt-rock process are also evident in the distinct REE compositions of Type-Ia vs. Type-Ib and Type-II whole rocks (Fig. 3.2).

The marked LREE-depletion and the higher absolute concentrations in HREE recorded by clinopyroxene of Monte Gavi peridotites and pyroxenites are thus indicative of the infiltrating melt. Such a depleted melt is not compatible with a typical MORB-type melt. Several authors have documented the presence of similar depleted melts in oceanic and ophiolitic mantle sequences from ultra-slow spreading settings (e.g., Dantas et al., 2007; Dijkstra et al., 2003; Basch et al., 2018, 2019). They were interpreted as non-aggregated incremental melts derived from fractional melting of a DMM source. The relatively SiO_2-rich composition of the reactively infiltrating melts could be achieved after reactive dissolution of mantle pyroxenes during melt migration in the extending lithosphere (Rampone et al, 2020 and quoted references).

A selective enrichment in Zr and Hf contents is displayed by Type-Ib and Type-II clinopyroxenes and could be ascribed to melt-rock reaction. Indeed, the most preserved Type-Ia clinopyroxenes have lower Zr/Nd and Hf/Nd ratios (Fig. 3.6) in accordance with clinopyroxenes from the other External Ligurian pyroxenites. Zr and Hf contents do not change significantly in clinopyroxenes from peridotites. The systematic lowering of Ce/Y ratios observed for Monte Gavi clinopyroxenes from both peridotites and pyroxenites reflects the pronounced LREE depletion.

In summary, the Monte Gavi mantle section was percolated by silica(orthopyroxene)-saturated, Ti-rich (see §2.6.1. Monte Gavi: a mantle section recording reactive melt infiltration in the plagioclase stability field, Chapter 2), LREE depleted melts.

3.8.2. Thermal evolution of the Monte Gavi sequence

Geothermometers of Liang et al. (2013) and Sun and Liang (2017) based on slowly diffusing elements (REE, Y) applied to Monte Gavi peridotites and pyroxenites gave temperatures > 1170 °C. These relatively high values are consistent with the interaction with asthenospheric melts and may be attributed to the plagioclase-facies melt impregnation event. Two-pyroxene and Ca-in-orthopyroxene geothermometers of Brey and Köhler (1990) furnished lower values (~930-980 and ~990-1000 °C, respectively) on the same pyroxene pairs used for the T_{REE-Y} (Tab. 3.4), presumably reflecting subsolidus re-equilibration after melt impregnation.

Overall, the high temperatures recorded by the Monte Gavi mantle sequence are comparable with those inferred for the plagioclase-facies granoblastic assemblage from the Monte Nero peridotites (1120-1140 °C; see §2.6.4. The heterogeneity of the External Ligurian subcontinental mantle, Chapter 2), thus arguing that the two mantle sections represent domains subject to heating during the plagioclase-facies rifting evolution.

In comparison, lower T_{REE-Y} values (~1040-1100 °C) were yielded by the porphyroclastic pyroxenes from Monte Sant'Agostino peridotites and pyroxenites. They likely preserve the thermal conditions of the spinel-facies equilibration stage and suggest no further heating of the mantle section, as testified by the colder plagioclase-facies evolution compared to the Monte Gavi sequence (see also §2.6.4. The heterogeneity of the External Ligurian subcontinental mantle, Chapter 2). Monte Sant'Agostino $T_{Ca\text{-}in\text{-}Opx}$ (~920-990 °C) referred to the porphyroclastic assemblage are lower than the corresponding T_{REE-Y} and could represent minimum temperatures of the spinel-facies phase, indicating a cooling process (Tab. 3.4).

3.8.3. Isotopic constraints on the melt infiltration event

Nd isotopic compositions of Monte Gavi pyroxenite samples possibly reflect different extent of melt-rock reaction recorded by Type-Ia, Type-Ib and Type-II rocks. In the $^{143}Nd/^{144}Nd$ vs. $^{147}Sm/^{144}Nd$ diagram (Fig. 3.9), Type-Ia samples do not plot along the linear correlation depicted by Type-Ib and Type-II samples. It could be speculated that melt-rock interaction experienced by Type-Ib and Type-II samples led to substantial re-equilibration of the Sm-Nd isotopic system. In this view, the errorchron of 210 ± 20 Ma (MSWD = 9.8) may correspond to the timing of the melt infiltration event. In this view, the initial ε_{Nd} of +4.3 could represent the isotopic composition of the percolating melt. The Nd-Hf isotopic compositions calculated at 210 Ma highlight the distinction between Type-Ia, Type Ib and Type-II pyroxenites (Fig. 3.12), with the Type-Ia clinopyroxene separate displaying the most radiogenic Nd and Hf compositions ($\varepsilon_{Nd(210)}$ = +8.9; $\varepsilon_{Hf(210)}$ = +19.3) and therefore lying above the mantle array, in the depleted portion of the MORB field. Following the notion that Type-Ia pyroxenites were least affected by the melt-rock reaction event, this Nd-Hf isotopic signature could reflect those of Type-Ia pyroxenite protoliths before melt-rock interaction. Some of the External Ligurian pyroxenites show a similar decoupling towards radiogenic ε_{Hf} values, which was explained by a time-integrated growth related to high Lu/Hf ratios of the protolith (e.g., Montanini and Tribuzio, 2015).

The $\varepsilon_{Nd(210)}$ and $\varepsilon_{Hf(210)}$ values of Type-Ib and Type-II pyroxenites calculated at 210 Ma plot slightly below the mantle array, in the enriched portion of the MORB field (Fig. 3.12). The $\varepsilon_{Hf(210)}$ range observed for these pyroxenites could be due to an incomplete reset of the Lu-Hf isotopic system. Some decoupling of Sm-Nd and Lu-Hf isotope systems during melt-rock interaction is commonly reported in the literature (Le Roux et al., 2009; Stracke et al., 2011; Guarnieri et al., 2012; Rampone

and Hofmann, 2012). Collectively, the $\varepsilon_{Nd(210)}$ and $\varepsilon_{Hf(210)}$ compositions of Type-Ib and Type-II pyroxenites may represent the Nd-Hf isotopic signature of the impregnating melt, which would be slightly enriched compared to a DMM source. Hence, the involvement of an isotopically enriched mantle component should be envisaged for the source of the impregnating melt.

Taking into account the orthopyroxene-saturated nature of this melt, we speculate that the impregnating melt was derived from a pyroxenite-dominated source. Pyroxenites from the External Ligurian units showing $\varepsilon_{Nd(210)}$ and $\varepsilon_{Hf(210)}$ compositions broadly comparable to those of Type-Ib and Type-II rocks were reported in the literature for the Suvero (Borghini et al., 2021) and Rio Strega-Monte Prinzera mantle sequences (Montanini et al., 2012; Montanini and Tribuzio, 2015). The Monte Gavi impregnating melt could derive from similar pyroxenites present in the late Triassic at deep mantle levels. In particular, Borghini et al. (2021) discussed the role of secondary high-MgO pyroxenites as a source of low radiogenic Nd-Hf isotopic compositions and their role in modifying the isotopic signature of the host peridotite, which is converted into an enriched peridotite. Partial melts from these secondary pyroxenites could be also a good candidate for the Monte Gavi impregnating melt. As a further hypothesis, following the reasoning of Borghini et al. (2021), a deeper veined mantle (i.e., a mantle sequence constituted by three components: a depleted peridotite + an enriched peridotite + a secondary high MgO pyroxenite) could generate melts with enriched Nd-Hf isotopic compositions. In this case, the orthopyroxene-saturation would be progressively acquired by the melts during their reactive ascent towards shallower, plagioclase-facies conditions.

3.8.3.1. The Upper Triassic melt impregnation event

In the framework of the geodynamic evolution of the External Ligurian mantle, the errorchron of 210 ± 20 Ma (MSWD = 9.8) attributed to the melt infiltration event (see §Isotopic constraints on the melt infiltration event) point to a process linked to the onset of Mesozoic rifting stage that preceded the opening of the Western Tethys basin (e.g., Villa et al., 2000). Similarly to Monte Gavi, the Monte Nero mantle section recorded a plagioclase-facies melt-rock reaction event. However, the melt impregnation of Monte Nero section likely occurred in Jurassic times, according to the Sm-Nd clinopyroxene-plagioclase two-point alignments of 163 ± 20 Ma and 165 ± 20 Ma reported by Rampone et al. (1995).

This observation indicates that the plagioclase-impregnated domains of the External Ligurian mantle (see §2.6.4. The heterogeneity of the External Ligurian subcontinental mantle, Chapter 2) recorded at least two distinct plagioclase-facies melt-rock interaction processes. This is also supported by the geochemical differences of the reacted clinopyroxene grains from Monte Gavi and Monte Nero

peridotites (see §Geochemical response to plagioclase-facies melt infiltration) and by the occurrence of MORB-type gabbroic and basaltic bodies associated to the Monte Nero mantle section (e.g. Montanini et al., 2008), which are absent in the Monte Gavi mantle section. The timing of Monte Nero impregnation and the presence of MORB-type rocks are consistent with the production of MORB-type melts along the Middle-Upper Jurassic ocean-continent transition. Conversely, the late Triassic impregnation of the Monte Gavi mantle section suggests melt production consequent to passive asthenospheric ascent during the onset of the rifting evolution.

Upper Triassic Lu-Hf cooling ages were obtained for the Rio Strega-Monte Prinzera sequence and were related to ductile shearing during the spinel- to plagioclase-facies transition under melt-absent conditions (Montanini et al., 2006). In addition, Upper Triassic ages were attributed to pyroxenite-forming melt production (Montanini et al., 2012; Montanini and Tribuzio, 2015).

In the framework of the other mantle bodies exposed along the Western Tethys OCT (Malenco, Platta, Totalp, Lanzo), the Upper Triassic age of Monte Gavi plagioclase-facies impregnation is a novelty. The melt production recorded by the Monte Gavi mantle sections is consistent with the Upper Triassic onset of lithosphere extension. This event was associated with formation of melts slightly enriched in Nd-Hf isotopic compositions.

3.9. Conclusions

The plagioclase-impregnated domains from the External Ligurian units include the Monte Nero and the Monte Gavi mantle bodies (see §2.6.4. The heterogeneity of the External Ligurian subcontinental mantle, Chapter 2). The plagioclase-facies melt-rock reaction recorded by the Monte Nero body was ascribed to percolation of MORB-type melts (Piccardo et al., 2004), most likely in midlle-upper Jurassic times (Rampone et al., 1995).

A petrographic and petrological description of the Monte Gavi mantle sequence is reported in Chapter 2 of this PhD Thesis (see also Ferrari et al., 2022). The geochemical and isotopic study presented in this Chapter allowed us to enhance the comprehension of the melt-rock reaction event. The main conclusions may be summarized as follows:

- In both peridotites and enclosed pyroxenite layers, the melt percolation event produced clinopyroxenes having high HREE contents and LREE-depleted chondrite-normalized patterns.
- The melt percolation event was associated with significant heating of the mantle section, as documented by temperature evaluations based on slowly diffusing elements REE and Y.

- The orthopyroxene-saturated and the slightly isotopically enriched (ε_{Nd} = +4.3) nature of the percolating melt could be related to a pyroxenite-dominated source from deep mantle levels. Alternatively, the compositional characteristics of the percolating melt originated from partial melting of a veined mantle section.
- The plagioclase-facies melt-rock reaction recorded by the Monte Gavi mantle body occurred in late Triassic times. We relate the generation of the percolating melt to an event of asthenosphere ascent associated with the early stages of the Tethyan rifting.

The late Triassic age and the geochemical characteristics of the percolating melt document melt production prior to MORB generation in the extending lithosphere. Hence, the Monte Gavi and the Monte Nero mantle bodies represent two different events of melt impregnation, with the latter most likely related to the Jurassic generation of MORB-type melts.

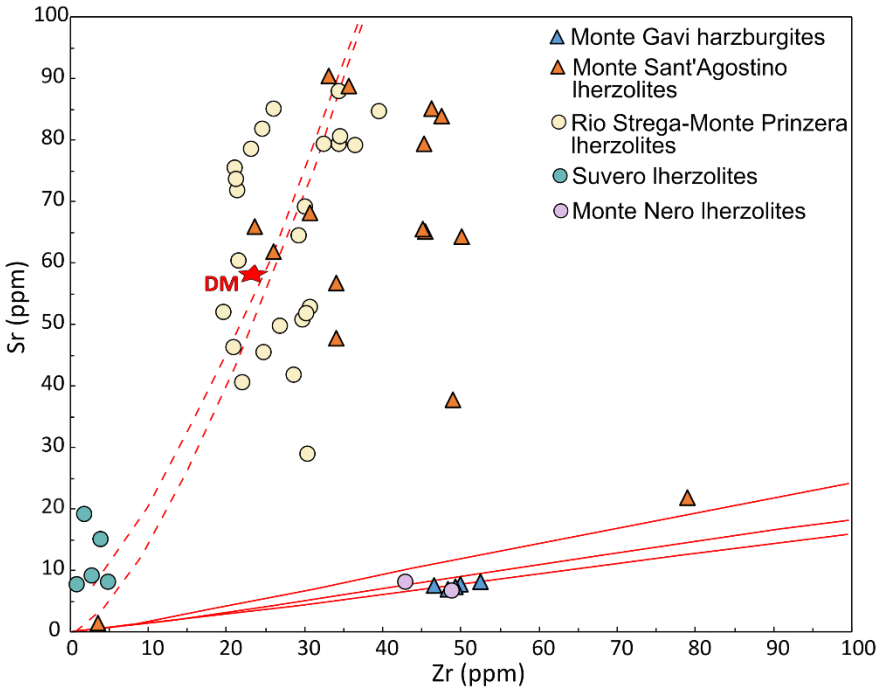

Fig. 3.13. Sr vs. Zr contents of clinopyroxenes from Monte Gavi harzburgites. Data for Monte Sant'Agostino and other External Ligurian mantle peridotites are shown for comparison. The red dashed curves represent batch melting and fractional melting trends of a spinel peridotite source and the red solid lines represent refertilization models after Müntener et al. (2010).

3.10. References

Basch V., Rampone E., Borghini G., Ferrando C., Zanetti A., 2019. Origin of pyroxenites in the oceanic mantle and their implications on the reactive percolation of depleted melts. Contributions to Mineralogy and Petrology, 174:97

Basch V., Rampone E., Crispini L., Ferrando C., Ildefonse B., Godard M., 2018. From mantle peridotites to hybrid troctolites: textural and chemical evolution during melt–rock interaction history (Mt. Maggiore, Corsica, France). Lithos, 323:4-23

Borghini G., Rampone E., Class C., Goldstein S., Cai Y., Cipriani A., Hofmann A.W., Bolge L., 2021. Enriched Hf–Nd isotopic signature of veined pyroxenite-infiltrated peridotite as a possible source for E-MORB. Chemical Geology, 586:120591

Borghini G., Rampone E., Zanetti A., Class C., Cipriani A., Hofmann A.W. and Goldstein S.L., 2013. Meter-scale Nd isotopic heterogeneity in pyroxenite-bearing Ligurian peridotites encompasses global-scale upper mantle variability. Geology, 41:1055-1058

Borghini G., Rampone E., Zanetti A., Class C., Cipriani A., Hofmann A.W. and Goldstein S.L., 2016. Pyroxenite Layers in the Northern Apennines' Upper Mantle (Italy)-Generation by Pyroxenite Melting and Melt Infiltration. Journal of Petrology, 57:625-653

Borghini G., Rampone E., Zanetti A., Class C., Fumagalli P., Godard M., 2020. Ligurian pyroxenite-peridotite sequences (Italy) and the role of melt-rock reaction in creating enriched-MORB mantle sources. Chemical Geology, 532:119252

Brey G.P. and Köhler T., 1990. Geothermobarometry in four phase lherzolites II. New thermobarometers, and practical assessment of existing thermobarometers. Journal of Petrology, 31:1353-1378

Dantas C., Gregoire M., Koester E., Conceição R.D., Rieck N., 2009. The lherzolite–websterite xenolith suite from Northern Patagonia (Argentina): evidence of mantle–melt reaction processes. Lithos, 107:107-120

Dijkstra A.H., Barth M.G., Drury M.R., Mason P.R.D., Vissers R.L.M., 2003. Diffuse porous melt flow and melt-rock reaction in the mantle lithosphere at a slow-spreading ridge: a structural petrology and LA-ICP-MS study of the Othris peridotite massif (Greece). Geochemistry Geophysics Geosystem, 4:861

Faure G., 1986. Principles of isotope geology. John Wiley and Sons, New York

Ferrara G. and Tonarini S., 1985. Radiometric geochronology in Tuscany: Results and problems. Rendiconti della Società Italiana di Mineralogia e Petrologia, 40: 111-124

Ferrari E., Montanini A., Tribuzio R., 2022. Rifting evolution of the lithospheric subcontinental mantle: New insights from the External Ligurian ophiolites (Northern Apennine, Italy). Lithos, 410-411:106571

Fumagalli P., Borghini G., Rampone E. and Poli S., 2017. Experimental calibration of Forsterite Anorthite–CaTscherm.ak–Enstatite (FACE) geobarometer for mantle peridotites. Contributions to Mineralogy and Petrology, 172:38

Griffin W.L., Pearson N.J., Belousova E., Jackson S.E., van Achterbergh E., O'Reilly S.Y., Shee S.R., 2000. The Hf isotope composition of cratonic mantle: LAM-MC-ICPMS analysis of zircon megacrysts in kimberlites. Geochimica et Cosmochimica Acta, 64:133-147

Guarnieri L., Nakamura E., Piccardo G.B., Sagaguchi C., Shimizu N., Vannucci R., Zanetti A., 2012. Petrology, trace element and SR, Nd, Hf isotope geochemistry of the North Lanzo peridotite massif (Western Alps, Italy). Journal of Petrology, 53(11):2259-2306

Hidas K., Borghini G., Tommasi A., Zanetti A. and Rampone E., 2020. Interplay between melt infiltration and deformation in the deep lithospheric mantle (External Liguride ophiolite, North Italy). Lithos, 380-381:105855

Jeffries T.E., Jackson S.E., Longerich H.P., 1998. Application of a frequency quintupled Nd:YAG source (λ=213 nm) for laser ablation inductively coupled plasma mass spectrometric analysis of minerals. Journal of Analytical Atomic Spectrometry, 13:935-940

Le Roux V., Bodinier J.-L., Alard O., O'Reilly S.Y., Griffin W.L., 2009. Isotopic decoupling during porous melt flow: A case-study in the Lherz peridotite. Earth and Planetary Science Letters, 279:76-85

Liang Y., Sun C., Yao L., 2013. A REE-in-two-pyroxene thermometer for mafic and ultramafic rocks. Geochimica et Cosmochimica Acta, 102:246-260

Marroni M., Meneghini F. and Pandolfi L., 2017. A revised subduction inception model to explain the Late Cretaceous, double-vergent orogen in the precollisional western Tethys: Evidence from the Northern Apennines. Tectonics, 36:2227-2249

Meli S., Montanini A., Thoni M. and Frank W., 1996. Age of mafic granulite blocks from the external Liguride units (Northern Apennines, Italy). Memorie di Scienze Geologica, 48: 65-72

Montanini A. and Tribuzio R., 2015. Evolution of recycled crust within the mantle: Constraints from the garnet pyroxenites of the External Ligurian ophiolites (northern Apennines, Italy). Geology, 43:911-914

Montanini A., Tribuzio R. and Anczkiewicz R., 2006. Exhumation History of a Garnet Pyroxenite-bearing Mantle Section from a Continent-Ocean Transition (Northern Apennine Ophiolites, Italy). Journal of Petrology, 47:1943-1971

Montanini A., Tribuzio R. and Thirlwall M., 2012. Garnet clinopyroxenite layers from the mantle sequences of the Northern Apennine ophiolites (Italy): Evidence for recycling of crustal material. Earth and Planetary Science Letters, 351-352:171-181

Montanini A., Tribuzio R. and Vernia L., 2008. Petrogenesis of basalts and gabbros transition (external Liguride from an ancient continent-ocean ophiolites, northern Italy). Lithos, 101:453-479

Müntener O., Manatschal G., Desmurs L., Pettke T., 2010. Plagioclase Peridotites in Ocean-Continent Transitions: Refertilized Mantle Domains Generated by Melt Stagnation in the Shallow Mantle Lithosphere. Journal of Petrology, 51:255-294

Müntener O., Pettke T., Desmurs L., Meier M. and Schaltegger U., 2004. Refertilization of mantle peridotite in embryonic ocean basins: trace element and Nd isotopic evidence and implications for crust-mantle relationships. Earth and Planetary Science Letters, 221:293-308.

Piccardo G.B., Müntener O., Zanetti A. and Pettke T., 2004. Ophiolitic Peridotites of the Alpine-Apennine System: Mantle Processes and Geodynamic Relevance. International Geology Reviews, 46(12):1119-1159

Piccardo G.B., Padovano M., Guarnieri L., 2014. The Ligurian Tethys: Mantle processes and geodynamics. Earth-Science Reviews, 138:409-434

Rampone E., Borghini G., Basch V., 2020. Melt migration and melt-rock reaction in the Alpine-Apennine peridotites: Insights on mantle dynamics in extending lithosphere. Geoscience Frontiers, 11:151-166

Rampone E., Hofmann A.W., 2012. A global overview of isotopic heterogeneities in the oceanic mantle. Lithos, 148:247-261

Rampone E., Hofmann A.W., Piccardo G.B., Vannucci R., Bottazzi P. and Ottolini L., 1995. Petrology, Mineral and Isotope Geochemistry of the External Liguride Peridotites (Northern Apennines, Italy). Journal of Petrology, 36:81-105

Sanfilippo A. and Tribuzio R., 2011. Melt transport and deformation history in a nonvolcanic ophiolitic section, northern Apennines, Italy: Implications for crustal accretion at slow spreading settings. Geochemistry Geophysics Geosytems, 12(7)

Snow J.E., Schmidt G. and Rampone E., 2000. Os isotopes and highly siderophile elements (HSE) in the Ligurian ophiolites, Italy. Earth and Planetary Science Letters, 175:119-132

Stracke A., 2012. Earth's heterogeneous mantle: A product of convection-driven interaction between crust and mantle. Chemical Geology, 330-331:274-299

Stracke A., Genske F., Berndt J., Koornneef J.M., 2019. Ubiquitous ultra-depleted domains in Earth's mantle. Nature Geoscience, 12(10):851-855

Stracke A., Snow J.E., Hellebrand E., von der Handt A., Bourdon B., Birbaum K., Günther D., 2011. Abyssal peridotite Hf isotopes identify extreme mantle depletion. Earth and Planetary Science Letters, 308:359-368

Sun C., Liang Y., 2017. A REE-in-plagioclase-clinopyroxene thermometer for crustal rocks. Contributions to Mineralogy and Petrology, 172:24

Sun S.-s, McDonough W.F., 1989. Chemical and isotopic systematics of oceanic basalts: implications for mantle composition and processes. Geological Society Special Publications, 42:313-345

Tribuzio R., Garzetti F., Corfu F., Tiepolo M. and Renna M.R., 2016. U-Pb zircon geochronology of the Ligurian ophiolites (Northern Apennine, Italy): Implications for continental breakup to slow seafloor spreading. Tectonophysics, 666:220-243

Tribuzio R., Renna M.R., Dallai L. and Zanetti A., 2014. The magmatic-hydrothermal transition in the lower oceanic crust: Clues from the Ligurian ophiolites, Italy. Geochimica Cosmochimica Acta, 130:188-211

Tribuzio R., Thirlwall M. and Vannucci R., 2004. Origin of the Gabbro---Peridotite Association from the Northern Apennine Ophiolites (Italy). Journal of Petrology, 45:1109-1124

Villa I.M., Hermann J., Müntener O. and Trommsdorff V., 2000. 39Ar−40Ar dating of multiply zoned amphibole generations (Malenco, Italian Alps). Contributions to Mineralogy and Petrology, 140: 363-381

3.11. Tables

Table 3.1. Bulk rock major and trace element compositions of Monte Gavi pyroxenites. Major element compositions are calculated on anhydrous basis and normalized to 100. Major elements are expressed in wt%, trace elements in ppm.

Sample	GAV2	GA1	GA1 Pl rich fraction	GA1 Cpx rich fraction	MG6	MG5	IC2-3
Description	Type Ia pyroxenite	Type Ib pyroxenite	Type Ib pyroxenite	Type Ib pyroxenite	Type Ib pyroxenite	Type II pyroxenite	Type II pyroxenite
SiO_2	41.77	46.95	45.29	50.23	47.30	40.84	46.11
TiO_2	0.25	0.42	0.14	0.82	0.48	0.38	0.37
Al_2O_3	14.02	14.44	20.66	11.04	14.06	12.27	7.09
FeO	6.92	8.58	7.03	7.09	8.84	7.49	7.77
MnO	0.14	0.16	0.12	0.20	0.17	0.16	0.13
MgO	24.17	20.04	15.74	18.73	19.02	32.82	30.10
CaO	12.50	6.99	7.82	10.06	7.47	5.92	8.21
Na_2O	0.15	0.54	0.82	0.63	0.49	0.10	0.19
K_2O	0.09	1.88	2.37	1.20	2.18	0.01	0.02
P_2O_5	bdl	bdl	bdl	bdl	bdl	0.01	bdl
LOI	8.46	4.12	4.2	2.18	4.04	11.11	7.03
Mg#	86	81	80	82	79	89	87
SiO_2/MgO	1.73	2.34	2.88	2.68	2.49	1.24	1.53
V	115	155	76	273	198	155	129
Cr	2570	790	890	650	620	3300	2400
Ni	900	560	620	260	530	990	1420
Co	53	54	56	35	52	55	69
Sc	17	36	6.00	71	39	35	22
Sr	15	84	118	61	92	9.00	16
Y	4.90	14	1.20	35	16	9.80	8.40
Nb	bdl	bdl	bdl	bdl	bdl	bdl	bdl
Zr	10	20.00	3.00	59.00	21.00	15.00	17.00
La	0.37	0.23	bdl	0.19	0.47	0.22	0.33

Ce	1.40	0.93	0.66	1.37	1.31	0.99	1.46
Pr	0.22	0.20	0.12	0.37	0.26	0.18	0.29
Nd	1.26	1.54	0.76	3.51	1.88	1.12	1.81
Sm	0.48	1.03	0.22	2.45	1.22	0.51	0.66
Eu	0.23	0.46	0.39	0.74	0.49	0.26	0.29
Gd	0.74	1.79	0.27	4.56	2.14	1.00	1.11
Tb	0.13	0.39	0.04	0.93	0.42	0.22	0.22
Dy	0.92	2.50	0.22	6.28	2.90	1.57	1.45
Ho	0.19	0.53	0.04	1.29	0.60	0.37	0.31
Er	0.52	1.48	0.11	3.56	1.76	1.10	0.91
Tm	0.08	0.22	0.02	0.51	0.24	0.18	0.14
Yb	0.56	1.39	0.11	3.08	1.69	1.17	1.02
Lu	0.09	0.21	0.02	0.48	0.26	0.18	0.16
Hf	0.30	0.70	bdl	1.50	0.70	0.40	0.50
Ta	bdl	bdl	0.13	0.01	bdl	bdl	bdl
Th	bdl	bdl	bdl	bdl	bdl	bdl	bdl
U	bdl	bdl	bdl	0.01	0.09	bdl	bdl

LOI = Loss On Ignition

Mg# = [100 × Mg/(Mg+Fe_{tot})]

bdl = below detection limits

Table 3.2. Representative trace element compositions (ppm) of minerals from Monte Gavi selected samples.

Sample	MGA7		GAV2		GA1				MG6				MG5
Rock type	Harzburgite		Type-Ia pyroxenite		Type-Ib pyroxenite				Type-Ib pyroxenite				Type-II pyroxenite
Mineral	Opx	Cpx	Cpx (core)	Cpx (rim)	Cpx (core)	Cpx (int)	Cpx (rim)	Pl	Cpx (core)	Cpx (rim)	Opx	Pl	Cpx (core)
Sc	28	64	40	45	148	138	220	1.58	154	199	69	3.34	199
Ti	1100	4400	3871	3499	11197	11343	10945	345	10499	9850	3556	553	10233
V	137	312	259	247	543	493	687	2.21	750	867	402	23	491
Cr	3570	6064	2279	2586	757	726	952	bdl	673	1048	628	24	3605
Co	51	22	26	24	24	24	22	0.08	24	23	63	0.80	17
Ni	bdl	bdl	275	274.57	190	198.61	169	0.67	189	166	348	3.84	265
Rb	bdl	bdl	0.08	0.08	0.03	bdl	bdl	0.06	0.05	0.05	0.06	0.09	0.09
Sr	0.06	7.61	8.20	7.34	1.53	1.20	1.06	25	1.88	1.89	0.38	40	2.72
Y	2.77	31	16	15	123	128	126	1.10	84	90	7.91	1.75	104
Zr	4.36	49	29	27	189	191	221	bdl	126	142	10	1.33	178
Nb	bdl	bdl	0.25	0.16	0.04	0.02	bdl	bdl	0.03	0.02	bdl	bdl	0.02
Ba	bdl	bdl	0.51	1.00	0.11	0.07	0.04	0.16	0.10	0.05	0.18	0.27	0.22
La	bdl	0.47	0.69	0.50	0.26	0.25	0.18	0.24	0.24	0.20	0.01	0.15	0.48
Ce	0.03	3.34	3.72	3.15	2.69	2.65	2.39	0.96	2.57	2.23	0.02	0.90	3.91
Pr	0.01	0.87	0.76	0.65	1.00	1.17	0.97	0.18	0.93	0.89	0.01	0.19	1.23
Nd	0.10	6.36	4.77	3.95	11	11	11	0.96	9.19	9.32	0.12	1.26	11
Sm	0.07	2.90	1.75	1.53	9.23	9.04	8.76	0.23	6.13	6.31	0.14	0.38	7.42
Eu	0.04	1.11	0.79	0.67	2.29	2.23	2.02	0.62	1.73	1.80	0.03	0.60	1.72
Gd	0.20	4.19	2.49	2.42	16	17	17	0.29	11	12	0.42	0.33	13
Tb	0.05	0.77	0.47	0.42	3.47	3.40	3.54	0.05	2.33	2.46	0.11	0.06	2.79
Dy	0.39	5.42	3.00	2.87	23	24	26	0.22	15	17	1.03	0.26	20
Ho	0.09	1.12	0.61	0.57	4.95	5.10	5.00	0.04	3.30	3.46	0.27	0.08	4.54
Er	0.34	3.17	1.66	1.59	13	13	13	0.09	8.56	9.23	1.14	0.16	12
Tm	0.06	0.45	0.24	0.23	1.74	1.78	1.72	bdl	1.21	1.26	0.18	0.04	1.62
Yb	0.55	2.75	1.67	1.47	11	11	11	bdl	7.99	8.18	1.82	bdl	10

Lu	0.09	0.38	0.25	0.22	1.39	1.50	1.43	bdl	1.08	1.06	0.34	0.04	1.37
Hf	0.13	1.38	0.91	0.79	5.26	3.80	7.91	bdl	4.51	6.54	0.469	bdl	6.72
Ta	bdl	bdl	0.05	0.11	0.04	0.01	bdl	0.06	0.03	0.05	0.11	0.21	0.02
Pb	bdl	bdl	0.04	bdl	0.03	bdl	0.03	bdl	0.04	0.03	0.03	bdl	0.07
Th	bdl	bdl	0.03	bdl	0.01	bdl	bdl	bdl	0.01	0.02	bdl	bdl	0.02
U	bdl	bdl	0.01	0.02	0.02	bdl	bdl	0.02	0.01	bdl	bdl	bdl	0.01
La_N/Sm_N	-	0.10	0.25	0.21	0.02	0.02	0.01	0.69	0.03	0.02	0.04	0.26	0.04
Gd_N/Yb_N	0.31	1.26	1.23	1.36	1.20	1.24	1.27	-	1.11	1.18	0.19	-	1.02
Eu/Eu*	1.00	0.97	1.15	1.06	0.57	0.55	0.51	7.29	0.65	0.64	0.43	5.12	0.54

bdl = below detection limits

Table 3.3. Representative trace element compositions (ppm) of minerals from Monte Sant'Agostino selected samples.

Sample	MGO1				IC8-1			IC8-3		AM489				
Rock type	Mylonitic lherzolite				Mylonitic lherzolite			Mylonitic lherzolite		Spl websterite				
Mineral	Opx (core)	Opx (rim)	Cpx (core)	Cpx (rim)	Opx (core)	Cpx (core)	Cpx (rim)	Opx (core)	Cpx (core)	Opx (core)	Cpx1 (core)	Cpx1 (rim)	Cpx2 (core)	Cpx2 (rim)
Sc	19	20	65	65	21	91	71	15	55	35	81	89	99	123
Ti	952	836	3689	4021	815	5872	4057	835	4187	728	3181	3425	3252	3468
V	102	99	254	254	101	366	283	93	293	161	341	348	273	280
Cr	2468	2138	5246	5040	1780	5599	5308	2261	4253	1136	1869	1492	1356	1188
Co	bdl	bdl	bdl	bdl	56	106	24	55	22.99	49	18	15	15	16
Ni	bdl	bdl	bdl	bdl	670	1978	371	677	356	396	169	136	179	180
Rb	bdl	bdl	bdl	bdl	0.18	0.22	0.06	0.07	0.05	0.23	0.18	0.08	bdl	0.08
Sr	0.22	0.10	60	66	0.67	67	77	0.47	69.57	0.50	5.25	3.95	6.42	6.00
Y	1.24	1.19	18	19	1.29	28	22	1.05	18.61	2.23	29	32	42	43
Zr	1.78	1.57	30	32	2.21	54	48	1.83	41.65	2.49	30	35	37	40
Nb	0.01	0.01	0.15	0.10	0.02	0.38	0.05	0.01	0.12	0.01	0.40	0.35	0.32	0.34
Ba	0.004	0.01	0.01	0.005	0.14	0.56	3.92	0.02	0.04	1.01	0.40	0.54	0.28	0.58
La	0.002	0.001	0.87	0.90	0.03	1.68	1.74	0.01	1.50	0.03	0.58	0.42	0.63	0.70
Ce	0.01	0.01	3.15	3.20	0.04	5.71	5.20	0.03	5.34	0.03	2.96	2.85	3.64	3.44
Pr	0.003	0.002	0.62	0.62	0.02	1.11	0.90	0.01	0.94	0.01	0.67	0.68	0.72	0.72
Nd	0.02	0.02	3.87	3.98	0.10	6.17	5.58	0.05	5.73	0.09	4.65	4.82	4.93	4.82
Sm	0.02	0.02	1.60	1.59	bdl	2.56	2.05	0.03	2.09	bdl	2.20	2.10	2.19	2.21
Eu	0.01	0.01	0.65	0.66	bdl	1.06	0.84	0.01	0.93	0.03	0.88	0.90	0.63	0.74
Gd	0.05	0.04	2.27	2.43	0.08	3.43	3.00	0.07	2.74	0.11	3.28	3.29	3.49	3.24
Tb	0.01	0.01	0.44	0.46	0.02	0.76	0.55	0.01	0.52	0.03	0.64	0.67	0.78	0.85
Dy	0.15	0.14	3.19	3.44	0.14	4.70	3.80	0.09	3.41	0.23	4.60	4.72	7.25	7.17
Ho	0.04	0.04	0.68	0.72	0.04	1.12	0.79	0.04	0.72	0.07	1.07	1.19	1.72	1.69
Er	0.18	0.18	2.04	2.08	0.19	3.36	2.41	0.15	2.00	0.36	3.19	3.68	4.97	5.02
Tm	0.04	0.04	0.28	0.32	0.04	0.43	0.34	0.03	0.27	0.07	0.50	0.56	0.76	0.79
Yb	0.29	0.33	1.91	2.14	0.39	3.08	2.25	0.24	2.08	0.58	3.51	3.86	5.60	5.47

Lu	0.05	0.06	0.27	0.29	0.09	0.45	0.39	0.04	0.29	0.12	0.52	0.55	0.82	0.79
Hf	0.06	0.05	0.89	1.00	0.10	1.61	1.24	0.08	1.21	0.10	0.69	0.92	0.91	1.27
Ta	0.02	0.01	0.02	0.02	0.02	0.09	0.04	0.01	0.03	0.02	0.04	0.02	0.05	0.03
Pb	0.09	0.08	0.05	0.05	bdl	0.08	bdl	0.01	0.06	0.55	0.23	0.22	0.15	0.26
Th	0.0002	0.0004	0.03	0.02	0.02	0.06	bdl	0.01	0.03	0.01	0.03	0.06	0.05	0.11
U	0.0003	0.0003	0.01	0.005	0.02	0.03	bdl	0.01	0.03	0.02	0.04	0.03	0.03	0.04
La_N/Sm_N	0.06	0.05	0.35	0.36	-	0.42	0.55	0.21	0.46	-	0.17	0.13	0.19	0.21
Gd_N/Yb_N	0.14	0.11	0.98	0.94	0.17	0.92	1.10	0.25	1.09	0.15	0.77	0.70	0.52	0.49
Eu/Eu*	0.83	0.92	1.04	1.03	-	1.09	1.03	0.94	1.19	-	1.00	1.05	0.69	0.85

bdl = below detection limits

Table 3.4. Geothermometric estimates based on slowly diffusing elements (REE,Y) for the Monte Gavi mantle section. Conventional thermometric estimates are also reported. Temperature estimates for the Monte Sant'Agostino mantle section are reported for comparative purposes. Temperature values are given in °C.

	$T_{Cpx\text{-}Opx}$[a]	$T_{Cpx\text{-}Pl}$[b]	$T_{Ca\text{-}in\text{-}Opx}$[c,(1)]	T_{2Px}[c,(1)]
Monte Gavi				
Harzburgite MGA7	1245 ± 90[(1)]		994	931
Type-Ib pyroxenite MG6	1278 ± 32[(2)]	1257 ± 48[(2)]	1004	976
Type-Ib pyroxenite GA1		1170 ± 14[(2)]		
Monte S. Agostino				
Mylonitic lherzolite MGO1	1057 ± 31[(1)]		988	914
Mylonitic lherzolite IC8-1	1042 ± 34[(1)]		918	857
Mylonitic lherzolite IC8-3	990 ± 70[(1)]		974	981
Spl-Pl websterite AM489	1103 ± 78[(1)]		918	936

[a] = Liang et al. (2013)

[b] = Sun and Liang (2017)

[c] = Brey and Köhler (1990)

Assumed P : [(1)] 1.5 GPa, [(2)] 0.7 GPa

Table 3.5. Nd and Hf isotopic data for Monte Gavi selected pyroxenite samples. Data were obtained on whole rock powders (WR) and clinopyroxene separates (Cpx)

Sample	Sm (ppm)	Nd (ppm)	$^{147}Sm/^{144}Nd$	$^{143}Nd/^{144}Nd$	± 2s	$\varepsilon_{Nd(0)}$	$\varepsilon_{Nd(210)}$	Lu (ppm)	Hf (ppm)	$^{176}Lu/^{177}Hf$	$^{176}Hf/^{177}Hf$	± 2s	$\varepsilon_{Hf(0)}$	$\varepsilon_{Hf(210)}$
Type-Ia pyroxenite														
GAV2 WR	0.49*	1.08*	0.27	0.513148	0.000008	9.95	7.88							
GAV2 Cpx	1.70	4.58	0.22	0.513133	0.000008	9.66	8.93	0.24	0.88	0.04	0.283339	0.000053	20.04	19.25
Type-Ib pyroxenite														
GA1 WR	0.92*	1.42*	0.39	0.513114	0.000008	9.29	4.08							
GA1 Px-Rich Fraction WR	2.49*	3.47*	0.43	0.513149	0.000008	9.97	3.63							
GA1 Pl-Rich Fraction WR	0.23*	0.73*	0.19	0.512816	0.000012	3.47	3.65							
MG6 WR	1.22	1.88	0.39	0.513101	0.000010	9.03	3.81							
GA1 Cpx	9.10	11	0.50	0.513252	0.000010	11.98	3.97	1.42	5.50	0.04	0.282934	0.000034	5.73	5.29
MG6 Cpx	6.17	9.22	0.40	0.513135	0.000008	9.69	4.14	1.08	5.02	0.03	0.283008	0.000055	8.35	8.80
Type-II pyroxenite														
IC2/3 WR	0.66*	1.81*	0.22	0.512896	0.000010	5.03	4.41							
MG5 Cpx	7.58	11	0.43	0.513166	0.000008	10.30	4.18	1.38	6.52	0.03	0.282983	0.000042	7.48	7.99

*Concentrations calculated using Isotope Dilution data

Chapter 4
Ouassé (New Caledonia) pyroxenites witness mantle heterogeneity in young subduction systems

4.1. Introduction

The New Caledonia ophiolite is mainly constituted by mantle harzburgites which recorded evolution in a forearc setting during a Late Paleocene subduction event. Pre-obduction granitoid to gabbroic dikes locally crosscut the harzburgites and attest the presence of subduction-related melts that percolated the forearc mantle. Consistently, these dikes gave U-Pb zircon ages of ~55-50 Ma (e.g., Cluzel, 2020). Pyroxenitic dikes occur more rarely in the forearc section and are poorly described in the literature.

The Ouassé mantle section is located in the Bogota Peninsula, in the central-eastern part of the New Caledonia island. Here, the harzburgites are deformed as a consequence of the activity of the Bogota Peninsula Shear Zone (BPSZ). Pyroxenitic dikes usually cut the peridotite foliation at variable angles, but concordant layers are also present. Some of these pyroxenites were the subject of a recent petrological investigation (Xu et al., 2021a). However, this paper studies a limited set of samples, without providing geochronological constraints. A thorough structural study of pyroxenitic dikes in the Bogota Peninsula Shear Zone was made by Titus et al. (2011).

The present PhD Thesis describes a wide variety of pyroxenitic samples from the Ouassé mantle sequence. A complete petrological characterization includes major and trace elements compositions of whole rocks and mineral phases. The main aim of this study is to elucidate the nature and origin of the pyroxenite-forming melts. In addition, $^{40}Ar/^{39}Ar$ amphibole dating have been provided in order to put constraints on the relative age of pyroxenite emplacement and peridotite deformation. Overall, the results will be discussed in terms of melt production and percolation in the forearc mantle during the early stages of subduction initiation. In a broader perspective, the Thesis wishes to add new interpretations about the Bogota Shear Zone activity.

4.2. Geological and petrological setting

The New Caledonia island is located in the south-west Pacific Ocean. Geological terranes cover a wide range of lithologies, as a result of a complex tectonic history (see Cluzel et al., 2012b). In the Permian-Early Cretaceous period, during the subduction phase along the south-east Gondwanaland margin, New Caledonia was involved in a forearc region. A Late Cretaceous rifting phase caused separation of New Caledonia from Australia, thus creating the Norfolk Ridge (also referred to New Caledonia Ridge). In the Late Paleocene, a NE-dipping intra-oceanic subduction took place in the nearby Loyalty Basin, likely close to an active spreading ridge (Ulrich et al., 2010; Cluzel et al., 2012a). The Norfolk Ridge entered obliquely the subduction zone (Cluzel et al., 2021), triggering a Late Eocene obduction. Consequently, terranes of the Loyalty Basin (Poya Terrane and Peridotite Nappe) were overthrust onto the New Caledonia Ridge. Late Oligocene post-obduction plutonism and Early Miocene island uplift represent the latest major events.

The Peridotite Nappe terrane occupies almost half of the New Caledonia island (Fig. 4.1) and represents the oceanic lithosphere of the Loyalty Basin. The Peridotite Nappe is underlain by a highly-sheared serpentinite sole testifying obduction tectonics. The Peridotite Nappe is mainly composed of mantle harzburgites recording an evolution in a forearc environment. They outcrop extensively in the southern portion of the island (Massif du Sud). Minor mantle lherzolites (Cpx 5-15 vol%) are found in the northern sector (Ulrich et al., 2010; Secchiari et al., 2016). They represent slightly depleted abyssal-type peridotites recording moderate partial melting degrees (8-9%). Three regional-scale high-temperature shear zones representing oceanic paleotransform faults were detected in the Peridotite Nappe: the Bogota Peninsula Shear Zone (BPSZ; Prinzhofer and Nicolas, 1980; Titus et al., 2011; Chatzaras et al., 2020) and the Humboldt Corridor (Ferré et al., 2004; Vogt and Podvin, 1983), which developed in the harzburgites, and the Bélep Shear Zone (Nicolas, 1989; Titus et al., 2011) which developed in the lherzolites.

The mantle sequence is locally associated with mafic and ultramafic cumulates regarded as the lower crust of a nascent arc (Secchiari et al., 2018 and references therein). By contrast, the upper oceanic crust is missing in the ophiolite, probably because of erosion or tectonic detachment before, during and/or after obduction (Cluzel et al., 2001). A witness of the Loyalty Basin oceanic crust can be found in the allochtonous Poya Terrane. Here, basaltic rocks have variable compositions (Enriched-MORB to Back-Arc Basin Basalts) and their relationships with the Peridotite Nappe ultramafic rocks is still debated (Eissen et al., 1998; Ulrich et al., 2010; Secchiari et al., 2016).

The harzburgites are ultra-depleted peridotites lacking primary clinopyroxene which recorded a two-stage melting process: an anhydrous melting in a marginal basin (15% degree of fractional melting of a depleted mantle MORB source) and a subsequent fluid-assisted melting in a forearc environment (up to 18% degree of fractional melting). Contamination by subduction-related melts

and fluids led to Fluid Mobile Elements (FME), Nb, Zr and Hf enrichments, coupled to enriched Nd and Pb isotopic compositions (see Secchiari et al., 2020).

Before the obduction, the Peridotite Nappe mantle sequence was intruded by:

- Decimetre- to decametre-thick dikes exposed in the Massif du Sud. They range in composition from granitoid to gabbroic and show boninite-like and depleted to ultra-depleted Island Arc-Tholeiites (IAT) geochemical signatures. Zircon and titanite U-Pb dating gave a weighted average age of 52.8 ± 0.2 Ma for the felsic dikes (Cluzel et al., 2006) and a U-Pb zircon age of 53.7 ± 0.7 Ma was obtained for the boninite-series dikes (Cluzel et al., 2016)
- Tremolite-antigorite veins originated from slab-derived fluids (Cluzel et al., 2020)
- Meter-thick lenses of boninite rocks within the Peridotite Nappe serpentinite sole. They are genetically linked to the pre-obduction boninite-like dikes and derive from low degree partial melting of a peridotite previously re-enriched by small amount of melt originated from the subducted slab. Two boninite samples yielded $^{40}Ar/^{39}Ar$ plateau ages of 47.4 ± 0.9 Ma and 50.4 ± 1.3 Ma (Cluzel et al., 2016)
- Gabbro and diorite dikes and lenses (serpentinized peridotites of the Kopeto massif, Xu et al., 2021b). Gabbros were interpreted to crystallize from basaltic magmas from a DMM source contaminated by subduction-related fluids, whereas diorites derived from hydrous melting of mafic rocks. Both types of dikes gave U-Pb zircon and titanite ages of ~ 55-53 Ma
- Websteritic dikes crosscutting mylonitic harzburgites in the BPSZ. Boninitic melts are thought to have formed these intrusions, causing a metasomatic imprint in the host peridotites, e.g. LREE enrichment in orthopyroxene (Xu et al., 2021a)

As a whole, these dikes are related to melts and/or fluids percolating the forearc mantle during the Eocene subduction. Ages mainly cluster at ~ 54 Ma, in agreement with subduction inception constrained at 56 Ma ($^{40}Ar/^{39}Ar$ amphibole dating; Cluzel et al., 2012a). Slab-derived fluids also affected pre-existing mantle intrusions, as reported by Soret et al. (2016) for mafic dikes being amphibolitized during the initial stage of Eocene subduction at ~ 55 Ma ($^{40}Ar/^{39}Ar$ amphibole dating).

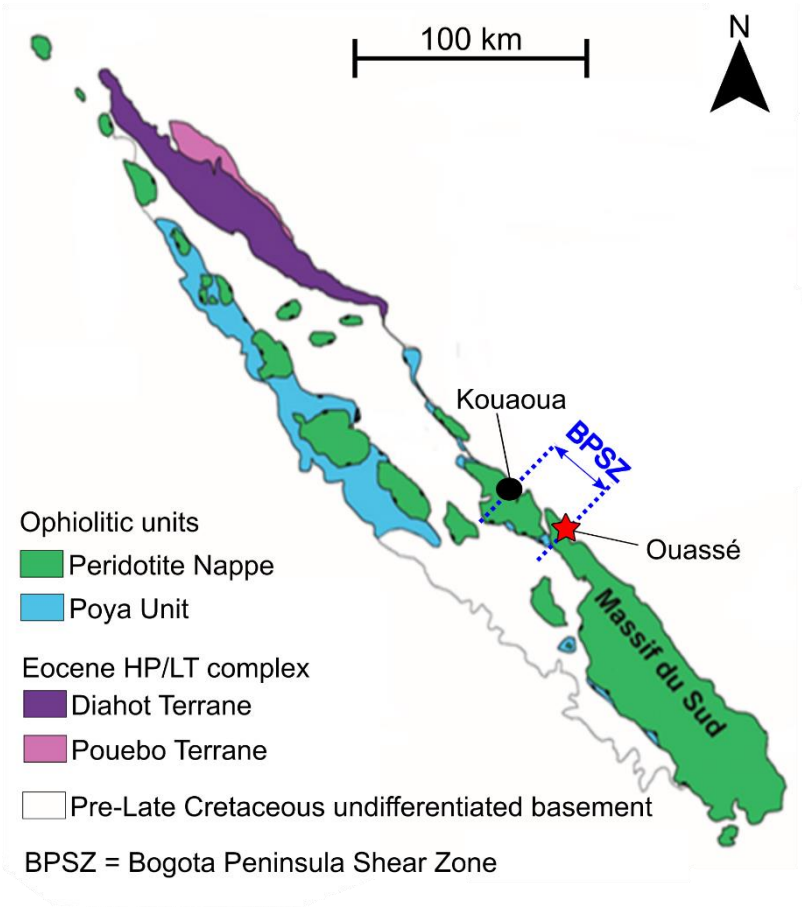

Fig. 4.1. New Caledonia sketch map (modified after Secchiari et al., 2020) showing the Peridotite Nappe extent. The sampling locality (Ouassé) is marked by a red star. The dotted blue lines indicate the lateral extension of the Bogota Peninsula Shear Zone. According to Chatzaras et al. (2020), two mylonite zones are located near Ouassé and Kouaoua.

4.3. Field relationships and sampling

Samples were collected in the Ouassé Bay, in the Bogota Peninsula shear zone (Fig. 4.1). The Bogota Peninsula is located in the central-eastern part of the New Caledonia island and represents the north-western extension of the Massif du Sud.

The Bogota Peninsula Shear Zone (BPSZ) is a 25-km-wide region of mantle harzburgites characterized by a strain gradient increasing towards two distinct 1 to 3 km-wide mylonitic zones (located in Ouassé and east of Kouaoua, respectively). Localization of deformation is marked by coarse granular textures ranging from protomylonite to mylonite, olivine grain size reduction, increasingly stretched orthopyroxene grains (aspect ratio up to 25:1) and presence of olivine-rich bands concordant to the foliation (Titus et al., 2011; Chatzaras et al., 2020). Strain increase also influenced fabric orientation, rotating strike foliation from NW-SE to NNE-SSW and steepening it from ~ 60° to ~ 90°. For comparison, the average foliation of the undeformed portion of the Massif du Sud body is ~ 20° E-W to NW-SE (Titus et al., 2011). Dextral sense of motion was attributed to the BPSZ and mylonite zones were regarded as the mantle areas corresponding to single faults in a transform system (Prinzhofer and Nicolas, 1980; Titus et al., 2011). Chatzaras et al. (2020) identified microdeformation zones (MDZs) in all deformed harzburgites. MDZs are μm- to mm-wide and are made by recrystallized olivine or orthopyroxene locally dislocating grains of the primary mineral assemblage. MDZs were interpreted to record stress change through time, from seismic-related brittle deformation to ductile deformation and dynamic recrystallization. Interstitial pargasite modally increasing towards the mylonite zones suggests high-temperature fluids percolating the shear zone, likely favouring strain localization and mylonitization. Serpentinite shear zones concordant with the high-temperature foliation would indicate ocean water infiltration during cooling of the shear zone (Teyssier et al., 2016).

Prinzhofer and Nicolas (1980) first reported the existence of several dikes in the BPSZ. Based on crosscutting relationships, the sequence of intrusion is (i) pyroxenite, (ii) feldspathic pyroxenite, (iii) hornblende gabbro, (iv) plagiogranite and (v) diabase, from the oldest to the youngest. A careful structural study of pyroxenite and diabase dikes was made by Titus et al. (2011). Some pyroxenitic bodies show constant thicknesses while others are necked or boudinaged. Locally, there are also folded layers. Pyroxenite foliation rotated and steepened with increasing strain, i.e. going towards the mylonite zone, and the dikes underwent greater stretching. Ultra-elongated boudins were locally dismembered leaving relict orthopyroxene blebs. Diabase dikes are mainly found in the mylonite zone. Due to their undeformed nature, they were considered as the last magmatic event.

In the Ouassé Bay, porphyroclastic to mylonitic harzburgites cut by pyroxenitic dikes crop out. Up to 1 cm-sized aligned and/or stretched orthopyroxene grains define the peridotite foliation. Tiny black spinel is also visible (Fig. 4.2a-b). Pyroxenites occur as 5-15 cm thick layers, mostly intersecting at high angle the harzburgite foliation and showing sharp contacts (Fig. 4.2c-d). Discordant low angle (Fig. 4.2e) and rare concordant (Fig. 4.2f), locally boudinaged, layers occur too. Our sampling focused on pyroxenites and the host harzburgites. Here, we report data for three websterites (two discordant high angle: OU1 and OU4; one discordant low angle: OU7B), two orthopyroxenites (one concordant: OU5A; one discordant high angle: OU8) and three harzburgites.

4.4. Methodology

Major element compositions of minerals were analysed using a JEOL-6400 electron microprobe equipped with a LINK-ISIS energy dispersive microanalytical system at the Department of Chemistry, Life Sciences and Environmental Sustainability of Parma University. The electron beam was produced at an accelerating voltage of 15 kV and probe current of 0.25 nA. Both natural minerals and synthetic compounds were used as standards.

Whole rock powders were prepared to analyse major and trace element compositions. Before making the powders, alteration was carefully removed from each rock sample using the diamond saw. Then, each rock sample was ground with a mortar until reaching a size less than 2 mm. The obtained granulate was reduced to powder (grain size < 2 μm) using an agate mill. The mortar, the sieves and the agate mill were cleaned with water and alcohol between one sample and another to avoid any contamination. Whole rock major and trace elements were analysed at Activation Laboratories (Ancaster, Ontario, Canada) by inductively coupled plasma (ICP) optical emission spectroscopy and ICP mass spectrometry. Precision and accuracy are estimated to be better than 2% for SiO_2, Al_2O_3, Fe_2O_3 and MgO and better than 5% for the other major elements. Precision and accuracy of trace element analyses are assessed to be within 10%.

In situ trace element analyses of mineral phases were carried out using laser ablation ICP mass spectrometry at Istituto di Geoscienze e Georisorse - C.N.R., Unità di Pavia. The laser probe consisted of a Q-switched Nd:YAG laser, model Quantel (Brilliant), whose fundamental emission in the near-IR region (1064 nm) was converted into 266 nm wavelength using three harmonic generators (Jeffries et al., 1998). Spot diameter was typically ~50 μm. The ablated material was analysed by using an Elan DRC-e quadrupole mass spectrometer. Helium was utilized as carrier gas and mixed with Ar downstream of the ablation cell. NIST 612 was used as external standard. The CaO content determined by electron microprobe was utilized as internal standard, scaled on the $^{44}Ca+$ signal. Precision and accuracy were assessed from repeated analyses of the BCR2 standard and resulted

better than 10% at ppm concentration level. Detection limits were typically in the range of 1.0-0.5 ppm for Cr and Ti, 0.5-0.1 ppm for Sc, 100-10 ppb for Sr, Zr, Ba, Rb, V and Gd, 10-1 ppb for Y, Nb, REE, Hf and Ta.

Amphibole separates from two distinct amphibole-bearing websterites (OU1 and OU7B) were obtained in order to get $^{40}Ar/^{39}Ar$ data. After grinding and sieving of rock samples, amphiboles were separated from the 250/180 µm granulate fractions by handpicking.

The $^{40}Ar/^{39}Ar$ analytical data are organized to comply with FAIR data reporting norms (see for instance Schaen et al., 2020). Each amphibole separate was irradiated at the Oregon State University for 14 hours in the CLICT position. Fish Canyon sanidine was used as the neutron flux monitor and has an assigned an age of 28.201 Ma (Kuiper et al., 2008) using a ^{40}K decay constant of $5.463e^{-10}/a$ (Min et al., 2000).

After irradiation, the sample was step-heated with a diode laser with a heating time of 45 seconds per step followed by 45 seconds of gas clean up with a SAES GP-50 getter operated at 2 A. Gas was also exposed to a cold finger operated at ~-140°C. Argon isotopes were measured using a Thermo-Fisher Scientific Helix MC-plus multi-collector mass spectrometer. Isotopes ^{40}Ar, ^{39}Ar, ^{38}Ar and ^{37}Ar were measured on Faraday collectors with ^{40}Ar and ^{37}Ar using a 1012 Ohm resistor, ^{39}Ar using a 1013 Ohm resistor, and ^{38}Ar using a 1014 Ohm resistor. ^{36}Ar was measured on a compact discrete dynode (CDD) ion counter that has a dead time of 20 ns. Due to the low K/Ca of the hornblende, CaF_2 was analysed at the same time as the sample to help ensure accurate correction for production of ^{36}Ar and ^{39}Ar from irradiation of Ca.

Calibration gases of air and a gas mixture enriched in radiogenic ^{40}Ar along with ^{39}Ar were analysed interspersed with the sample to monitor instrument drift and determine detector intercalibration factors. Extraction line blanks were analysed before and after data collection and are reported in the intensity data worksheet. All data collection was conducted with the in-house Pychron software and data reduction utilized MassSpec version 7.875.

The reported plateau age is derived from the weighted mean of the chosen steps with the weighting factor being the inverse variance (e.g., Taylor, 1982) and the error is the square root of the sum of $1/\sigma^2$ values. The plateau age error is reported at 1σ and includes the J-factor error and irradiation correction factor uncertainties.

Fig. 4.2. Ouassé outcrop. (a,b) Harzburgites with rounded or stretched orthopyroxene porphyroclasts (red circles) and tiny black spinel grains (blue circle). (c,d) Discordant high angle pyroxenites The thin whitish veins are made of serpentine. (e) Discordant low angle pyroxenite. (f) Concordant pyroxenite.

4.5. Petrography and mineralogy

Representative mineral major element compositions are listed in Table 4.1.

4.5.1. Harzburgites

The studied harzburgites consists of 70-80 vol% olivine, 20-30 vol% orthopyroxene (enstatite) and accessory Cr-spinel. Textures range from porphyroclastic to mylonitic (Fig. 4.3a-b). The foliation is defined by aligned and/or stretched orthopyroxene, with aspect ratio up to 12:1 (Fig. 4.3c) and olivine porphyroclasts.

Olivine and orthopyroxene porphyroclasts have refractory compositions (Fo = 91-92 mol% and Mg# = 91-92, respectively). Up to 1 cm-sized orthopyroxene porphyroclasts locally show undulous extinction and bending. Thin exsolution lamellae of clinopyroxene are also present. Orthopyroxene is characterised by relatively low Al_2O_3 contents (1.3-1.9 wt%; Fig. 4.6), slightly diminishing towards the rim (1.1-1.8 wt%). Cr_2O_3 and CaO contents show a broad decrease from core to rim (0.6-0.8 to 0.3-0.6 wt% and 0.6-1.1 to 0.4-0.7 wt%, respectively). Up to 1.5 mm dark brown to black spinel grains have anhedral to subhedral shapes and are locally organised in trails (Fig. 4.3d) concordant to the peridotite foliation. They have Cr# and Mg# ranging between 55-65 and 38-54 (Fig. 4.8), respectively, and low TiO_2 contents (≤0.13 wt%).

Porphyroclasts are set into a neoblastic matrix made of fine-grained (mostly 100-400 µm) olivine + orthopyroxene ± spinel displaying a polygonal texture. Neoblastic olivine has 91-93 mol% forsterite. Orthopyroxene neoblasts are mainly rounded crystals lacking exsolution lamellae. Overall, they display slightly lower Al_2O_3 (0.9-1.4 wt%) and Cr_2O_3 (0.3-0.7 wt%) contents compared to porphyroclasts (Fig. 4.6); CaO contents range between 0.5 and 1.1 wt%. Spinel shows Cr# values of 52-56 and Mg# values of 44-47 with TiO_2 contents up to 0.1 wt%. Fine-grained (up to 200 µm) clinopyroxene (diopside) was rarely found, locally associated to neoblastic olivine in small embayments on porphyroclastic orthopyroxene rim. It displays (Fig. 4.7) very high Mg# values (94-95) coupled to Cr_2O_3 contents ranging from 0.4 to 0.8 wt% and low Al_2O_3 contents (1.0-1.5 wt%). Tiny amphibole with pseudo-prismatic to rounded shape may be associated with the neoblastic assemblage. It has an edenitic composition (according to Leake et al., 1997) and Mg# values of 91-92, high Cr_2O_3 (2.0-2.6 wt%) and low TiO_2 contents (≤0.2 wt%).

Up to 0.5 cm-thick veins made of talc ± calcite ± magnetite crosscut the harzburgite foliation. Close to the vein, harzburgitic orthopyroxenes may be replaced by the secondary mineral vein assemblage. Further away, talc + calcite occasionally occur as small veins cutting the orthopyroxene crystals and substitute the neoblastic aggregates.

4.5.2. Orthopyroxenites

The orthopyroxenite samples are composed of ~95 vol% enstatitic orthopyroxene and accessory Cr-spinel, but differ for the minor components, as well as for the texture.

Orthopyroxenite OU5A shows a disequigranular texture made of medium- to coarse-grained (up to 0.5 cm) orthopyroxenes set into a fine-grained granoblastic polygonal matrix (Fig. 4.4a). Orthopyroxenes have a stubby prismatic shape and bear very thin Ca-rich exsolution lamellae. They have irregular rims and embayments formed by the granoblastic polygonal assemblage (Fig. 4.4b). Locally, some crystals are truncated by the fine-grained assemblage. The latter is mainly composed of subhedral orthopyroxene grains, ~5 vol% clinopyroxene, frequently showing triple junction points (Fig. 4.4c) and accessory amphibole. Granoblastic pyroxenes do not exhibit exsolution lamellae. The orthopyroxene grains have high Mg# values (90-91; Fig. 4.6). Al_2O_3, Cr_2O_3 and CaO contents slightly diminish from core (1.8-2.1, 0.7-1.0 and 0.5-1.0 wt%, respectively) to rim (1.6-1.9, 0.5-1.0 and 0.4-0.6 wt%). Clinopyroxene is a diopside up to 100 μm in size. It is characterised by high Mg# values (93), low Al_2O_3 contents (2.2-2.5 wt%), Na_2O and Cr_2O_3 contents of 0.4-0.5 and 1.0-1.5 wt%, respectively (Fig. 4.7). Accessory amphibole occurs as up to 100 μm in size crystals in the granoblastic assemblage, substituting clinopyroxene grains. It is a Cr-rich (Cr_2O_3 = 1.9-2.3 wt%) edenite showing nearly constant TiO_2 and Na_2O contents (~0.4 and ~1.9 wt%, respectively) and remarkably high Mg# values (92-93). Fine-grained (up to ~250 μm) dark brown to black chromian (Cr# = 57-61; Fig. 4.8) spinel occurs throughout the sample. It has cubic to anhedral habitus and relatively low TiO_2 contents (~0.1 wt%) coupled to Mg# values of 45-48. The sample is crosscut by up to ~1.5 mm-sized veins of secondary talc + calcite ± magnetite.

Sample OU8 is an olivine-bearing orthopyroxenite (Ol ~5 vol%), showing a medium- to coarse-grained cumulitic texture. Orthopyroxene mainly has a stubby shape (Fig. 4.4d) and is up to 1.5 cm in size. It is frequently highly fractured, but cleavages are still well identifiable. Orthopyroxene (Fig. 4.6) has high Mg# values (92), Al_2O_3, Cr_2O_3 and CaO contents comparable to those of the sample OU5a (1.5-1.9, 0.5-0.8 and 0.4-0.9 wt%, respectively). Olivine (Fig. 4.9; Fo = 92 mol%; NiO = 0.5-0.6 wt%) shows rounded to anhedral habitus and is up to 1.5 mm. Locally, it is included at the orthopyroxene rim (Fig. 4.4e). Spinel is a dark brown to black crystal up to 500 μm in size, displaying cubic, prismatic or anhedral shapes. Its TiO_2 contents reach up to 0.1 wt%. Mg# values range from 56 to 64 and Cr# values cluster at ~52 Veins consisting of talc + calcite cut the orthopyroxenite. Locally, anhedral, elongated spinel is associated to the secondary assemblage.

4.5.3. Amphibole-bearing websterites

Enstatitic orthopyroxene (~ 25-70 vol%) and augitic to diopsidic clinopyroxene (~ 25 vol%) are the main constituents of the sampled websterites. Edenitic amphibole occurs in variable amounts (~ 5-40 vol%) and plagioclase is locally present (up to ~ 3 vol% in sample OU1). Spinel occurs as an accessory phase. In samples OU1 and OU4, the texture is disequigranular and is made of medium- to coarse-grained (up to ~ 2.5 mm) pyroxenes set into a fine- to medium-grained granoblastic polygonal assemblage (Fig. 4.5a).

Medium- to coarse-grained pyroxenes have prismatic to subhedral habitus and octagonal basal sections are locally observed. They locally show mutual thin exsolution lamellae and are characterised by numerous inclusions. The latter are mostly concentrated at the core region and mainly consist of rounded, tabular, or anhedral amphibole. Orthopyroxene and spinel (TiO_2 = 0.6 wt%, Cr# = 0.7 and Mg# = 22) are minor inclusions. Clinopyroxene twins can also be easily found (Fig. 4.5b).

The granoblastic polygonal matrix (down to ~ 100 μm) is constituted by orthopyroxene ± clinopyroxene ± amphibole ± plagioclase (Fig. 4.5c) and frequently shows triple junction points. Interlobate, irregular boundaries among crystals are locally observed. Recrystallized pyroxenes lack exsolution lamellae and are sometimes substituted by amphibole at their rims. Amphibole is green to light brown crystal showing a pseudo-prismatic to anhedral habitus. It mainly occurs as an interstitial phase and locally displays a poikilitic texture surrounding pyroxenes (Fig. 4.5d). Cubic spinel grains are rarely included (TiO_2 = 2.3 wt%, Cr# = 66-73 and Mg# ~ 8).

A websterite sample (OU7B) consists of coarse-grained (up to ~ 2 cm) subhedral clinopyroxene, orthopyroxene and amphibole displaying mutually interfingered crystals. They mostly share interlobate boundaries and mutual inclusions (Fig. 4.5e). Up to 1 mm amphibole and apatite grains are found associated to medium-grained pyroxenes collectively intersecting a cm-sized amphibole crystal. Apatite has a prismatic or rounded shape and is associated to amphibole (Fig. 4.5f). Rare Fe-Ni sulphides occur as cubic crystals in amphibole. Edenitic amphibole and pyroxenes are commonly substituted by secondary tremolite (Al_2O_3 = 1.3-3.6 wt%, Mg# = 92-95), notably towards the contact with the host harzburgite.

Locally, mafic minerals may be partially altered into a mixture of chlorite + serpentine + talc ± smectite. Websterite OU1 shows interstitial patches made of sericite.

Mineral major element compositions are overall homogeneous among the samples and texture-related chemical variations were not observed. Orthopyroxene has relatively low Al_2O_3 contents (0.6-1.2 wt%; Fig. 4.6). CaO contents range from 0.6 to 0.9 wt%. Cr_2O_3 contents (0.1-0.4 wt%) increase at decreasing Mg# values (78-89). Clinopyroxene shows relatively low Al_2O_3, Cr_2O_3 (Fig. 4.7) and Na_2O contents (0.6-2.1, 0.1-0.3 and 0.1-0.4 wt%, respectively). Higher TiO_2 contents (0.1-0.2 wt%)

are coupled to progressively lower Mg# values (81-90). Edenite largely displays increasing TiO_2 contents (0.3-1.2 wt%) with increasing Al_2O_3 contents (7.5-11 wt%). Mg# values range from 78 to 88, whilst Na_2O contents mainly cluster at ~1.5-2.0 wt%. Plagioclase has 82-86 mol% anorthite.

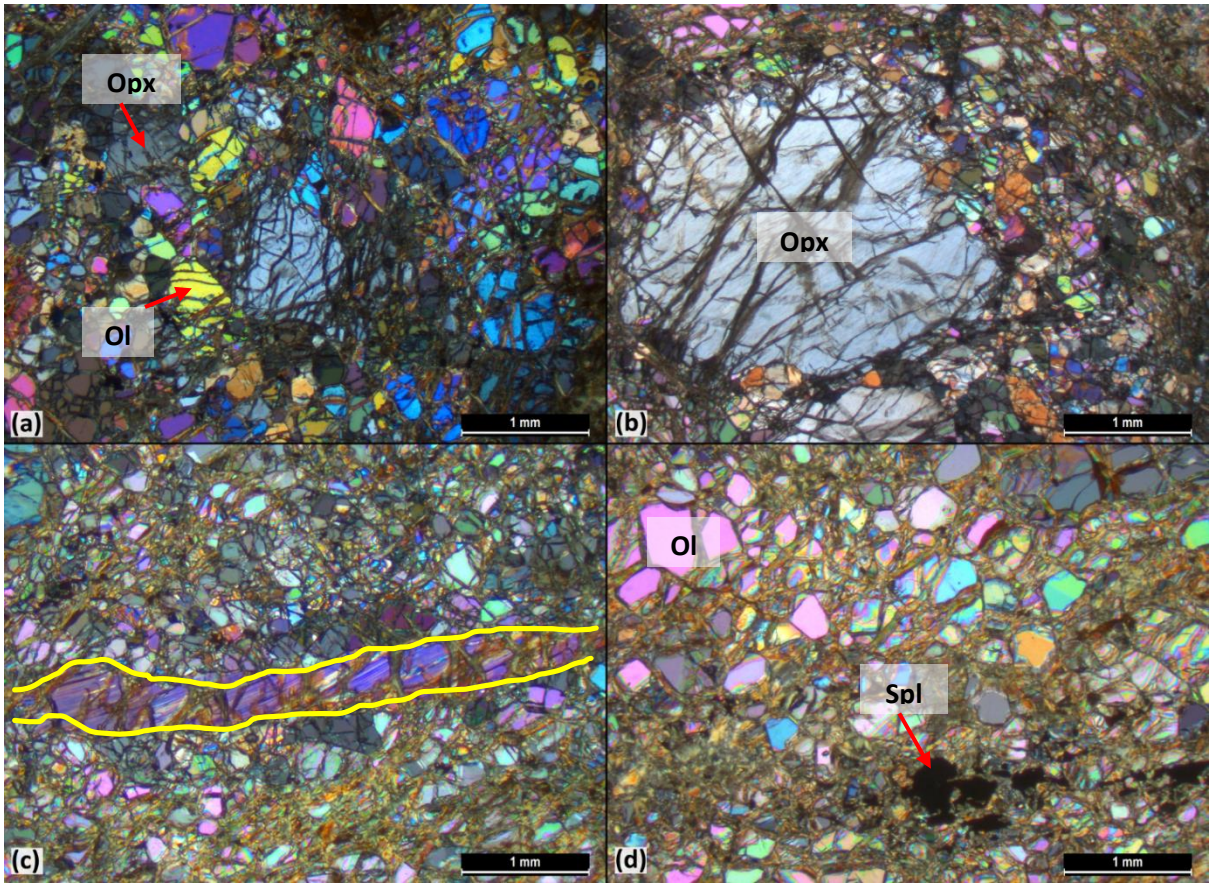

Fig. 4.3. Thin section photomicrographs under cross-polarized light of Ouassé harzburgites. (a) Porphyroclastic texture. (b) Mylonitic texture with coarse-grained orthopyroxene porphyroclast associated with the neoblastic assemblage. (c) Highly stretched orthopyroxene porphyroclast, showing aspect ratio of 12:1. (d) Trails of spinel grains. Mineral abbreviations are after Whitney and Evans (2010).

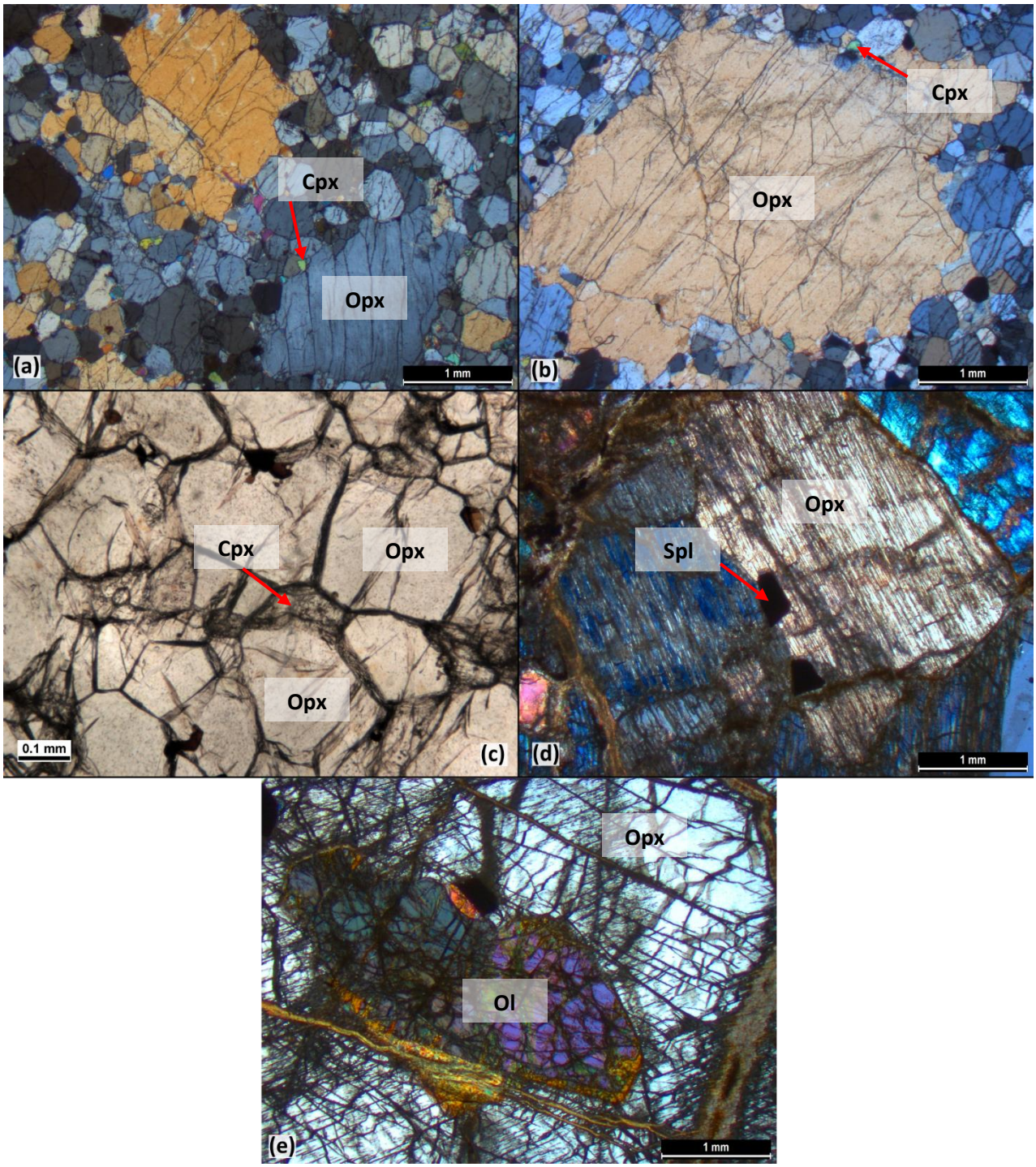

Fig. 4.4. Thin section photomicrographs under cross-polarized (a,b,d,e) and plane-polarized (c) light of Ouassé orthopyroxenites. (a,b) Medium- and coarse-grained orthopyroxenes set into a fine-grained granoblastic polygonal matrix in orthopyroxenite OU5A. (c) Granoblastic polygonal crystals showing triple junction points in orthopyroxenite OU5A. (d) Coarse-grained orthopyroxene in orthopyroxenite OU8. (e) Olivine crystal included at the orthopyroxene rim in orthopyroxenite OU8. Mineral abbreviations are after Whitney and Evans (2010).

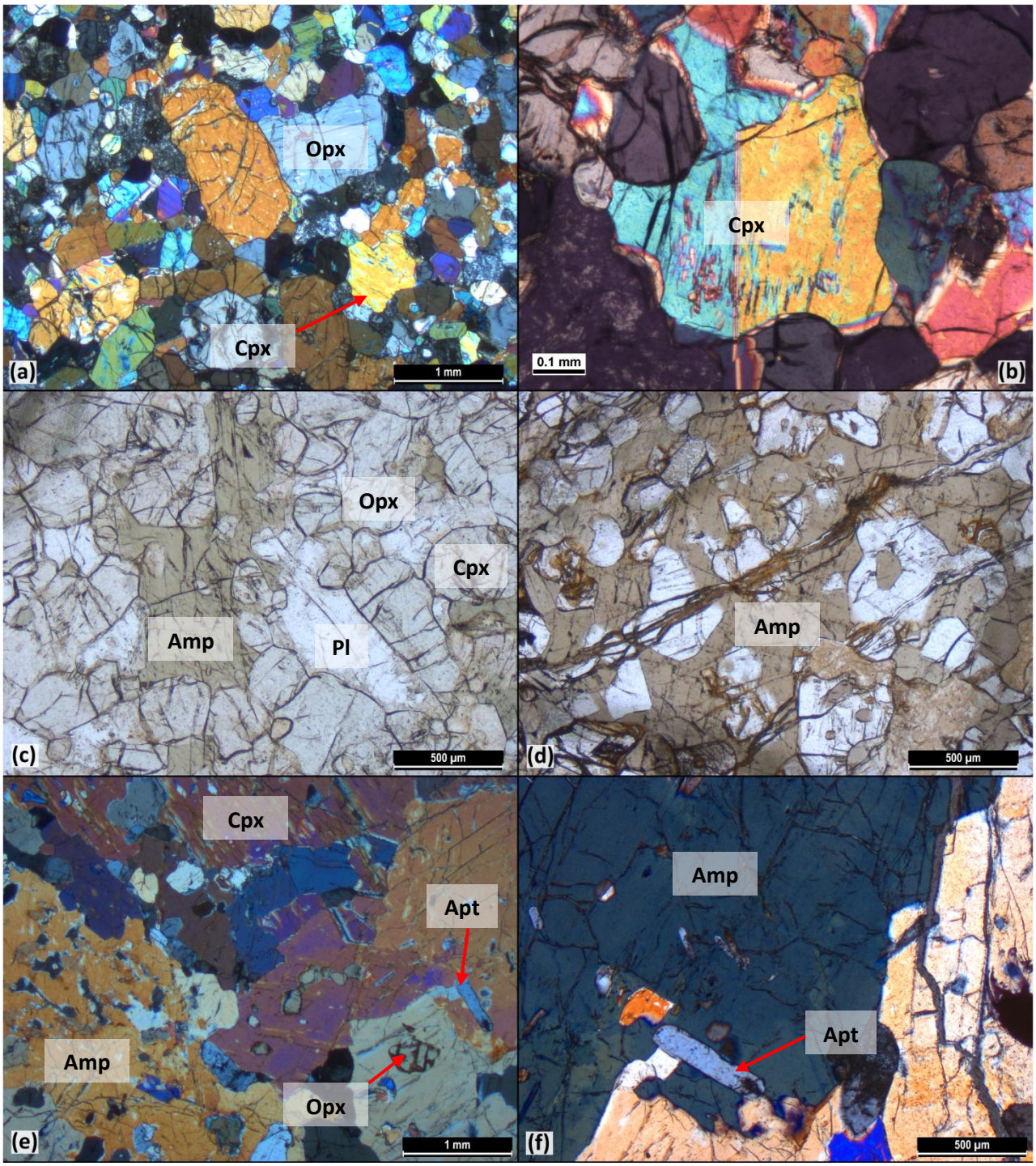

Fig. 4.5. Thin section photomicrographs under cross-polarized (a,b,e,f) and plane-polarized (c,d) light of Ouassé amphibole-bearing websterites. (a) Medium- to coarse-grained pyroxenes set into a granoblastic polygonal assemblage in websterite OU4. (b) Clinopyroxene twinned crystal in websterite OU1. (c) Amphibole crystal associated with the granoblastic polygonal assemblage in websterite OU1. (d) Poikilitic amphibole surrounding pyroxenes in websterite OU1. (e) Texture of websterite OU7B. (f) Apatite crystal associated with amphibole in websterite OU7B. Mineral abbreviations are after Whitney and Evans (2010).

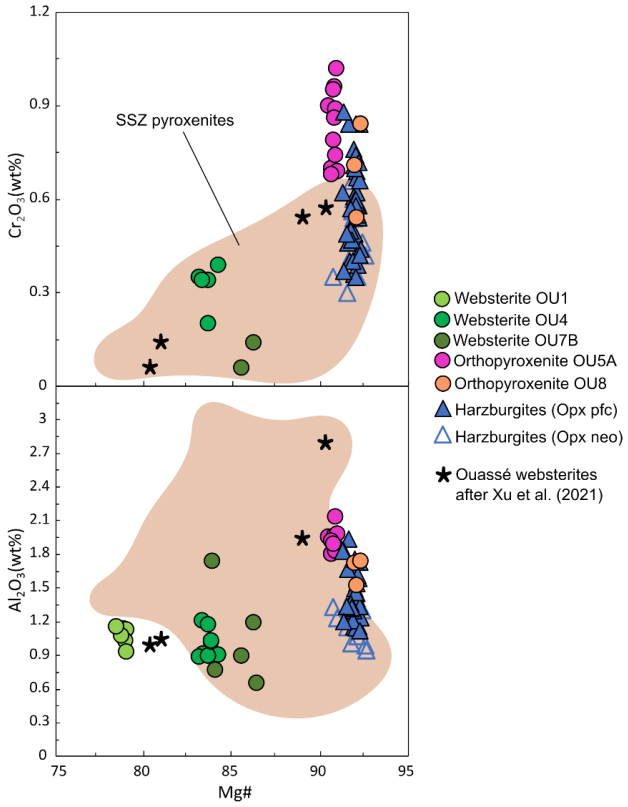

Fig. 4.6. Cr_2O_3 and Al_2O_3 vs. Mg# for orthopyroxene cores from Ouassé samples. Data from other Ouassé websterites studied by Xu et al. (2021) are shown for comparison. Field for supra-subduction zone (SSZ) pyroxenites includes data from Berly et al. (2006), Choi et al. (2008), Varfalvy et al. (1997), Bénard et al. (2016), Tamura and Arai (2006), Tilhac et al. (2016).

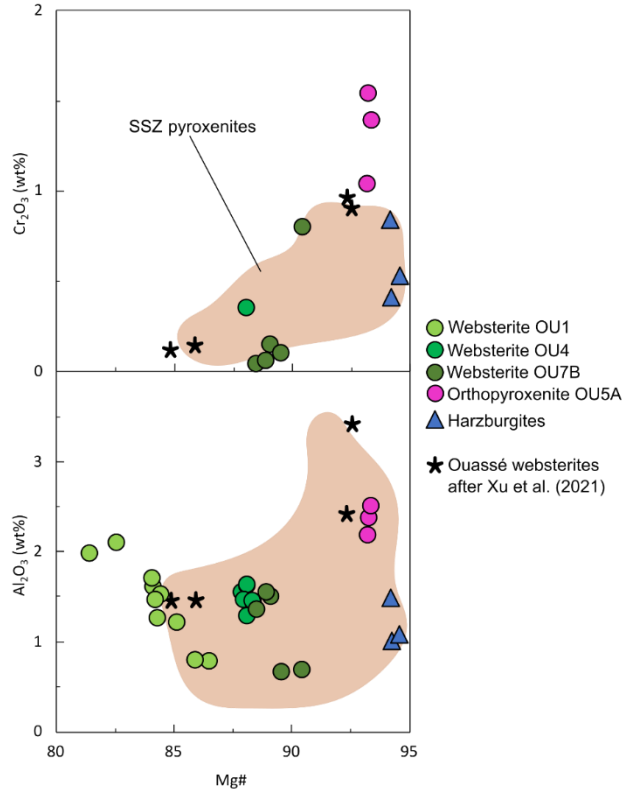

Fig. 4.7. Cr_2O_3 and Al_2O_3 vs. Mg# for clinopyroxene cores from Ouassé samples. Data from other Ouassé websterites studied by Xu et al. (2021) are shown for comparison. Field for supra-subduction zone (SSZ) pyroxenites includes data from Berly et al. (2006), Choi et al. (2008), Varfalvy et al. (1997), Bénard et al. (2016), Tamura and Arai (2006), Tilhac et al. (2016).

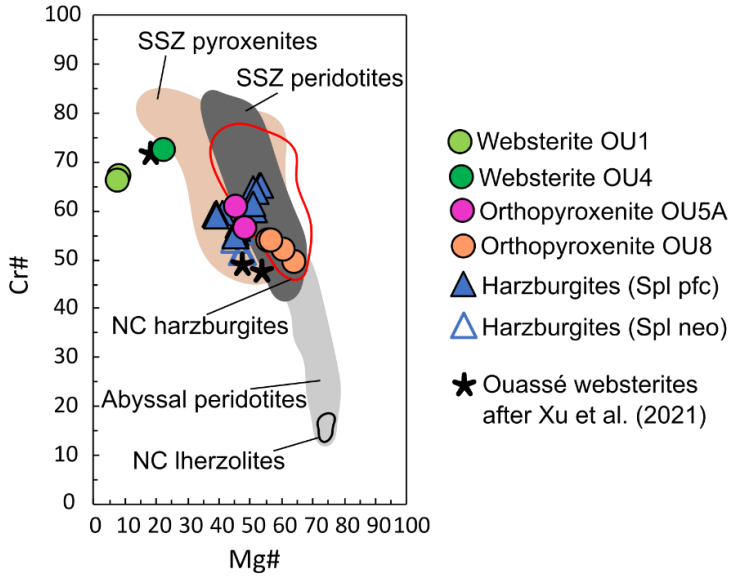

Fig. 4.8. Cr# vs. Mg# values of spinels from Ouassé samples. Data from other Ouassé websterites studied by Xu et al. (2021) are shown for comparison. Field for supra-subduction zone (SSZ) and abyssal peridotites are after Dick and Bullen (1984) and Arai (1994). Field for SSZ pyroxenites includes data from Berly et al. (2006), Choi et al. (2008), Varfalvy et al. (1997), Bénard et al. (2016), Tamura and Arai (2006). Field for New Caledonia harzburgites includes data from Marchesi et al. (2009), Ulrich et al. (2010), Pirard et al. (2013), Secchiari et al. (2020), Xu et al. (2021). Field for New Caledonia lherzolites includes data from Secchiari et al. (2016)

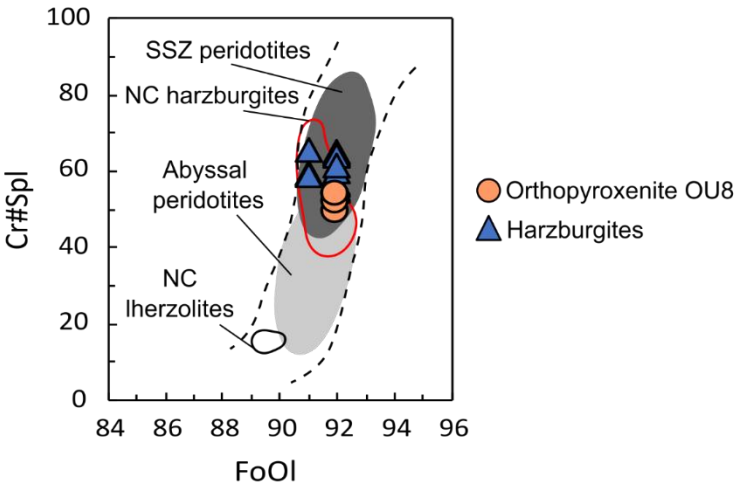

Fig. 4.9. Cr#Spl vs. FoOl for Ouassé samples. Field for supra-subduction zone (SSZ) and abyssal peridotites are after Dick and Bullen (1984) and Arai (1994). Field for New Caledonia harzburgites includes data from Marchesi et al. (2009), Ulrich et al. (2010), Pirard et al. (2013), Secchiari et al. (2020), Xu et al. (2021). Field for New Caledonia lherzolites includes data from Secchiari et al. (2016). The black dashed lines define the Olivine-Spinel Mantle Array (OSMA).

4.6. Whole rock compositions

Bulk rock major and trace element compositions of harzburgite and pyroxenite samples are listed in Table 4.2.

4.6.1. Major elements

Loss On Ignition (LOI) values of harzburgites (7.41-8.80 %) are generally higher than those of pyroxenites (0.22-5.62), reflecting their moderate serpentinization degree. Major element compositions were recalculated on anhydrous basis and normalized to 100.

Mg# values (91-92) and major element compositions of the harzburgites ($TiO_2 \leq 0.002$ wt%, Al_2O_3 = 0.4-0.5 wt%, CaO = 0.4-0.5 wt%, $Na_2O \leq 0.07$ wt%) are in the range of the other New Caledonia harzburgites which recorded high degrees partial melting (Fig. 4.10; Marchesi et al., 2009; Ulrich et al., 2010; Secchiari et al., 2020).

Orthopyroxenites and harzburgites show similar Mg# values (91-92). The sample OU8 has very low TiO_2 contents (0.004 wt%) comparable to host peridotites, whilst slightly higher values (0.03 wt%) are displayed by the sample OU5A. Low Al_2O_3 (~ 2 wt%), CaO (1.1-1.8 wt%) and Na_2O (~ 0.1 wt%) contents characterise both orthopyroxenites.

Websterites have variable and lower Mg# values (82-89) compared to the orthopyroxenites. They also show higher TiO_2 (0.1-0.3 wt%) and CaO (7.1-12 wt%), in accordance with the higher modal amounts of clinopyroxene and amphibole. Increasing CaO, Al_2O_3 (1.3-7.1) and Na_2O (0.1-0.7 wt%) contents among the websteritic rocks might reflect higher proportions of amphibole and, at a lesser extent, of plagioclase from sample OU4 to OU7B to OU1. Small amounts of P_2O_5 (0.06 wt%) were detected by sample OU7B, testifying the occurrence of accessory apatite.

4.6.2. Trace elements

The studied peridotites show V (~ 23 ppm), Cr (2160-2550 ppm) and Ni (2260-2400 ppm) contents similar to the New Caledonia harzburgites of the literature (Fig. 4.11; Marchesi et al., 2009; Ulrich et al., 2010; Secchiari et al., 2020). Orthopyroxenite OU8 has remarkably high Ni contents (2890 ppm), higher than the host harzburgites and orthopyroxenite OU5A (960 ppm). Cr, Sc and V contents are nevertheless similar to orthopyroxenite OU5A, collectively clustering at ~ 5800, ~ 18 and ~ 89 ppm. Websterites have lower Cr (460-1170 ppm) and Ni (360-800 ppm) contents. Websterites are distinguished from orthopyroxenites also for higher Sc (47-56 ppm) and V (118-218 ppm) contents. For the pyroxenites, increasing Ni contents are associated to increasing Mg# values (Fig. 4.11).

Orthopyroxenite OU5A shows low REE abundances, ~ 0.1 to 1.0 times chondritic values. The REE pattern is concave upward with nearly flat LREE and a slight increase in HREE with respect to MREE (Gd_N/Yb_N = 0.3). REE contents are mostly below detection limits in orthopyroxenite OU8. Websterites are more enriched lithotypes (Fig. 4.12; REE ~ 1.0 to 10 x chondrite) displaying variably depleted LREE patterns (La_N/Sm_N = 0.3-0.9) and MREE enrichment relative to HREE (Gd_N/Yb_N = 1.7-1.9). Small Eu negative anomalies occur in samples OU4 and OU7B (Eu/Eu* = 0.8).

In Primitive Mantle normalized diagram (Fig. 4.13), positive Sr, Zr and Ti spikes characterise orthopyroxenite OU5A. Websterites show higher abundances compared to orthopyroxenites and host harzburgites. As for chondrite-normalized REE patterns, concentrations tend to increase, on average, from sample OU4 to OU1 to OU7B. All samples share Ti negative anomalies. Websterite OU1 displays a strong positive Sr spike, in contrast to pyroxenites OU4 and OU7B which exhibit weak and more pronounced negative anomalies, respectively.

4.7. Mineral trace elements composition

Representative mineral trace element compositions of pyroxenites are reported in Table 4.3.

4.7.1. Orthopyroxenites

Sample OU5A has orthopyroxene with REE contents mostly < 1.0 times chondritic values and LREE negatively fractionated over HREE. Clinopyroxene shows a slight LREE depletion (La_N/Sm_N = 0.6) and a positive Eu anomaly (Eu/Eu* = 1.2). Low absolute concentrations of incompatible elements (from 0.03 to 0.8 times primitive mantle values) are coupled to a positive anomaly in Pb and negative anomalies in Zr and Ti (Fig. 4.14). Amphibole displays nearly flat HREE (Gd_N/Yb_N = 1.2) and depletion in Nb and Hf.

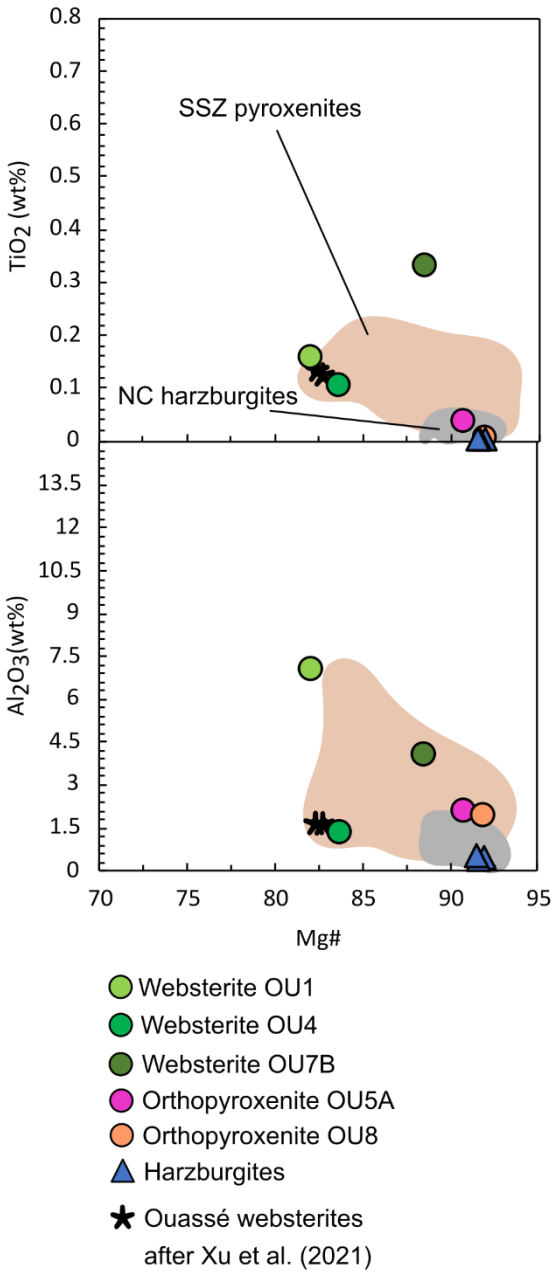

Fig. 4.10. TiO_2 and Al_2O_3 vs. Mg# of Ouassé whole rocks. Data from other Ouassé websterites studied by Xu et al. (2021) are shown for comparison. Field for New Caledonia harzburgites includes data from Marchesi et al. (2009), Ulrich et al. (2010), Secchiari et al. (2020). Field for supra-subduction zone (SSZ) pyroxenites includes data from Berly et al. (2006), Varfalvy et al. (1997), Tilhac et al. (2016), Rogkala et al. (2017), Eslami et al. (2021).

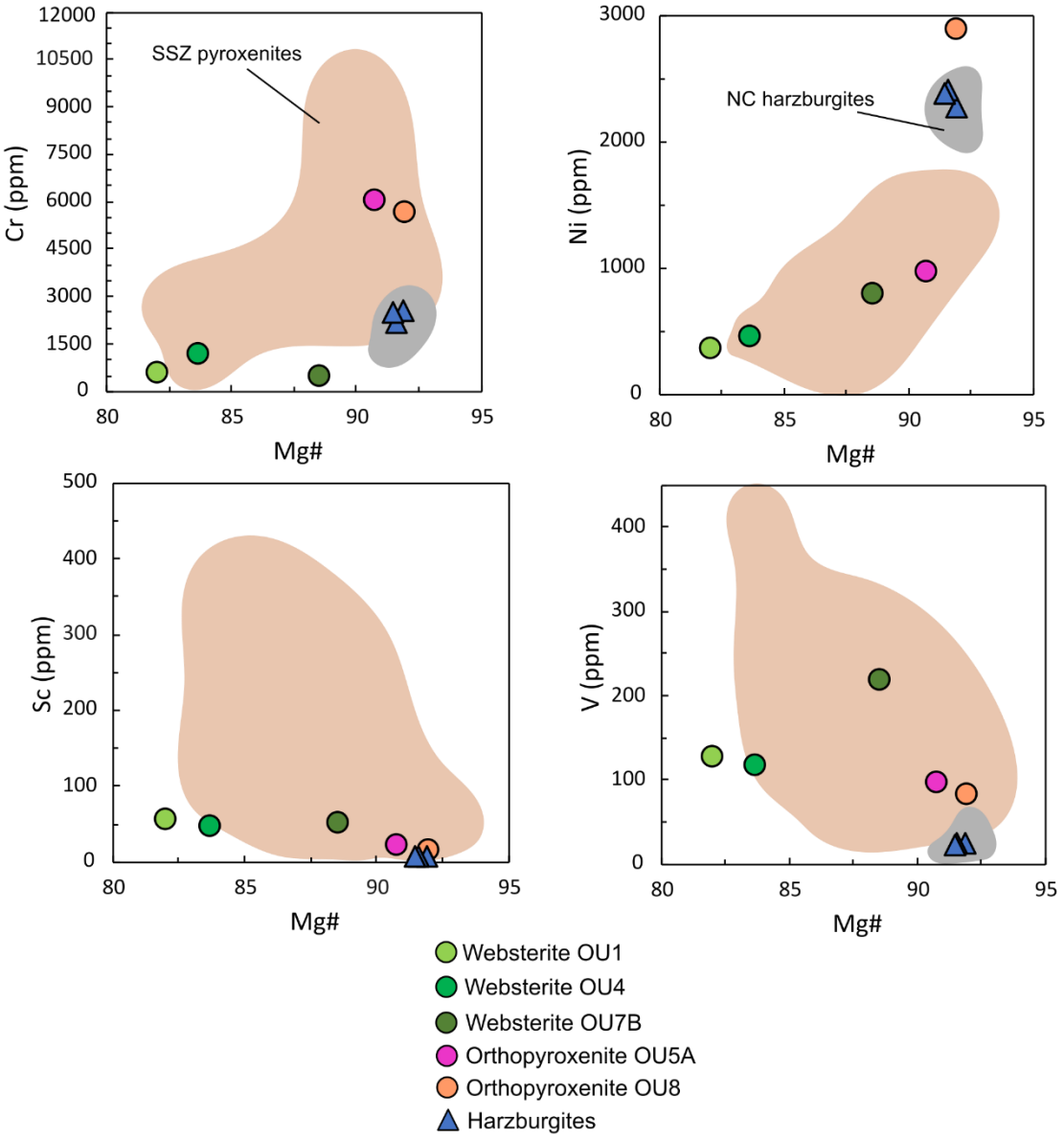

Fig. 4.11. Cr, Ni, Sc, V vs. Mg# of Ouassé whole rocks. Field for New Caledonia harzburgites includes data from Marchesi et al. (2009), Ulrich et al. (2010), Secchiari et al. (2020). Field for supra-subduction zone (SSZ) pyroxenites includes data from Berly et al. (2006), Varfalvy et al. (1997), Tilhac et al. (2016), Rogkala et al. (2017), Eslami et al. (2021).

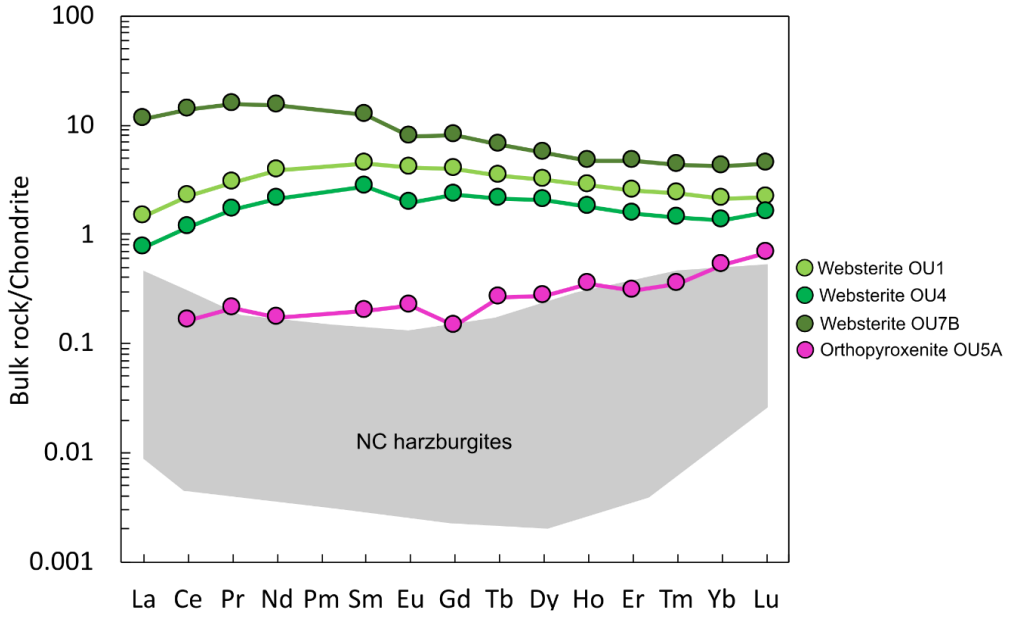

Fig. 4.12. Rare Earth Elements compositions of Ouassé pyroxenites normalized to chondrite (normalizing values after Sun and McDonough, 1989). Field for New Caledonia harzburgites includes data from Marchesi et al. (2009), Ulrich et al. (2010), Secchiari et al. (2020).

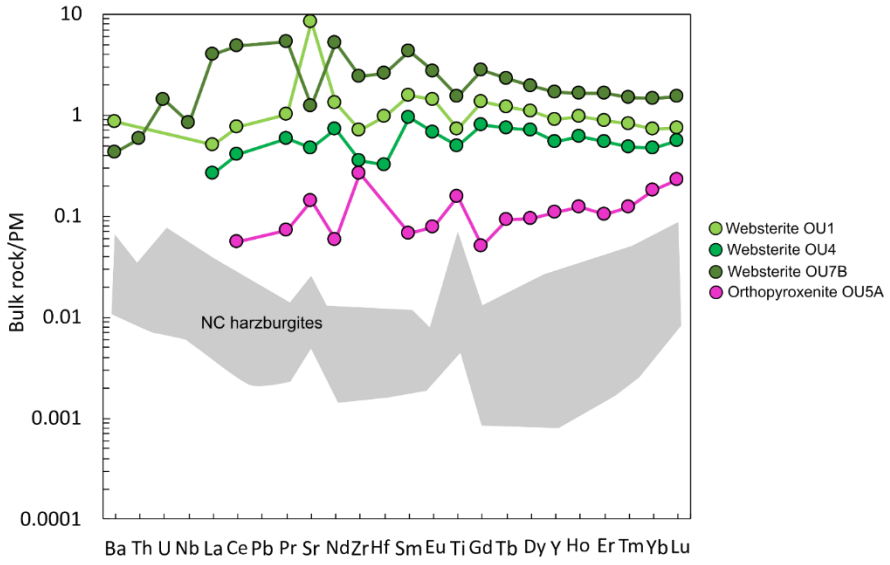

Fig. 4.13. Extended incompatible trace element diagram for Ouassé pyroxenites normalized to Primitive Mantle (normalizing values after Sun and McDonough, 1989). Field for New Caledonia harzburgites includes data from Marchesi et al. (2009), Ulrich et al. (2010), Secchiari et al. (2020).

4.7.2. Amphibole-bearing websterites

Clinopyroxene has REE contents ranging from ~2 to 10 times chondritic values. It shows variably depleted LREE (La_N/Sm_N = 0.1-0.6), weak to moderate negative Eu anomalies (Eu/Eu* = 0.7-0.9) and nearly flat HREE. In addition, negative anomalies are observed for Pb, Sr, Zr and Ti elements (Fig. 4.14).

Orthopyroxene has very low REE contents in OU1 and OU4 websterites (~ 0.1-1 times chondritic values), whilst higher concentrations are displayed by sample OU7B (~1-4 times chondritic values). The orthopyroxene is characterized by increasing concentrations from LREE to HREE. Orthopyroxene from sample OU7B has a positive Eu anomaly (Eu/Eu* = 1.8).

Amphibole displays high REE contents, up to 30 times chondritic values. It has a convex REE pattern characterized by a strong depletion in LREE (La_N/Sm_N = 0.2-0.7) and HREE (Gd_N/Yb_N = 1.9-2.0) and a very weak negative Eu anomaly (Eu/Eu* = 0.9). Amphibole from sample OU7B displays a positive LREE fractionation over HREE, Fig. 4.15). In Primitive Mantle normalized trace element diagram all amphiboles show negative peaks in Pb, Sr and Zr. The edenitic amphibole from the recrystallized matrix of harzburgite sample OU7A shows REE contents up to ~10 times chondritic values, characterized by a strong LREE enrichment (La_N/Sm_N = 1.6) and MREE positively fractionated over HREE (Gd_N/Yb_N = 1.3). It broadly mirrors the amphibole REE pattern of the host websterite OU7B, but at lower absolute concentrations.

Plagioclase from pyroxenite OU1 has high LREE concentrations (mostly ~1-5 times chondritic values; Fig. 4.16), whilst M- and HREE contents are <1 times chondritic values. It is characterized by LREE enrichment (La_N/Sm_N = 1.2-4.4) and prominent positive Eu anomalies (Eu/Eu* = 3.3-11).

Apatite from websterite OU7B has extremely high REE contents (~20 to ~1100 times chondritic values; Fig. 4.16), progressively decreasing from LREE to HREE. It shows a steep L- to MREE fractionation and nearly flat HREE.

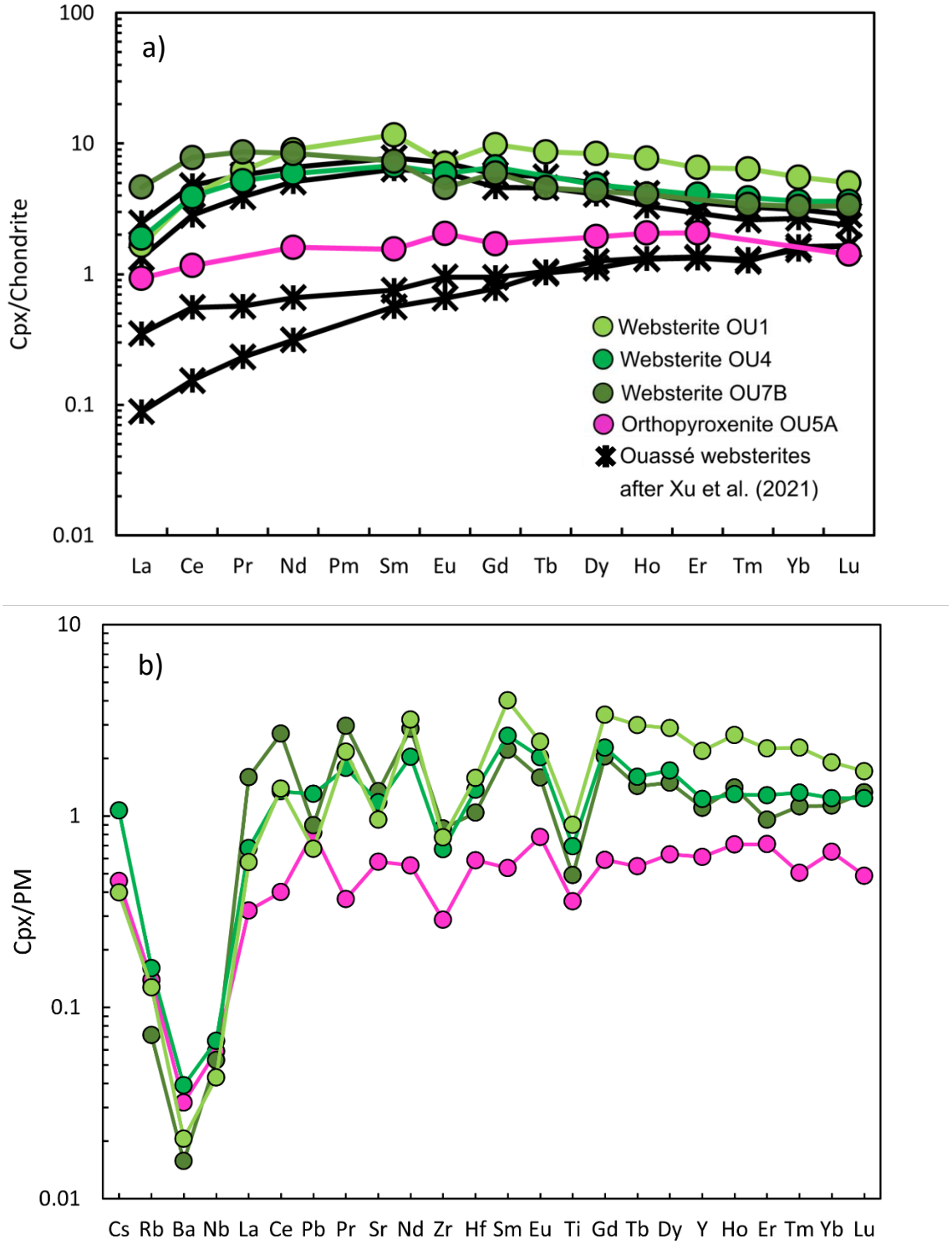

Fig. 4.14. (a) Rare Earth Elements and (b) extended incompatible trace elements diagrams for clinopyroxenes from Ouassé pyroxenites normalized to chondrite and Primitive Mantle, respectively (normalizing values after Sun and McDonough, 1989). Data from other Ouassé websterites studied by Xu et al. (2021) are shown for comparison.

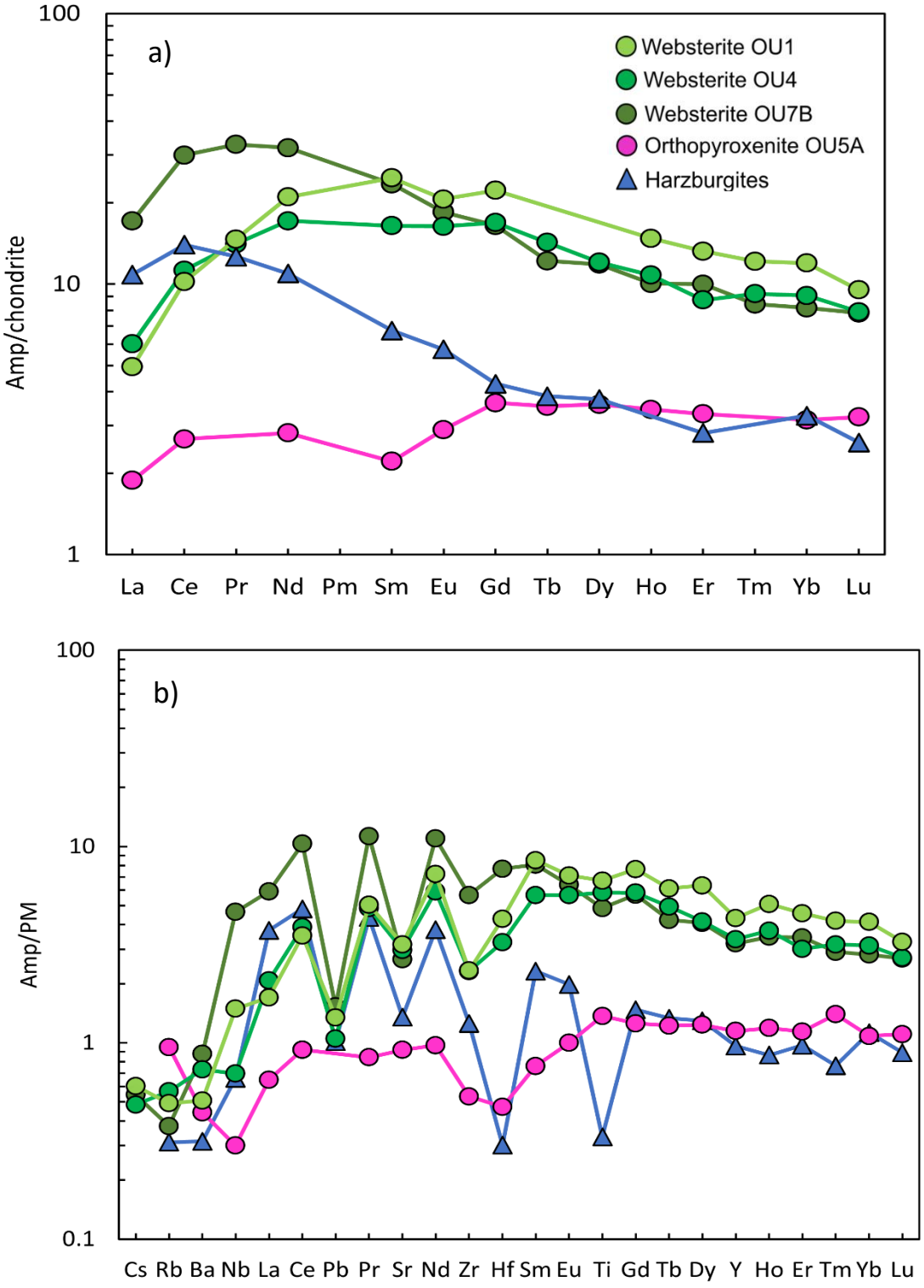

Fig. 4.15. (a) Rare Earth Elements and (b) extended incompatible trace elements diagrams for amphiboles from Ouassé pyroxenites normalized to chondrite and Primitive Mantle, respectively (normalizing values after Sun and McDonough, 1989).

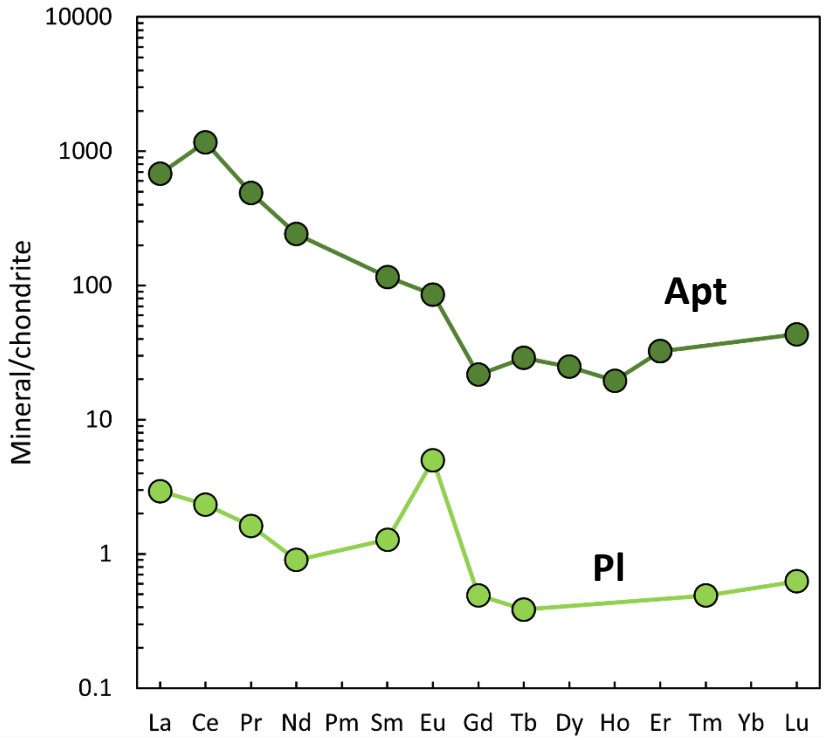

Fig. 4.16. Rare Earth Elements compositions for plagioclase and apatite from Ouassé amphibole-bearing websterites OU1 and OU7B, respectively. Chondritic normalizing values are after Sun and McDonough (1989).

4.8. Geothermometry

Equilibrium temperatures calculated for host harzburgites and enclosed pyroxenite layers are listed in Table 4.4. Pressure conditions were assumed equal to 1 GPa, considering the spinel-facies conditions of the host harzburgites. The applied methods are the following:

- two-pyroxene thermometers of Taylor (1998; referred to as T_{Ta98}) and Brey and Köhler (1990; referred to as T_{BK90}), based on the Fe^{2+}-Mg exchange between coexisting clinopyroxene and orthopyroxene
- Ca-in-orthopyroxene thermometer of Brey and Köhler (1990; referred to as $T_{Ca\text{-}in\text{-}Opx}$), based on the Ca content of orthopyroxene
- olivine-spinel thermometer of Jianping et al. (1995; referred to as $T_{Ol\text{-}Spl}$), based on the Fe^{2+}-Mg exchange between coexisting olivine and spinel
- Ca-in-olivine thermometer of De Hoog et al. (2010; referred to as $T_{Ca\text{-}in\text{-}Ol}$), based on the Ca content of olivine
- amphibole-plagioclase thermometer of Holland and Blundy (1994; referred to as T_{HB94}), based on the compositions of coexisting amphibole and plagioclase
- thermometers based on the partitioning of slowly diffusing elements (REE-Y), between (i) clinopyroxene and orthopyroxene (Liang et al., 2013; referred to as $T_{REE\text{-}Px}$), and (ii) clinopyroxene and plagioclase (Sun and Liang, 2017; referred to as $T_{REE\text{-}Cpx\text{-}Pl}$).

The porphyroclastic assemblage of Ouassé harzburgites yielded Ca-in-Opx temperatures ranging from 920 to 970 °C at the orthopyroxene core. Remarkably lower values (730-750 °C) were obtained for olivine-spinel cores. Slightly lower temperatures were recorded by the neoblastic assemblage ($T_{Ca\text{-}in\text{-}Opx}$ = 920-945 °C, T_{Ta98} = 880-920 °C, T_{BK90} = 890-930 °C, $T_{Ol\text{-}Spl}$ = 720 °C).

Orthopyroxenite OU5A recorded Ca-in-Opx temperatures of 920-930 °C, T_{Ta98} = 894 °C and T_{BK90} = 910 °C. Orthopyroxene cores from sample OU8 recorded the lowest Ca-in-Opx temperatures (870 °C). Olivine-spinel and Ca-in-olivine thermometers gave values of 865 and 861 °C, respectively, consistent with the Ca-in-Opx estimate.

Thermometers based on slowly diffusing elements (REE, Y) were applied on the websteritic assemblages. Sample OU1 yielded values of 1251 ± 37 °C for the clinopyroxene-orthopyroxene pair and values of 1310 ± 14 °C were provided by clinopyroxene and plagioclase. Comparable temperatures were obtained from the core of the coarse clinopyroxene-orthopyroxene (1264 ± 50 °C) and the core of the granoblastic pyroxenes (1249 ± 52 °C) from sample OU4. Conventional geothermometry applied to pyroxene cores provided $T_{Ca\text{-}in\text{-}Opx}$ = 965-995 °C, T_{Ta98} = 930-970 °C and

T_{BK90} = 915-965 °C. These values are in the range of those from the host harzburgites. The amphibole-plagioclase geothermometer applied on sample OU1 gave consistent temperatures of 970 °C.

4.9. $^{40}Ar/^{39}Ar$ amphibole dating

Two magmatic amphibole (edenite) separates from websterites OU1 and OU7B were analysed for $^{40}Ar/^{39}Ar$ dating and the results are reported in Table 4.5 and Figure 4.17.

The two samples show low amounts of excess argon ($^{40}Ar/^{36}Ar$ = ~295-297) and display good concordances between the plateau ages and the isochron ages (Tab. 4.5). Well-defined plateau ages can be seen in Figure 4.17.

The plateau ages of the two samples (OU1 = 56.01 ± 0.19 Ma; OU7B = 56.05 ± 0.17 Ma) are nearly undistinguishable and cluster at 56 Ma.

4.10. Discussion

4.10.1. Nature and evolution of hosting peridotites

Overall, major element mineral and whole rock compositions of the Ouassé harzburgites are in the range of the other New Caledonia mantle harzburgites which were extensively studied in previous works (Marchesi et al., 2009; Ulrich et al., 2010; Secchiari et al., 2020). In particular, according to Secchiari et al. (2020), the harzburgites are ultra-refractory peridotites recording a two-stage melting process including an anhydrous melting event which possibly occurred in a marginal basin and a subsequent fluid-assisted melting in a forearc environment. Post-melting reactive percolation of depleted melts led to crystallization of secondary pyroxenes (e.g., Secchiari et al., 2020) and produced variable enrichments in several incompatible trace elements (L- and MREE, LILE and some HFSE, see also Xu et al., 2021a).

The highly refractory nature of Ouassé harzburgites is supported by (i) the absence of primary clinopyroxene, (ii) the very low bulk rock Al_2O_3 (0.4-0.5 wt%) and CaO (0.4-0.5 wt%) contents coupled to high MgO contents (46-47 wt%), (iii) the high Cr# values (55-65) coupled to low TiO_2 contents (≤0.1 wt%) in spinels, (iv) the high forsterite content in olivine (Fo = 91-92 mol%) and (v) the high Mg# values (91-92) of orthopyroxene porphyroclasts associated with low Al_2O_3 contents (1.1-1.9 wt%).

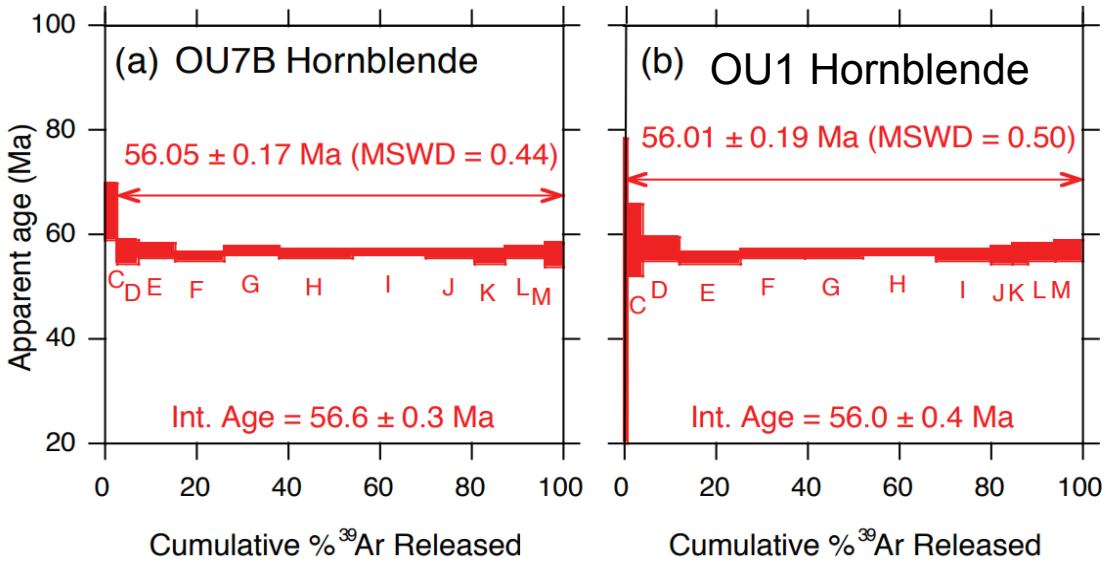

Fig. 4.17. $^{40}Ar/^{39}Ar$ age spectra for two amphibole separates from Ouassé websterites OU1 and OU7B.

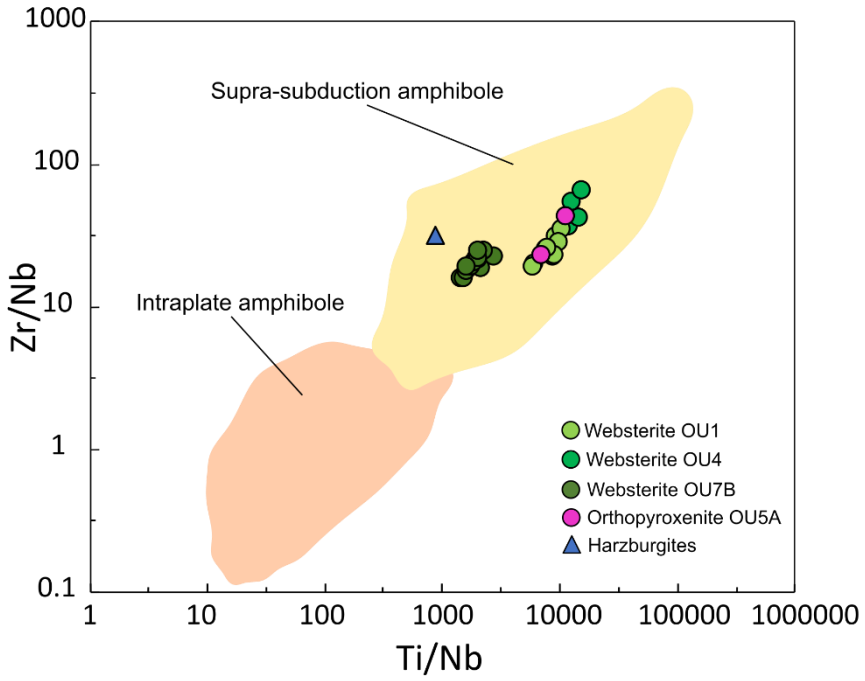

Fig. 4.18. Zr/Nb vs. Ti/Nb of amphiboles from Ouassé samples. Fields of supra-subduction and intraplate amphibole are after Coltorti et al. (2007).

Remarkably, the Ouassé harzburgites were affected by intense deformation, that produced mylonitic textures and highly stretched orthopyroxene porphyroclasts (Fig. 4.3c). Deformation in the study area is linked to the Bogota Peninsula Shear Zone, one of the three regional-scale high temperature shear zones of the Peridotite Nappe (see §Geological and petrological setting). Deformation was accompanied by recrystallization and grain size reduction, as testified by the fine-grained (~ 100-400 μm) neoblastic assemblage (ol + opx ± spl). Secondary clinopyroxene crystallized among neoblasts, suggesting deformation synchronous to percolation of melt or fluids capable to precipitate clinopyroxene. Amphibole of edenitic composition was also locally found within the neoblastic assemblage. The presence of amphibole relatively enriched in incompatible elements (Table 4.3, Fig. 4.15) in a highly depleted harzburgite points to a metasomatic origin. Its Ti/Nb and Zr/Nb ratios (Fig. 4.18) are coherent with an origin in a supra-subduction zone (Coltorti et al., 2007). Teyssier et al. (2016) also reported the presence of fine-grained interstitial pargasite in Bogota mylonites. They proposed that the high temperature amphibole originated from percolating fluids initially derived from the subduction context and subsequently related to ocean water infiltration.

Ca-in-orthopyroxene equilibration temperatures of neoblastic pyroxenes range from 920 to 945 °C. These estimates suggest fairly high temperature conditions for the deformation. They are comparable to those calculated for the porphyroclastic orthopyroxene ($T_{Ca\text{-}in\text{-}Opx}$ = 890-970 °C), in agreement with the absence of significant differences in major element compositions between porphyroclasts and neoblasts. These temperatures fall in the range of those reported by other authors (Teyssier et al., 2016; Chatzaras et al., 2020) for the Bogota Peninsula Shear Zone. Significantly lower temperatures were obtained for neoblastic (720 °C) and porphyroclastic (730-750 °C) olivine-spinel pairs (Jianping et al., 1995). Considering that the olivine-spinel thermometer is based on faster element diffusion compared to the Ca-in-orthopyroxene, the remarkable temperature difference detected by the two geothermometers suggest a relatively slow cooling and slow thermal equilibration of the studied mantle sector.

4.10.2. Origin of the pyroxenite layers

Whole rocks and minerals chemistry of Ouassé orthopyroxenites and amphibole-bearing websterites are consistent with the compositions of supra-subduction zone pyroxenites reported in the literature (see Figs. 4.6,4.7,4.8,4.9,4.10,4.11).

4.10.2.1. Orthopyroxenites

The presence of orthopyroxenite layers in mantle suites is generally ascribed to percolating silica-rich melts. Pyroxenes from Ouassé orthopyroxenites are characterized by very low Al_2O_3 contents

(1.5-2.5 wt%) coupled to very high Mg# values (90-93), suggesting an origin from a supra-subduction agent, as reported, for instance, by Müntener et al. (2001), Morishita et al. (2003) and Arai et al. (2006) for rocks crystallized from hydrous silica-rich melts showing high Mg# andesite to boninite-affinity.

The presence of clinopyroxene in orthopyroxenite OU5A allowed the calculation of parental liquids in equilibrium with this mineral. Trace element analysis performed on clinopyroxene and cpx/liquid partition coefficients from the compilation of Hart and Dunn (1993) returned the composition of the equilibrium melt (Tab. 4.6). Its REE pattern (Fig. 4.19a) shows contents up to ~ 20 times chondrite values, with LREE positively fractionated over MREE ($La_N/Sm_N = 3.2$) and nearly flat HREE ($Gd_N/Yb_N = 0.9$). Positive Ba, Pb and Sr anomalies and negative Ti anomaly are displayed in a N-MORB normalized extended trace element diagram (Fig. 4.19b). Enrichments in LREE, LILE (Ba, Sr) and Pb are typical of slab-derived hydrous silicate melts, rather than aqueous fluids (Zheng, 2019). Mg# of the equilibrium melt (computed according to the equation of Wood and Blundy, 1997) is equal to 80. The high Mg# suggest an origin from a refractory source (e.g., Pearce, 1982). According to this, both pyroxenes have refractory compositions with high Mg# values (90-93). Boninite-like liquids could be a good candidate for a silica-rich melt in equilibrium with such a depleted source (Pearce and Reagan, 2019), as the New Caledonia Peridotite Nappe is crosscut by dikes with boninite affinity (Cluzel et al., 2006; Xu et al., 2021a) and boninite rocks were emplaced at its base (Cluzel et al., 2016). Fig. 4.19 shows a good match between the calculated liquid representing the parental melt of orthopyroxenite OU5A and the field of New Caledonia boninites, as well as the pattern of pre-obduction boninite-like dikes. Boninitic rocks from New Caledonia were interpreted as the product of low degree partial melting of a depleted peridotite source previously enriched by slab-derived felsic melts (Cluzel et al., 2016). The small percentage of clinopyroxene (~ 5 vol%) in sample OU5A likely reflects the Ca-poor composition of the whole rock which could be explained by the low-Ca nature of New Caledonia boninites (Cluzel et al., 2016). Textural evidence show that the amphibole grew at the expense of clinopyroxene. Its geochemical features (e.g. Ti/Nb and Zr/Nb ratios Fig. 4.18) are consistent with crystallization from a subduction-related agent (Coltorti et al., 2007). The boninite-like melt was injected in the deforming harzburgite, as evidenced by the orientation of the orthopyroxenite dike concordant to the peridotite foliation. In addition, equilibration temperatures gave values consistent with those of the host harzburgite ($T_{Ca\text{-}in\text{-}Opx}$ = 920-930 °C).

The orthopyroxenite OU8 has peculiar features, as (i) the high Ni contents (2890 ppm), which exceeds the values displayed by all the New Caledonia harzburgites and (ii) the extremely low REE contents (< 0.1 times chondritic values). Most of the elements appearing in the bulk rock extended

trace element diagram were not detectable as well, suggesting an overall refractory nature of orthopyroxenite OU8. This is confirmed by orthopyroxene (Mg# = 92) and olivine compositions (Fo = 92 mol%). Given its refractory composition and the low Al_2O_3 contents in orthopyroxene, it could be hypothesized that it represents a cumulus rock originated from a silica-rich boninite-like liquid (Müntener et al., 2001). The presence of olivine included in orthopyroxene suggests crystallization of olivine before orthopyroxene. This would reflect the crystallization sequence from a boninitic melt (Pearce et al., 1984).

4.10.2.2. Amphibole-bearing websterites

Besides the similarities with other subduction-related pyroxenites of the literature (Figs. 4.6,4.7,4.8,4.9,4.10,4.11), bulk rock major elements are also consistent with the websterites of Müntener et al. (2001), obtained experimentally through the crystallization of primitive arc basalts at 1.2 GPa. In particular, Ouassè websterites are in the range of those derived from high Mg# andesite. Further evidence comes from the composition of Ouassé pyroxenes. Indeed, they have very low Al_2O_3 contents (0.6-2.1 wt%), as also noticed by Müntener et al. (2001) for their websteritic samples and by several other authors for supra-subduction zone mantle rocks (e.g., Arai et al., 2006; Morishita et al., 2003). This feature is ascribed to crystallization from hydrous silica-rich melts showing high Mg# andesite to boninite-affinity. In order to verify this hypothesis, clinopyroxene from websterites was used for the geochemical characterization of parental liquids (Tab. 4.6). Trace element composition of the liquids in equilibrium with clinopyroxenes were calculated using the Cpx/melt partition coefficients of Hart and Dunn (1993). The obtained liquids (Fig. 4.19a) have MREE positively fractionated over HREE ($Gd_N/Yb_N \sim 2.0$) and negative Eu anomalies (Eu/Eu* = 0.6-0.9). They differ in being slightly depleted (OU1, $La_N/Sm_N = 0.8$) to enriched (OU4 and OU7B, $La_N/Sm_N = 1.5$, 3.4, respectively) in LREE. Overall, they show distinct REE patterns and higher concentrations (~ 10 to 100 times chondrite values) compared to the equilibrium melt of orthopyroxenite OU5A. In a N-MORB normalized trace element diagram (Fig. 4.19b), the calculated websterite liquids display depletion in HFSE elements (Ti, Zr, Hf) and negative anomalies in Sr (liquids OU1 and OU7B) and Pb (liquid OU7B). Once again, these patterns are different and more enriched compared to that of OU5A liquid. As a whole, websterite liquids are enriched in LREE and LILE over HREE and HFSE. These features are consistent with slab-related silica-rich components; moreover, the widespread presence of primary amphibole suggest an hydrous character. Calculated Mg# values of equilibrium melts (Wood and Blundy, 1997) increase from sample OU1 (58) to OU4 (67) to OU7B (69). They are lower than that of OU5A liquid, pointing to less primitive melts and/or a less refractory source, maybe also not peridotitic. In particular, Mg# value of OU1 liquid is not consistent with mantle-

derived melts, which display higher values (> 60; e.g., Stern and Kilian, 1996). A slab-derived melt would have even lower Mg# values (10-40; Kelemen, 1995). A reaction between slab-derived melt and supra-subduction mantle is proved to increase the Mg# value of the resulting liquid (Kelemen 1995; Stern and Kilian, 1996; Carroll and Wyllie, 1989) and could explain the intermediate value of liquid OU1. Thus, the distinct Mg# values of the three websteritic liquids could be a consequence of (i) evolving melts after fractional crystallization, (ii) different degrees of interaction with the peridotite during their way to surface, (iii) genetically different melts or (iv) a combination of the latter two. Fig. 4.20 shows Sr/Y ratios plotted against Mg# values of the liquids. A linear correlation exist among the websteritic samples, with decreasing Sr/Y ratios at decreasing Mg# values. This positive correlation cannot be explained by evolving liquids after fractional crystallization as an opposite trend should be viewed. Therefore, the websteritic liquids (i) could derive from the same slab melt that reacted in varying proportions with the mantle peridotite during ascent or with a mantle-derived melt or (ii) could derive from genetically distinct melts. Equilibrium melt of sample OU7B is distinguished from the other two in having a considerable enrichment in LREE and a rather steep pattern decreasing from LREE to HREE. In addition, the mineral assemblage of the amphibole-bearing websterite OU7B is characterized by the peculiar occurrence of accessory apatite (+ sulphides). The presence of apatite could indicate a derivation from alkaline melts. Alternatively, as the apatite is not widespread, but it is only locally found in sample OU7B, it could represent a crystallization product from a highly differentiated trapped melt. Hence, it can be speculated that the melt which originated OU7B layer is of a different nature than those related to samples OU1 and OU4.

REE and trace element patterns of liquid OU7B are similar to those of some enriched boninites (Fig. 4.19) for which the involvement of an OIB component was hypothesized (Falloon et al., 2007; Price et al., 2016). Foden et al. (2020) described similar patterns for a high Mg andesite with boninitic affinity, i.e. a volcanic rock with andesitic silica contents and high MgO contents showing similarities with the low-Ca boninites. OU1 and OU4 liquids have patterns comparable to those presented by Zhao and Asimow (2014) for some Neoproterozoic volcanic rocks from South Cina. Their origin was explained by the interaction of a boninite-like melt with a slab sediment melt. All these evidence point to the existence of a boninitic component coupled to a more enriched component (OIB or sediment/crust slab) for the different websterite-forming liquids. The boninitic component is expressed by the relatively low Sr/Y ratio (7.4-21; Defant and Drummond, 1990), whilst the enriched component triggered a relative enrichment of LREE and LILE over HREE and HFSE. The prominent Ti negative anomalies could reflect a mantle contribution according to its refractory nature. As an hypothesis, the negative Eu anomalies of the liquids could be due to the presence of plagioclase as a

solid residue after slab melted at a pressure not greater than 1.5 GPa. This could explain also the negative Sr anomalies in the N-MORB normalized trace element diagram.

To sum up, the different geochemical features and patterns of the websteritic liquids would suggest genetically distinct melts, at least for sample OU7B. Overall, the websteritic liquids share similarities with enriched boninites. The presence of amphibole would also indicate an hydrous component, presumably derived from the sinking slab. Common subduction-related hydrous silica-rich melts are termed adakite and generally represent liquids directly coming from the melted slab. Pooling all these observations together, it could be hypothesised that the websteritic liquids represent the products of slab-derived and mantle-derived melts likely mixed in different proportions.

Some similarities in whole rock and REE clinopyroxene compositions were detected between sample OU4 and some Ouassé websterites studied by Xu et al. (2021). The latter were interpreted as cumulate products from boninitic melts which could have interacted with the surrounding peridotites. Xu et al. (2021) also provided Sr, Nd, Hf isotopic data and $^{187}Os/^{188}Os$ ratios on the websteritic samples: they are isotopically depleted and their parental melts presumably originated from a Depleted MORB Mantle (DMM) source. High two-pyroxene-REE temperatures (1159-1452 °C) were related to the pyroxenite-forming melt-peridotite interaction process. Comparable estimates are displayed by OU1 and OU4 samples (~1250 °C).

4.10.3. Insights on the New Caledonia Paleocene-Eocene subduction initiation

As discussed above, the Ouassé mantle section is characterized by a series of subduction-related pyroxenite dikes. These layers are mostly discordant with the host harzburgite foliation. Orthopyroxenite OU5A is the unique concordant dike. This indicates emplacement during peridotite deformation. Strain deformation also affected this pyroxenite layer which is locally boudinaged.

The other studied dikes are variably discordant. Clear sharp contacts with the host peridotite are also visible from the amphibole-bearing websterites OU1 and OU4. These features suggest that their emplacement occurred by hydraulic fracturing of a brittle mantle, being thus relatively colder than it was during the deformation phase.

The various dikes were sampled at a few hundreds of meters of distance. Thus, they come from comparable levels of the mantle column. Based on all the above observations, a cooling temporal evolution of the mantle section is marked by the shift from ductile to brittle behaviour. Following this, a relative chronology could be established among the different pyroxenite layers. In particular, the concordant orthopyroxenite OU5A was emplaced before the other dikes.

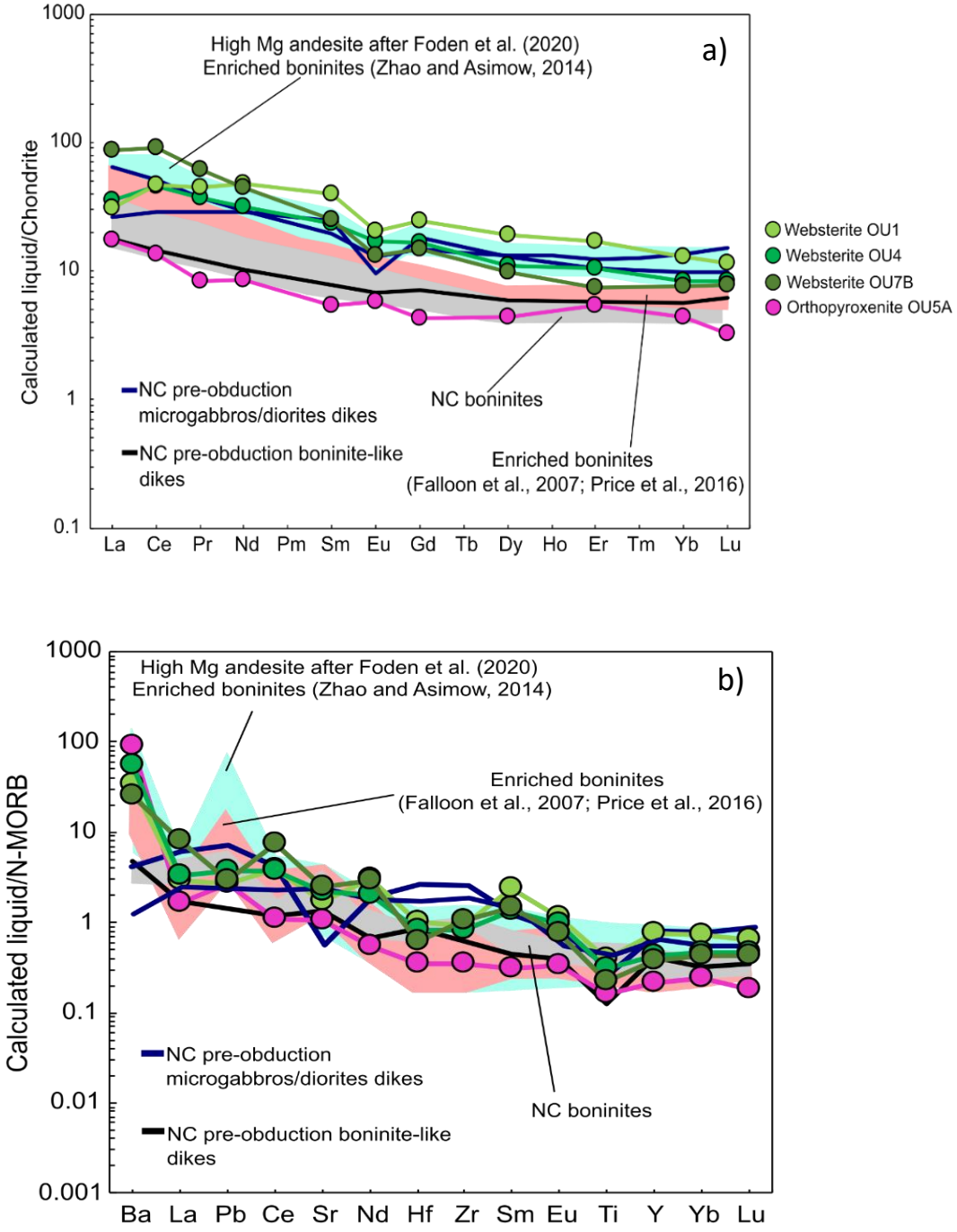

Fig. 4.19. (a) Rare Earth Elements and (b) incompatible trace elements diagrams for calculated liquids in equilibrium with clinopyroxenes from Ouassé pyroxenites normalized to chondrite and N-MORB, respectively (normalizing values after Sun and McDonough, 1989). Boninites from New Caledonia (Cluzel et al., 2016), enriched boninites (Zhao and Asimow, 2014; Falloon et al., 2007; Price et al., 2016) and high Mg andesite (Foden et al., 2020) are shown for comparison. Patterns for New Caledonia pre-obduction dikes (Cluzel et al., 2006) are also reported.

$^{40}Ar/^{39}Ar$ amphibole dating of websterites OU1 and OU7B gave plateau ages of 56.01 ± 0.19 Ma (MSWD = 0.5) and 56.05 ± 0.17 Ma (MSWD = 0.44), respectively. The two ages are essentially undistinguishable. Similar ages are reported in the literature and were attributed to the NE-dipping subduction initiation (e.g., Cluzel et al., 2012a). Due to the relatively low closure temperature of the K-Ar system in amphibole (500-600 °C; Villa et al., 1996), the obtained values represent cooling ages. Thus, ~56 Ma is a minimum age of subduction inception, in agreement with van de Lagemaat et al. (2018) that set at ~ 60 Ma the initiation of New Caledonia NE-dipping subduction based on seismic tomography data and plate tectonic models. Following the relative chronology criteria among Ouassé pyroxenite dikes, orthopyroxenite OU5A was, thus, one of the very first event of subduction-related melt percolation in the forearc mantle.

Collectively, Ouassé pyroxenites are connected to the earliest phase of the Paleocene-Eocene subduction. Indeed, the other subduction-related dikes and veins crosscutting the Peridotite Nappe mantle are partly younger (~ 55-47 Ma; Cluzel et al., 2006, 2016, 2020; Cluzel 2020; Xu et al., 2021b).

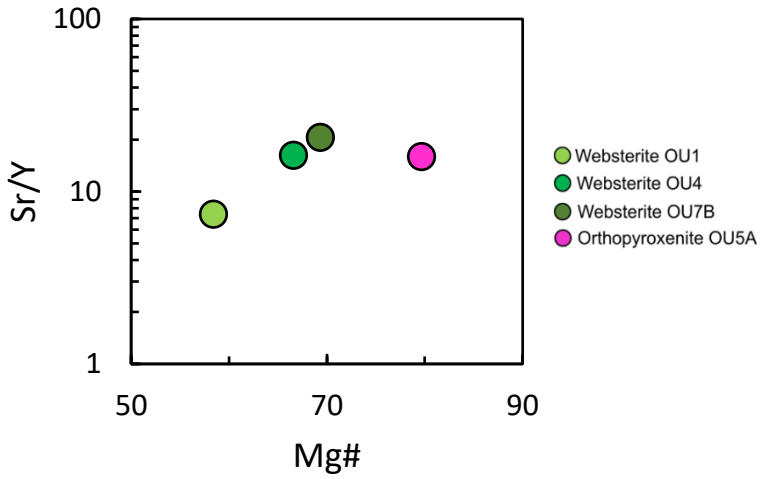

Fig. 4.20. Sr/Y vs. Mg# for calculated liquids in equilibrium with clinopyroxenes from Ouassé pyroxenites.

4.10.4. Evolution of the percolating melts/fluids in the forearc mantle

Few authors have made an attempt to decipher the temporal evolution of melts percolating the forearc mantle of the Peridotite Nappe. Cluzel (2020) hypothesised that melt sources changed through time, becoming progressively more depleted. In support of this, the author highlighted the transition from dikes showing undepleted IAB affinity dated at 55 Ma to those showing ultra-depleted IAT affinity dated at 50-47 Ma. By comparing the REE patterns of mafic-felsic dikes (Cluzel et al., 2006; Cluzel 2020; Xu et al., 2021b), boninites (Cluzel et al., 2016) and parental liquids of pyroxenitic dikes (this study; Xu et al., 2021a), a clear correlation between melt composition and age was not found.

Xu et al. (2021b) concluded that boninites were generated only in a second phase of the subduction inception event, at 51-47 Ma, when the harzburgitic mantle was highly depleted. This contrast with the existence of older (i) mafic-felsic dikes dated at ~ 54 Ma by Cluzel et al. (2016) and (ii) Ouassé orthopyroxenite layer OU5A emplaced before ~ 56 Ma (this study; see the above discussion), all showing boninitic affinity. Giving this evidence, the boninitic magmatism in the Peridotite Nappe was constantly present from the beginning of the subduction until, at least, 47 Ma and generated boninite-like rocks showing U-shaped REE patterns.

Taking into account the primitive nature (Mg# = 80) and the boninitic affinity of the parental melt of orthopyroxenite OU5A (i.e., the oldest subduction-related intrusion found in this study), a refractory mantle source existed at the time of subduction inception. This diverge from the Subduction Initiation Rule (SIR) formulated by Whattam and Stern (2011). They stated that Fore-Arc Basalts (FAB) are produced as a consequence of fertile asthenosphere upwelling during the early stages of subduction. Contributions from the subducting slab are minor in this first phase. Volcanic Arc Basalts (VAB) and minor boninites are generated only in a second phase, when the mantle has become more refractory and undergo fluid-assisted melting. According to the SIR, a geochemical evolution of the forearc melts comprises the transition towards more HFSE-depleted and LILE-enriched compositions. Percolating melts in the Peridotite Nappe mantle do not clearly display such a trend. Hypothetically, the early appearance of boninite-like liquids could be explained by an already depleted nature of the mantle at the time of subduction inception. It can also be speculated that the mantle acquired its ultra-refractory composition during the first stages of subduction inception, when intense forearc spreading established. Further fluid-assisted mantle melting triggered the first boninitic magmatism (prior to 56 Ma).

Intrusions showing FAB affinities are not reported in this study nor in the literature and could be due to the absence of this lithotype, though it is not possible to completely exclude the presence of

these rocks and further field surveys could enhance the studies in remote areas. Upper arc crust is missing (e.g., Cluzel et al., 2012b), thus rendering difficult to determine the existence of a FAB crust.

4.10.5. Hints for reinterpreting the significance of the Bogota Peninsula Shear Zone

The Bogota Peninsula Shear Zone (BPSZ) was generally considered as an oceanic paleotransform fault characterized by a dextral sense of motion (Prinzhofer and Nicolas, 1980; Titus et al., 2011; Chatzaras et al., 2020). The new data on Ouassé mantle rocks could provide new constraints on the BPSZ origin.

Ouassé mylonitic harzburgites developed secondary clinopyroxene and amphibole in the neoblastic assemblage, suggesting mylonitization concurrent to infiltration of slab-derived fluids/melts. In this view, the BPSZ was established in a supra-subduction environment. Accordingly, the subduction-related melt forming orthopyroxenite OU5A was injected in the harzburgites during deformation, as the pyroxenite layer is concordant with the host peridotites foliation. As discussed in the previous section, the subsequent intrusion of amphibole-bearing websterites is connected to a brittle behaviour of the mantle.

Different subduction-related scenarios could be invoked to explain the origin of the Bogota Peninsula Shear Zone:

- It could represent a transform fault related to a short-lived spreading center developed in the forearc region shortly after subduction initiation. A similar mechanism of seafloor spreading was hypothesised by Reagan et al. (2019) for the Izu-Bonin-Mariana system
- New Caledonia Paleocene-Eocene subduction inception is thought to occur near a spreading ridge and oblique subduction has been envisaged (Cluzel et al., 2021). The resulting transpressive forces could have deformed the hot and buoyant lithospheric mantle, thus creating the BPSZ
- The BPSZ could represent an old (Late Cretaceous-Paleocene) transform fault or at least a weak lithospheric mantle region of the South Loyalty Basin reactivated during the beginning of the Paleocene-Eocene subduction

Some considerations can be made in order to give at least some preferences over the above options. First, mylonitization occurred after partial melting of peridotites, not prior as partial melting could influence or hide deformation textures. Since Ouassé peridotites, like the other New Caledonia harzburgites, are interpreted to record subduction-related fluid-assisted partial melting, deformation is presumed to have occurred after this event and thus the third option can be discarded, as it would include a pre-existing shear zone preceding the subduction-related partial melting event. The first two

options seem to be more plausible and additional data are needed to better interpret the origin of the BPSZ.

4.11. Conclusions

The Ouassé mantle section shows a rare variety of subduction-related pyroxenites crosscutting the host harzburgites. In particular, orthopyroxenites and amphibole-bearing websterites were recognized. Each studied sample displays peculiar mineralogical characteristics, whereby, for instance, Ol-bearing and Cpx-bearing orthopyroxenites were distinguished. In addition, the websteritic rocks have variable amounts of primary amphibole (~5-40 vol%). From a chemical point of view, the orthopyroxenites show more refractory compositions compared to the amphibole-bearing websterites.

Beyond the characterization of the pyroxenitic samples, the main achievements of this PhD Thesis were (i) the identification of their parental liquids and (ii) their significance in the overview of the Eocene subduction. The main conclusions are:

- Equilibrium melts of the orthopyroxenites have a boninite-affinity.
- Equilibrium melts of the amphibole-bearing websterites are more enriched liquids compared to those of the orthopyroxenites. A derivation from enriched boninitic liquids and/or from adakite-like liquids is plausible.
- The $^{40}Ar/^{39}Ar$ cooling age of ~56 Ma referred to the websterites suggest that Ouassé pyroxenites represent one of the earliest magmatic products of melt percolation in the New Caledonia forearc mantle reported in the literature.

The results also allowed to give new insights on the significance of the Bogota Peninsula Shear Zone (BPSZ). In particular, the concordant orthopyroxenite layer found in the mylonitic harzburgites indicates the injection of boninitic liquids concurrent to the activity of the BPSZ. As the boninite-like liquids are typically subduction-related products, the shear zone should have been developed in a supra-subduction setting. Thus, it cannot be considered as a paleotransform fault merely related to a normal oceanic spreading ridge, as proposed by Prinzhofer and Nicolas (1980), Titus et al. (2011) and Chatzaras et al. (2020).

4.12. References

Arai S., 1994. Characterization of spinel peridotites by olivine-spinel compositional relationships: review and interpretation. Chemical Geology, 113:191-204

Arai S., Shimizu Y., Morishita T., Ishida Y., 2006. A new type of orthopyroxenite xenolith from Takashima, Southwest Japan: silica enrichment of the mantle by evolved alkali basalt. Contributions to Mineralogy and Petrology, 152:387-398

Bénard A., Nebel O., Ionov D.A., Arculus R.J., Shimizu N., Métrich N., 2016. Primary Silica-rich Picrite and High-Ca Boninite Melt Inclusions in Pyroxenite Veins from the Kamchatka Sub-arc Mantle. Journal of Petrology, 57:1955-1982

Berly T.J., Hermann J., Arculus R.J., Lapierre H., 2006. Supra-subduction Zone Pyroxenites from San Jorge and Santa Isabel (Solomon Islands). Journal of Petrology, 47:1531-1555

Brey G.P., Köhler T., 1990. Geothermobarometry in four-phase lherzolites II. New thermobarometers, and practical assessment of existing thermobarometers. Journal of Petrology, 31:1353-1378

Carroll M.R., Wyllie P.J., 1989. Experimental phase relations in the system tonalite-peridotite-H2O at 15 kb; implications for assimilation and differentiation processes near the crust-mantle boundary. Journal of Petrology, 30:1351-1382

Chatzaras V., Tikoff B., Kruckenderg S.C., Titus S.J., Teyssier C., Drury M.R., 2020. Stress variations in space and time within the mantle section of an oceanic transform zone: Evidence for the seismic cycle. Geology, 48:569-573

Choi S.H., Shervais J.W., Mukasa S.B., 2008. Supra-subduction and abyssal mantle peridotites of the Coast Range ophiolite, California. Contributions to Mineralogy and Petrology, 156:551-576

Cluzel D., 2020. Subduction erosion: contributions of footwall and hanging wall to serpentinite mélange; field, geochemical and radiochronological evidence from the Eocene HP-LT belt of New Caledonia. Australian Journal of Earth Sciences, 68:99-119

Cluzel D., Aitchison J.C., Picard C., 2001. Tectonic accretion and underplating of mafic terranes in

the Late Eocene intraoceanic fore-arc of New Caledonia (Southwest Pacific): geodynamic implications. Tectonophysics, 340:23-59

Cluzel D., Boulvais P., Iseppi M., Lahondère D., Lesimple S., Maurizot P., Paquette J.-L., Tarantola A., Ulrich M., 2020. Slab-derived origin of tremolite–antigorite veins in a supra-subduction ophiolite: the Peridotite Nappe (New Caledonia) as a case study. International Journal of Earth Sciences, 109:171-196

Cluzel D., Iseppi M., Chen Y., 2021. Eocene pre- and syn-obduction tectonics in New Caledonia (Southwest Pacific), a case for oblique subduction, transcurrent tectonics and oroclinal bending; structural and paleomagnetic evidence. Tectonophysics, 811

Cluzel D., Jourdan F., Meffre S., Maurizot P., Lesimple S., 2012a. The metamorphic sole of New Caledonia ophiolite: 40Ar/39Ar, U-Pb, and geochemical evidence for subduction inception at a spreading ridge. Tectonics, 31

Cluzel D., Maurizot P., Collot J., Sevin B., 2012b. An outline of the geology of New Caledonia; from Permian-Mesozoic southeast Gondwanaland active margin to Cenozoic obduction and supergene evolution. Episodes, 35:72-86

Cluzel D., Meffre S., Maurizot P., Crawford A.J., 2006. Earliest Eocene (53 Ma) convergence in the Southwest Pacific; evidence from pre-obduction dikes in the ophiolite of New Caledonia. Terra Nova, 18:395-402

Cluzel D., Ulrich M., Jourdan F., Meffre S., Paquette J.-L., Audet M.-A., Secchiari A., Maurizot P., 2016. Early Eocene clinoenstatite boninite and boninite-series dikes of the ophiolite of New Caledonia; a witness of slab-derived enrichment of the mantle wedge in a nascent volcanic arc. Lithos, 260:429-442

Coltorti M., Bonadiman C., Faccini B., Grégoire M., O'Reilly S.Y. and Powell W., 2007. Amphiboles from suprasubduction and intraplate lithospheric mantle. Lithos, 99:68-84

De Hoog J.C.M., Gall L., Cornell D.H., 2010. Trace-element geochemistry of mantle olivine and application to mantle petrogenesis and geothermobarometry. Chemical Geology, 270:196-215

Defant M.J., Drummond M.S., 1990. Derivation of some modern arc magmas by melting of young subducted lithosphere. Nature, 347:662-665

Dick H.J.B., Bullen T., 1984. Chromian spinel as a petrogenetic indicator in abyssal and alpine-type peridotites and spatially associated lavas. Contributions to Mineralogy and Petrology, 86:54-76

Eissen J.-P., Crawford A.J., Cotten J., Meffre S., Bellon H., Delaune M., 1998. Geochemistry and tectonic significance of basalts in the Poya Terrane, New Caledonia. Tectonophysics, 284:203-219

Eslami A., Borghini G., Montanini A., Grieco G., Marchesi C., 2021. Petrological constraints on the origin of pyroxenite dykes in the lithospheric mantle of the Cheshmeh-Bid ophiolitic massif, Southern Iran. Ofioliti, 46(1):63-81

Falloon T.J., Danyushevsky L. V., Crawford T. J., Maas R., Woodhead J. D., Eggins S. M., Bloomer S. H., Wright D. J., Zlobin S. K., Stacey A. R., 2007. Multiple mantle plume components involved in the petrogenesis of subduction-related lavas from the northern termination of the Tonga Arc and northern Lau Basin: Evidence from the geochemistry of arc and backarc submarine volcanics. Geochemistry, Geophysics and Geosystems, 8:1-45

Ferré E.C., Belley F., Tikoff B., Martín-Hernández F., Nzokwe G., Ward C., 2004. Anatomy of an oceanic mantle shear zone deduced from high-field magnetic anisotropy: the Humboldt corridor, New Caledonia. Eos Trans. AGU 85 (47). Fall Meeting Supplement, Abstract GP23B-04

Foden J., Elburg M., Turner S., Clark C., Blades M.L., Cox G., Collins A.S., Wolff K., George C., 2020. Cambro-Ordovician magmatism in the Delamerian orogeny: Implications for tectonic development of the southern Gondwanan margin. Gondwana Research, 81:490-521

Hart S.R., Dunn T., 1993. Experimental cpx/melt partitioning of 24 trace elements. Contributions to Mineralogy and Petrology, 113:1-8

Hermann J., Spandler C., Hack A., Korsakov A.V., 2006. Aqueous fluids and hydrous melts in high-pressure rocks: Implications for element transfer in subduction zone. Lithos, 92:399-417

Holland T., Blundy J., 1994. Non-ideal interactions in calcic amphiboles and their bearing on amphibole-plagioclase thermometry. Contributions to Mineralogy and Petrology, 116:433-447

Jeffries T.E., Jackson S.E., Longerich H.P., 1998. Application of a frequency quintupled Nd:YAG source (λ=213 nm) for laser ablation inductively coupled plasma mass spectrometric analysis of minerals. Journal of Analytical Atomic Spectrometry, 13:935-940

Jianping L., Kornprobst J., Vielzeuf D., 1995. An improved experimental calibration of the olivine-spinel geothermometer. Chinese Journal of Geochemistry, 14:68-77

Kelemen P.B., 1995. Genesis of high Mg# andesites and the continental crust. Contributions to Mineralogy and Petrology, 120:1-19

Kuiper K.F., Deino A., Hilgen F.J., Krijgsman W., Renne P.R., Wijbrans J.R., 2008. Synchronizing the rock clocks of Earth history. Science, 320:500-504

Leake B.E., Woolley A.R., Arps C.E., Birch W.D., Gilbert M.C., Grice J.D., Hawthorne F.C., Kato A., Kisch H.J., Krivovichev V.G., Linthout K., Laird J., Mandarino J., Maresch W.V., Nickel E.H., Tock N.M.S., Schumacher J.C., Smith D.C., Stephenson N.C.N., Ungaretti L., Whittaker E.J.W., Youzhi G., 1997. Nomenclature of amphiboles; report of the Subcommittee on

Amphiboles of the International Mineralogical Association Commission on new minerals and mineral names. Mineralogical Magazine, 61 (405):295-310

Li H., Arculus R.J., Ishizuka O., Hicjey-Vargas R., Yogodzinski G.M., McCarthy A., Kusano Y., Brandl P.A., Savov I.P., Tepley F.J., Sun W., 2021. Basalt derived from highly refractory mantle sources during early Izu-Bonin-Mariana arc development. Nature Communications, 12:1723

Liang Y., Sun C., Yao L., 2013. A REE-in-two-pyroxene thermometer for mafic and ultramafic rocks. Geochimica et Cosmochimica Acta, 102:246-260

Lin K.-Y., Wang K.-L., Chung S.-L., Bingöl A.F., Iizuka Y., Lee H.Y., 2020. Tracking the magmatic response to subduction initiation in the forearc mantle wedge: Insights from peridotite geochemistry of the Guleman and Kızıldağ ophiolites, Southeastern Turkey. Lithos, 376-377

Manning C.E., 2004. The chemistry of subduction zone fluids. Earth and Planetary Science Letters, 223:1-16

Marchesi C., Garrido C.J., Godard M., Belley F., Ferré E., 2009. Migration and accumulation of ultra-depleted subduction-related melts in the Massif du Sud ophiolite (New Caledonia). Chemical Geology, 266:171-186

Min K., Mundil R., Renne P.R., Ludwig K.R., 2000. A test for systematic errors in 40Ar/39Ar geochronology through comparison with U–Pb analysis of a 1.1 Ga rhyolite. Geochimica et Cosmochimica Acta, 64:73-98

Morishita T., Arai S., Green D.H., 2003. Evolution of low-Al orthopyroxene in the Horoman peridotite, Japan: an unusual indicator of metasomatzing fluids. Journal of Petrology, 44:1237-1246

Müntener O., Kelemen P.B., Grove T.L., 2001. The role of H2O during crystallization of primitive arc magmas under uppermost mantle conditions and genesis of igneous pyroxenites: an experimental study. Contributions to Mineralogy and Petrology, 141:643-658

Nekvasil H., Dondolini A., Horn J., Filiberto J., Long H., Lindsley D.H., 2004. The Origin and Evolution of Silica-saturated Alkalic Suites: an Experimental Study. Journal of Petrology, 45:693-721

Nicolas A., 1989. Structure of Ophiolites and Dynamics of Oceanic Lithosphere. Kluwer, Dordrecht, p. 367

Pearce J.A., 1982. Trace element characteristics of lavas from destructive plate boundaries. In: Thorpe, R.S. ed., Orogenic andesites and related rocks, Chichester, England: John Wiley and Sons, 528-548

Pearce J.A., Lippard S.J., Roberts S., 1984. Characteristics and tectonic significance of supra-subduction zone ophiolites. Geological Society, London, Special Publications, 16:77-94

Pearce J.A., Reagan M.K., 2019. Identification, classification, and interpretation of boninites from Anthropocene to Eoarchean using Si-Mg-Ti systematics. Geosphere, 15:1008-1037

Pirard C., Hermann J. and O'Neill H.ST.C., 2013. Petrology and Geochemistry of the Crust-Mantle Boundary in a Nascent Arc, Massif du Sud Ophiolite, New Caledonia, SW Pacific. Journal of Petrology, 54:1759-1792

Price A.A., Jackson M.G., Blichert-Toft J., Blusztajn J., Conatser C.S., Konter J.G., Koppers A.A.P., Kurz M.D., 2016. Geochemical evidence in the northeast Lau Basin for subduction of the Cook-Austral volcanic chain in the Tonga Trench. Geochemistry, Geophysics, Geosystems, 17:1694-1724

Prinzhofer A., Nicolas A., 1980. The Bogota peninsula, New Caledonia: a possible oceanic transform fault. The Journal of Geology, 88:387-398

Prouteau G., Scaillet B., Pichavant M., Maury R., 2001. Evidence for mantle metasomatism by hydrous silicic melts derived from subducted oceanic crust. Nature, 410:197-200

Reagan M.K., Heaton D.E., Schmitz M.D., Pearce J.A., Shervais J.W., Koppers A.A.P., 2019. Forearc ages reveal extensive short-lived and rapid seafloor spreading following subduction initiation. Earth and Planetary Science Letters, 506:520-529

Rogkala A., Petrounias P., Tsikouras B., Hatzipanagiotou K., 2017. New Occurrence of Pyroxenites in the Veria-Naousa Ophiolite (North Greece): Implications on Their Origin and Petrogenetic Evolution. Geosciences, 7,92

Schaen A.J., Jicha B.R., Hodges K.V., Vermeesch P., Stelten M.E., Mercer C.M., Phillips D., Rivera T.A., Jourdan F., Matchan E.L., Hemming S.R., Morgan L.E., Kelley S.P., Cassata W.S., Heizler M.T., Vasconcelos P.M., Koppers A.A.P., Mark D.F., Niespolo E.M., Sprain,C.J., Benowitz J.A., Hames W.E., Kuiper K.F., Turrin B.D., Renne P.R., Ross J., Nomade S., Guillou H., Laura E., Webb L.E., Cohen B.A., Calvert A.T., Joyce N., Morgan Ganderød M., Wijbrans J., Ishizuka, O., He H., Ramirez A., Pfänder J.A., Lopez-Martínez M., Huaning Qiu H., Brad S. Singer B.S., 2020.

On the reporting and interpretation of 40Ar/39Ar geochronologic data, Geological Society America Bullettin, 133(3-4):461-487

Schiano P., Clocchiatti R., Shimizu N., Maury R.C., Jochum K.P., Hofmann A.W., 1995. Hydrous silica-rich melts in the sub-arc mantle and their relationships with erupted arc lavas. Nature, 377:595-600

Secchiari A., Montanini A., Bosch D., Macera P., Cluzel D., 2016. Melt extraction and enrichment processes in the New Caledonia lherzolites: Evidence from geochemical and Sr–Nd isotope data. Lithos, 260:28-43

Secchiari A., Montanini A., Bosch D., Macera P., Cluzel D., 2018. The contrasting geochemical message from the New Caledonia gabbronorites: insights on depletion and contamination processes of the sub-arc mantle in a nascent arc setting. Contributions to Mineralogy and Petrology, 173:66

Secchiari A., Montanini A., Bosch D., Macera P., Cluzel D., 2020. Sr, Nd, Pb and trace element systematics of the New Caledonia harzburgites: Tracking source depletion and contamination processes in a SSZ setting. Geoscience Frontiers, 11:37-55

Soret M., Agard P., Dubacq B., Vitale-Brovarone A., Monié P., Chauvet A., Whitechurch H., Villemant B., 2016. Strain localization and fluid infiltration in the mantle wedge during subduction initiation: Evidence from the base of the New Caledonia ophiolite. Lithos, 244:1-19

Steiger R.H., Jäger E., 1977. Subcommission on geochronology: Convention on the use of decay constants in geo- and cosmochronology. Earth and Planetetary Science Letters, 36:359-362

Stern R.J., 2002. Subduction zones. Reviews of Geophysics, 40:1-42

Stern C.R., Kilian R., 1996. Role of the subducted slab, mantle wedge and continental crust in the generation of adakites from the Andean Austral Volcanic Zone. Contributions to Mineralogy and Petrology, 123:263-281

Sun C., Liang Y., 2017. A REE-in-plagioclase-clinopyroxene thermometer for crustal rocks. Contributions to Mineralogy and Petrology, 172:24

Tamura A., Arai S., 2006. Harzburgite–dunite–orthopyroxenite suite as a record of supra-subduction zone setting for the Oman ophiolite mantle. Lithos, 90:43-56

Taylor J.R., 1982. An Introduction to Error Analysis: The Study of Uncertainties in Physical Measurements. University Science Books, Mill Valley, California, 270 p

Taylor W.R., 1998. An experimental test of some geothermometer and geobarometer formulations for upper mantle peridotites with application to the thermobarometry of fertile lherzolite and garnet websterite. Neues Jb Miner Abh, 172: 381-408

Teyssier C., Chatzaras V., Von Der Handt A., 2016. Microfabrics in depleted mantle plaeotransform (New Caledonia). Geophysical Research Abstracts, EGU2016-11489, 18

Tilhac R., Ceuleneer G., Griffin W.L., O'Reilly S.Y., Pearson N.J., Benoit M., Henry H., Girardeau J., Grégoire M., 2016. Primitive Arc Magmatism and Delamination: Petrology and Geochemistry of Pyroxenites from the Cabo Ortegal Complex, Spain. Journal of Petrology, 57:1921-1954

Titus S.J., Maes S.M., Benford B., Ferré E.C., Tikoff B., 2011. Fabric development in the mantle section of a paleotransform fault and its effect on ophiolite obduction, New Caledonia. Lithosphere, 3:221-244

Ulrich M., Picard C., Guillot S., Chauvel C., Cluzel D., Meffre S., 2010. Multiple melting stages and refertilization as indicators for ridge to subduction formation: The New Caledonia ophiolite. Lithos, 115:223-236

van de Lagemaat S.H.A., van Hinsbergen D.J.J., Boschman L.M., Kamp P.J.J., Spakman W., 2018. Southwest Pacific Absolute Plate Kinematic Reconstruction Reveals Major Cenozoic Tonga-Kermadec Slab Dragging. Tectonics, 37:2647-2674

Varfalvy V., Hébert R., Bédard J.H., Laflèche M.R., 1997. Petrology and geochemistry of pyroxenite dykes in upper mantle peridotites of the North Arm mountain massif, Bay of Islands ophiolite, Newfoundland: implications for the genesis of boninitic and related magmas. The Canadian Mineralogist, 35:543-570

Villa I.M., Grobéty B., Kelley S.P., Trigila R., Wieler R., 1996. Assessing Ar transport paths and mechanisms for McClure Mountains Hornblende. Contributions to Mineralogy and Petrology, 126:67-80

Vogt J., Podvin P., 1983. Carte Géologique à l'échelle du 1 / 50 000 et notice explicative: feuille Humboldt-Port-Bouquet. Territoire de Nouvelle-Calédonie-Bureau de Recherches Géologiques et Minières, 1-68

Whattam S.A., Stern R.J., 2011. The ‘subduction initiation rule’: a key for linking ophiolites, intra-oceanic forearcs, and subduction initiation. Contributions to Mineralogy and Petrology, 162:1031-1045

Whitney D.L., Evans B.W., 2010. Abbreviations for names of rock-forming minerals. American Mineralogist, 95:185-187

Wood B.J., Blundy J.D., 1997. A predictive model for rare earth element partitioning between clinopyroxene and anhydrous silicate melt. Contributions to Mineralogy and Petrology, 129:166-181

Xu Y., Liu C.-Z., Lin W. 2021a. Melt extraction and reaction in the forearc mantle: Constraints from trace elements and isotope geochemistry of ultra-refractory peridotites of the New Caledonia Peridotite Nappe. Lithos, 380-381

Xu Y., Liu C.-Z., Shi X.-.F., Lin W., 2021b. Petrogenesis of Eocene mafic and felsic magmas in the New Caledonia ophiolite: geochemistry and geochronology constraints. International Geology Review

Zhao J.-H., Asimow P.D., 2014. Neoproterozoic boninite-series rocks in South China: A depleted mantle source modified by sediment-derived melt. Chemical Geology, 388:98-111

Zheng Y.-F., 2019. Subduction zone geochemistry. Geoscience Frontiers, 10:1223-1254

4.13. Tables

Table 4.1. Average major element compositions (wt%) of mineral phases from Ouassé samples. Digits in blue italics refer to the standard deviation.

	n° analysis	SiO_2	TiO_2	Al_2O_3	Cr_2O_3	FeO	MnO	MgO	CaO	Na_2O	K_2O	P_2O_5	NiO	Mg#	Cr#	An
OU2 Harzburgite																
Ol pfc core	6	41.41	bdl	bdl	bdl	8.04	0.11	50.71	bdl	bdl	bdl	bdl	0.50	92	-	-
		0.26		-	-	*0.21*	*0.06*	*0.42*	-	-	-	-	*0.05*	*0.23*	-	-
Ol pfc rim	4	41.68	bdl	bdl	bdl	8.07	0.16	51.02	bdl	bdl	bdl	bdl	0.51	92	-	-
		0.06		-	-	*0.07*	*0.08*	*0.37*	-	-	-	-	*0.14*	*0.09*	-	-
Opx pfc core	12	57.58	bdl	1.57	0.69	5.39	0.14	34.95	0.75	bdl	bdl	bdl	bdl	92	-	-
		0.34		*0.15*	*0.11*	*0.08*	*0.08*	*0.20*	*0.15*	-	-	-	-	*0.10*	-	-
Opx pfc rim	8	57.99	bdl	1.23	0.45	5.43	0.16	35.33	0.56	bdl	bdl	bdl	bdl	92	-	-
		0.39		*0.08*	*0.09*	*0.17*	*0.05*	*0.28*	*0.08*	-	-	-	-	*0.21*	-	-
Spl pfc		bdl	bdl	22.77	42.63	22.17	0.41	10.40	bdl	bdl	bdl	bdl	0.17	46	56	-
		-		*0.61*	*0.51*	*0.10*	*0.09*	*0.16*	-	-	-	-	*0.12*	*0.44*	*0.93*	-
Ol neo	6	41.98	bdl	bdl	bdl	7.83	0.16	51.65	bdl	bdl	bdl	bdl	0.42	92	-	-
		0.21		-	-	*0.25*	*0.09*	*0.41*	-	-	-	-	*0.16*	*0.28*	-	-
Opx neo	6	57.73	bdl	1.36	0.55	5.48	0.15	35.35	0.65	bdl	bdl	bdl	bdl	92	-	-
		0.50		*0.11*	*0.08*	*0.17*	*0.10*	*0.32*	*0.12*	-	-	-	-	*0.21*	-	-
Spl neo	5	bdl	bdl	24.10	41.59	21.94	0.37	10.55	bdl	bdl	bdl	bdl	bdl	46	54	-
		-		*1.34*	*1.27*	*0.54*	*0.19*	*0.30*	-	-	-	-		*1.30*	*2.12*	-
Cpx neo at opx rim	1	54.24	bdl	1.49	0.84	1.97	bdl	17.84	23.67	bdl	bdl	bdl	bdl	94	-	-
OU3 Harzburgite																
Ol pfc core	3	41.22	bdl	bdl	bdl	8.38	0.12	51.35	bdl	bdl	bdl	bdl	0.44	92	-	-
		0.25	-	-	-	*0.16*	*0.05*	*0.33*	-	-	-	-	*0.06*	*0.19*	-	-
Ol pfc rim		41.09	bdl	bdl	bdl	8.27	0.13	51.28	bdl	bdl	bdl	bdl	0.62	92	-	-
		0.09		-	-	*0.15*	*0.08*	*0.14*	-	-	-	-	*0.09*	*0.12*	-	-
Opx pfc core	6	57.59	bdl	1.42	0.59	5.54	0.15	35.46	0.81	bdl	bdl	bdl	bdl	92	-	-
		0.43		*0.11*	*0.02*	*0.10*	*0.10*	*0.31*	*0.23*	-	-	-	-	*0.13*	-	-
Opx pfc rim	6	57.83	0.10	1.33	0.49	5.62	0.19	35.67	0.78	bdl	bdl	bdl	bdl	92	-	-
		0.36	*0.01*	*0.19*	*0.09*	*0.25*	*0.06*	*0.39*	*0.41*	-	-	-	-	*0.28*	-	-
Spl pfc core	6	bdl	bdl	17.83	48.81	19.58	0.51	11.78	bdl	bdl	bdl	bdl	bdl	52	65	-
		-		*1.22*	*0.65*	*0.53*	*0.05*	*0.18*	-	-	-	-	-	*0.94*	*0.69*	-
Spl pfc rim	6	bdl	bdl	19.92	46.62	19.36	0.40	12.12	bdl	bdl	bdl	bdl	bdl	53	61	-
		-		*1.41*	*1.36*	*0.52*	*0.07*	*0.31*	-	-	-	-	-	*1.27*	*2.36*	-
Ol neo	6	41.34	bdl	bdl	bdl	8.17	0.17	51.52	bdl	bdl	bdl	bdl	0.42	92	-	-
		0.23		-	-	*0.18*	*0.07*	*0.40*	-	-	-	-	*0.13*	*0.18*	-	-
Opx neo core	6	57.59	bdl	1.21	0.46	5.61	bdl	35.56	0.71	bdl	bdl	bdl	bdl	92	-	-
		0.24		*0.17*	*0.12*	*0.16*		*0.28*	*0.26*	-	-	-	-	*0.20*	-	-
Opx neo rim	2	58.26	0.11	0.96	0.42	5.23	0.14	35.55	0.55	bdl	bdl	bdl	bdl	93	-	-
		0.11	-	*0.03*	-	-	*0.01*	*1.19*	*0.03*	-	-	-	-	*0.04*	-	-
Spl neo		bdl	bdl	23.43	42.05	22.53	0.41	10.21	bdl	bdl	bdl	bdl	bdl	45	55	-
		-	-	*0.37*	*0.62*	*0.18*	*0.06*	*0.02*	-	-	-	-	-	*0.26*	*0.76*	-
Cpx neo	2	55.12	bdl	1.05	0.47	1.97	0.16	18.65	23.51	bdl	bdl	bdl	bdl	94	-	-
		0.01		*0.05*	*0.08*	*0.09*	*0.03*	*0.03*	*0.04*	-	-	-	-	*0.24*	-	-

OU7A Harzburgite																
Ol pfc	7	40.34	bdl	bdl	bdl	8.94	bdl	50.52	bdl	bdl	bdl	bdl	0.49	91	-	-
		0.36		-	-	*0.22*		*0.28*	-	-	-	-	*0.08*	*0.19*	-	-
Opx pfc core	2	56.46	bdl	1.84	0.77	5.58	0.17	35.04	0.64	bdl	bdl	bdl	bdl	92	-	-
		0.22	-	*0.12*	*0.10*	*0.16*	*0.12*	*0.18*	*0.11*	-	-	-	-	*0.25*	-	-
Opx pfc rim	4	56.17	bdl	1.55	0.59	5.91	0.10	34.98	0.61	bdl	bdl	bdl	bdl	91	-	-
		0.19		*0.33*	*0.22*	*0.05*	*0.12*	*0.29*	*0.11*	-	-	-	-	*0.10*	-	-
Spl pfc core	4	bdl	bdl	20.75	45.36	24.54	0.32	8.99	bdl	bdl	bdl	bdl	bdl	39	59	-
		-		*0.34*	*0.95*	*0.29*	*0.17*	*0.38*	-	-	-	-	-	*1.04*	*0.25*	-
Spl pfc rim	3	bdl	bdl	21.47	44.06	24.64	0.37	8.81	bdl	bdl	bdl	bdl	bdl	39	58	-
		-		*0.84*	*0.93*	*0.15*	*0.15*	*0.36*	-	-	-	-	-	*0.82*	*1.20*	-
Ol neo	2	40.75	bdl	bdl	bdl	9.21	0.11	50.35	bdl	bdl	bdl	bdl	0.51	91	-	-
		0.37		-	-	*0.08*	*0.06*	*0.57*	-	-	-	-	-	*0.02*	-	-
Opx neo	2	57.15	bdl	1.28	0.35	6.34	0.18	35.24	0.67	bdl	bdl	bdl	bdl	91	-	-
		0.49		*0.07*	-	*0.05*	*0.04*	*0.48*	*0.01*	-	-	-	-	*0.19*	-	-
Amp neo	2	48.72	0.18	9.88	2.03	3.38	bdl	20.31	12.05	2.00	bdl	bdl	bdl	91	-	-
		1.17	-	*0.96*	*0.07*	*0.22*		*0.58*	*0.06*	*0.10*	-	-	-	*0.73*	-	-
OU1 Amp-websterite																
Opx core	4	54.52	bdl	1.09	bdl	13.89	0.32	29.11	0.83	bdl	bdl	bdl	bdl	79	-	-
		0.60		*0.05*	-	*0.09*	*0.07*	*0.35*	*0.06*	-	-	-	-	*0.12*	-	-
Opx rim	4	54.96	bdl	0.96	bdl	13.82	0.37	29.35	0.72	bdl	bdl	bdl	bdl	79	-	-
		0.15		*0.12*	-	*0.21*	*0.05*	*0.32*	*0.11*	-	-	-	-	*0.11*	-	-
Opx granoblastic assemblage	2	54.91	bdl	1.04	bdl	14.05	0.42	29.17	0.86	bdl	bdl	bdl	bdl	79	-	-
		0.74		*0.16*	-	*0.12*	*0.04*	*0.43*	*0.05*	-	-	-	-	*0.39*	-	-
Cpx core	8	53.44	0.14	1.43	bdl	5.60	0.22	16.79	21.95	0.24	bdl	bdl	bdl	84	-	-
		0.47	*0.07*	*0.50*	-	*0.68*	*0.07*	*0.27*	*0.68*	*0.08*	-	-	-	*1.67*	-	-
Cpx rim	5	53.53	0.17	1.74	bdl	5.78	0.16	16.78	22.14	0.30	bdl	bdl	bdl	84	-	-
		0.28	*0.02*	*0.12*	-	*0.15*	*0.03*	*0.28*	*0.14*	*0.06*	-	-	-	*0.51*	-	-
Cpx granoblastic assemblage	2	53.50	bdl	1.50	bdl	5.46	0.19	16.48	21.92	bdl	bdl	bdl	bdl	84	-	-
		0.26	-	*0.04*	-	*0.07*	*0.04*	*0.03*	*0.31*	-	-	-	-	*0.14*	-	-
Amp core	6	46.49	1.01	10.24	0.64	8.51	0.14	17.29	11.46	1.92	0.21	bdl	bdl	78	-	-
		0.98	*0.05*	*0.43*	*0.11*	*0.17*	*0.05*	*0.35*	*0.17*	*0.19*	*0.04*	-	-	*0.51*	-	-
Amp rim	3	46.93	1.04	10.20	0.35	7.96	0.11	17.60	11.63	1.93	0.20	bdl	bdl	80	-	-
		0.48	*0.08*	*0.47*	-	*0.24*	*0.08*	*0.30*	*0.18*	*0.12*	*0.02*	-	-	*0.71*	-	-
Pl	6	45.65	bdl	34.93	bdl	0.33	0.13	bdl	16.12	1.68	bdl	bdl	bdl	-	-	84
		0.34	-	*0.38*	-	-	-	-	*0.37*	*0.18*	-	-	-	-	-	*1.73*
Spl included in amp	2	bdl	2.30	8.40	25.10	60.84	0.27	2.90	bdl	bdl	bdl	bdl	bdl	7.8	67	-
		-	*0.01*	*0.26*	*0.01*	*0.04*	*0.16*	*0.11*	-	-	-	-	-	*0.28*	*0.68*	-
OU4 Amp-websterite										-						
Opx core	4	55.43	bdl	0.90	0.36	10.90	0.37	31.16	0.75	bdl	bdl	bdl	bdl	84	-	-
		0.21		*0.01*	*0.03*	*0.35*	*0.12*	*0.38*	*0.08*	-	-	-	-	*0.48*	-	-
Opx rim	4	55.79	bdl	0.92	0.22	10.87	0.17	31.39	0.72	bdl	bdl	bdl	bdl	84	-	-
		0.28		*0.09*	*0.01*	*0.10*	*0.02*	*0.25*	*0.05*		-	-	-	*0.19*	-	-
Opx granoblastic assemblage	4	56.05	bdl	1.11	0.27	10.91	0.21	31.32	0.78	bdl	bdl	bdl	bdl	84	-	-
		0.50		*0.10*	*0.10*	*0.18*	*0.07*	*0.14*	*0.07*	-	-	-	-	*0.24*	-	-
Cpx core	4	54.36	0.13	1.57	bdl	4.21	0.12	17.35	22.47	0.29	bdl	bdl	bdl	88	-	-

		0.23	*0.04*	*0.08*	-	*0.08*	*0.06*	*0.20*	*0.27*	*0.16*	-	-	-	*0.12*	-	-
Cpx rim	2	53.95	0.14	1.61	bdl	4.23	0.12	17.27	21.86	0.29	bdl	bdl	bdl	88	-	-
		0.04	*0.14*	*0.10*	-	*0.44*	*0.03*	*0.14*	*0.23*	*0.09*	-	-	-	*1.01*	-	-
Cpx granoblastic assemblage	4	54.04	0.19	1.38	0.35	4.05	bdl	17.20	22.48	0.30	bdl	bdl	bdl	88	-	-
		0.45	*0.03*	*0.07*	-	*0.02*		*0.21*	*0.22*	*0.08*	-	-	-	*0.16*	-	-
Amp	2	48.46	0.75	9.03	0.68	5.95	bdl	19.13	11.71	1.58	0.23	bdl	bdl	85	-	-
		0.19	*0.01*	*0.31*	*0.02*	*0.14*		*0.00*	*0.01*	*0.01*	*0.01*	-	-	*0.31*	-	-
Spl included in opx	1	bdl	0.65	11.64	45.83	33.86	0.21	5.47	bdl	bdl	bdl	bdl	bdl	22	73	-
OU5A Orthopyroxenite																
Opx core	5	56.24	bdl	1.89	0.91	6.25	0.17	34.29	0.64	bdl	bdl	bdl	bdl	91	-	-
		0.28		*0.07*	*0.12*	*0.15*	*0.06*	*0.37*	*0.09*	-	-	-	-	*0.16*	-	-
Opx rim	6	56.18	bdl	1.75	0.75	6.20	0.18	34.36	0.50	bdl	bdl	bdl	bdl	91	-	-
		0.33		*0.09*	*0.18*	*0.10*	*0.05*	*0.25*	*0.05*	-	-	-	-	*0.17*	-	-
Opx core granoblastic assemblage	6	55.77	bdl	1.93	0.78	6.14	0.14	34.08	0.69	bdl	bdl	bdl	bdl	91	-	-
		0.56		*0.11*	*0.09*	*0.15*	*0.06*	*0.41*	*0.17*		-	-	-	*0.12*	-	-
Opx rim granoblastic assemblage	2	56.53	0.10	1.74	0.62	6.29	0.22	34.58	0.58	bdl	bdl	bdl	bdl	91	-	-
		1.14	-	*0.17*	*0.08*	*0.12*	*0.02*	*0.82*	*0.04*	-	-	-	-	*0.36*	-	-
Cpx granoblastic assemblage	3	53.34	0.11	2.36	1.32	2.22	bdl	17.27	22.65	0.46	bdl	bdl	bdl	93	-	-
		0.43	*0.06*	*0.16*	*0.26*	*0.05*		*0.19*	*0.18*	*0.03*	-	-	-	*0.08*	-	-
Amp	3	48.26	0.38	10.10	2.08	2.91	bdl	20.30	12.06	1.88	0.17	bdl	bdl	93	-	-
		0.29	*0.02*	*0.30*	*0.21*	*0.11*		*0.16*	*0.15*	*0.03*	*0.04*	-	-	*0.29*	-	-
Spl	2	bdl	0.12	21.17	44.91	21.30	0.43	10.46	bdl	bdl	bdl	bdl	bdl	47	59	-
		-	*0.05*	*1.70*	*1.99*	*0.25*	*0.11*	*0.74*	-	-	-	-	-	*2.06*	*3.03*	-
OU7B Amp-websterite																
Opx core	2	55.78	bdl	1.04	0.14	9.79	0.28	31.22	0.85	bdl	bdl	bdl	bdl	85	-	-
		0.42	-	*0.21*	-	*1.01*	*0.04*	*0.90*	*0.04*	-	-	-	-	*1.68*	-	-
Opx rim	3	57.09	0.18	bdl	bdl	7.84	0.15	34.02	0.17	bdl	bdl	bdl	bdl	89	-	-
		0.17	-	-	-	*0.14*	*0.04*	*0.22*	*0.06*		-	-	-	*0.21*	-	-
Cpx core	3	54.08	0.19	1.47	bdl	3.95	0.16	17.64	22.19	0.22	bdl	bdl	bdl	89	-	-
		0.20	*0.07*	*0.10*		*0.25*	*0.12*	*0.56*	*0.93*	*0.08*	-	-	-	*0.31*	-	-
Cpx rim	2	54.48	bdl	0.60	bdl	3.73	0.20	16.70	23.99	0.25	bdl	bdl	bdl	89	-	-
		0.82	-	-	-	*0.19*	*0.06*	*0.82*	*1.30*	*0.03*	-	-	-	*0.98*	-	-
Amp	18	49.14	0.75	9.63	0.14	5.68	0.12	19.19	11.93	1.84	0.20	bdl	bdl	86	-	-
		0.79	*0.21*	*0.93*	*0.08*	*0.25*	*0.06*	*0.62*	*0.35*	*0.21*	*0.04*	-	-	*0.84*	-	-
Apt	2	bdl	bdl	bdl	bdl	bdl	bdl	bdl	57.27	bdl	bdl	42.83	bdl	-	-	-
		-	-	-	-	-	-	-	*1.36*	-	-	*0.91*	-	-	-	-
OU8 Orthopyroxenite																
Opx core	4	56.26	bdl	1.68	0.73	5.31	0.12	34.98	0.49	bdl	bdl	bdl	bdl	92	-	-
		1.15		*0.11*	*0.14*	*0.12*	*0.04*	*0.32*	*0.07*	-	-	-	-	*0.16*	-	-
Opx rim	5	56.05	0.10	1.50	0.69	5.24	0.14	34.92	0.75	bdl	bdl	bdl	bdl	92	-	-
		0.60	*0.02*	*0.84*	*0.10*	*0.12*	*0.06*	*0.27*	*0.09*	-	-	-	-	*0.12*	-	-
Ol	7	40.77	bdl	bdl	bdl	7.90	0.14	51.10	bdl	bdl	bdl	bdl	0.54	92	-	-
		0.31	-	-	-	*0.13*	*0.07*	*0.38*	-	-	-	-	*0.06*	*0.14*	-	-
Spl	4	bdl	bdl	26.27	42.77	16.05	0.38	13.45	bdl	bdl	bdl	bdl	bdl	60	52	-
		-		*1.26*	*1.13*	*1.12*	*0.06*	*1.07*	-	-	-	-	-	*3.55*	*1.84*	-

bdl = below detection limits

Table 4.2. Bulk rock major and trace element compositions of Ouassé peridotites and pyroxenites. Major element compositions are calculated on anhydrous basis and normalized to 100. Major elements are expressed in wt%, trace elements in ppm.

Sample	OU2	OU3	OU7A	OU1	OU4	OU5A	OU7B	OU8
Rock type	Harzburgite	Harzburgite	Harzburgite	Amp-websterite	Amp-websterite	Orthopyroxenite	Amp-websterite	Orthopyroxenite
SiO_2	44.19	43.92	45.03	51.16	55.18	56.51	53.37	55.54
TiO_2	0.002	0.001	0.002	0.16	0.11	0.03	0.33	0.004
Al_2O_3	0.47	0.41	0.52	7.07	1.34	2.07	4.06	1.96
FeO	7.42	7.74	7.69	8.17	9.28	6.02	5.74	5.57
MnO	0.12	0.12	0.12	0.18	0.20	0.14	0.12	0.12
MgO	47.28	47.24	46.15	20.93	26.69	33.31	24.91	35.69
CaO	0.49	0.54	0.42	11.58	7.07	1.81	10.62	1.06
Na_2O	0.02	0.02	0.07	0.72	0.13	0.10	0.73	0.06
K_2O	bdl	bdl	bdl	0.02	bdl	bdl	0.05	bdl
P_2O_5	bdl	bdl	bdl	bdl	bdl	bdl	0.06	bdl
LOI	7.69	7.41	8.80	3.03	0.22	1.20	3.07	5.62
Mg#	92	92	91	82	84	91	89	92
Sc	6.00	7.00	6.00	56.00	47.00	20.00	51.00	16.00
V	24.00	24.00	22.00	127.00	118.00	95.00	218.00	83.00
Cr	2550	2160	2450	600	1170	6000	460	5650
Co	102.00	106.00	105.00	57.00	73.00	67.00	48.00	65.00
Ni	2260	2400	2380	360	450	960	800	2890
Cu	bdl	bdl	bdl	20.00	10.00	10.00	30.00	bdl
Zn	40.00	40.00	40.00	50.00	70.00	50.00	40.00	40.00
Ga	1.00	1.00	1.00	6.00	3.00	2.00	6.00	2.00
Ge	0.70	0.80	0.80	1.60	1.80	1.70	1.50	1.50
Sr	9.00	17.00	2.00	178.00	10.00	3.00	26.00	bdl
Y	bdl	bdl	bdl	4.10	2.50	0.50	7.70	bdl
Zr	2.00	1.00	2.00	8.00	4.00	3.00	27.00	2.00
Nb	bdl	bdl	bdl	bdl	bdl	bdl	0.60	bdl

Ba	bdl	bdl	bdl	6.00	bdl	bdl	3.00	4.00
La	bdl	bdl	bdl	0.35	0.18	bdl	2.73	bdl
Ce	bdl	bdl	0.13	1.36	0.72	0.10	8.62	bdl
Pr	bdl	bdl	0.02	0.28	0.16	0.02	1.47	bdl
Nd	bdl	bdl	0.06	1.79	0.99	0.08	6.99	bdl
Sm	bdl	bdl	0.03	0.69	0.42	0.03	1.92	bdl
Eu	bdl	bdl	bdl	0.24	0.11	0.01	0.45	bdl
Gd	bdl	bdl	bdl	0.81	0.48	0.03	1.67	bdl
Tb	bdl	bdl	bdl	0.13	0.08	0.01	0.25	bdl
Dy	bdl	bdl	0.02	0.81	0.52	0.07	1.42	bdl
Ho	bdl	bdl	bdl	0.16	0.10	0.02	0.27	bdl
Er	bdl	bdl	0.01	0.42	0.26	0.05	0.78	0.01
Tm	bdl	bdl	bdl	0.06	0.04	0.01	0.11	bdl
Yb	bdl	bdl	0.01	0.36	0.23	0.09	0.72	0.01
Lu	bdl	bdl	0.003	0.06	0.04	0.02	0.11	0.002
Hf	bdl	bdl	bdl	0.30	0.10	bdl	0.80	bdl
Ta	bdl	0.07	0.17	bdl	bdl	bdl	0.06	bdl
W	bdl	bdl	3.90	bdl	bdl	bdl	bdl	bdl
Th	bdl	bdl	bdl	bdl	bdl	bdl	0.05	bdl
U	0.01	bdl	bdl	bdl	bdl	bdl	0.03	bdl
Mineral modal composition (vol%)	Ol = 78.10 Opx = 21.17 Spl = 0.63 Cpx = 0.1	Ol = 76.56 Opx = 22.99 Spl = 0.45	Ol = 69.38 Opx = 30.17 Spl = 0.45	Opx = 26.57 Cpx = 23.99 Amp = 40.72 Sec. min. = 5.2 Pl = 3.45	Opx = 67.53 Cpx = 27.52 Amp = 4.95	Opx = 94.44 Cpx = 5.38 Spl = 0.18	Opx = 40.94 Cpx = 26.79 Amp = 32.27	Opx = 95.05 Ol = 4.51 Spl = 0.44

LOI = Loss On Ignition

Mg# = [100 × Mg/(Mg+Fe_{tot})]

bdl = below detection limits

Table 4.3. Representative trace element compositions (ppm) of minerals from Ouassé pyroxenites.

Sample	OU1				OU4			OU5A			OU7B				OU8	
Rock type	Amp-websterite				Amp-websterite			Orthopyroxenite			Amp-websterite				Orthopyroxenite	
Mineral	Opx	Cpx	Amp	Pl	Opx	Cpx	Amp	Opx	Cpx	Amp	Opx	Cpx	Amp	Apt	Opx	Ol
Sc	27	90	115	3.58	23	89	125	20	62	71	6.33	68	73	16	14	1.88
Ti	649	1168	8711	41	442	904	7592	203	465	1781	144	638	6323	872	17	3.80
V	72	357	588	0.88	64	198	587	94	216	398	19	257	461	33	87	1.03
Cr	1007	706	1846	6.78	1329	1271	4216	5792	7729	11484	41	539	1167	148	4681	38
Co	101	39	65	0.45	92	37	69	68	36	49	70	32	48	6.56	61	164
Ni	433	312	557	1.45	526	290	753	934	646	1197	661	408	779	21	944	4179
Zn	128	30	45	2.73	89	21	40	38	15	18	39	19	33	165	36	42
Rb	0.14	0.08	0.31	bdl	bdl	0.10	0.36	0.12	0.09	0.60	0.20	0.05	0.24	31	0.04	0.04
Sr	0.18	20	67	690	0.16	25	63	0.46	17	21	0.34	28	56	669	0.11	0.14
Y	0.83	10	20	0.11	0.58	5.58	15	0.36	2.78	5.23	0.77	5.03	15	23	0.05	bdl
Zr	0.58	8.64	26	bdl	0.58	7.50	26	0.40	3.21	5.98	0.69	10	63	100	bdl	0.04
Nb	0.06	0.03	1.06	bdl	0.06	0.05	0.50	0.07	0.04	0.21	0.12	0.04	3.31	3.02	0.03	0.03
Cs	0.04	0.01	0.02	0.11	0.01	0.03	0.02	0.02	0.01	bdl	0.06	bdl	0.02	1.10	0.01	0.01
Ba	0.04	0.14	3.55	4.52	0.03	0.27	5.12	0.25	0.22	3.09	0.10	0.11	6.14	220	0.08	0.06
La	0.02	0.39	1.17	0.70	bdl	0.45	1.43	bdl	0.22	0.45	bdl	1.10	4.06	161	0.02	0.01
Ce	bdl	2.47	6.25	1.43	0.07	2.39	6.89	0.06	0.71	1.64	0.08	4.78	18	713	0.01	bdl
Pr	0.01	0.59	1.39	0.15	bdl	0.49	1.34	bdl	0.11	0.23	0.08	0.82	3.12	47	0.01	bdl
Nd	0.10	4.17	10	0.42	bdl	2.76	8.01	0.07	0.75	1.32	0.39	3.92	15	113	0.10	0.06
Sm	0.05	1.78	3.78	0.20	bdl	1.03	2.51	0.08	0.24	0.34	0.31	1.12	3.59	18	0.02	0.07
Eu	0.04	0.41	1.20	0.29	0.02	0.34	0.95	0.07	0.12	0.17	0.20	0.27	1.07	4.97	0.04	0.02
Gd	0.14	2.01	4.57	0.17	bdl	1.36	3.47	0.17	0.35	0.75	0.37	1.22	3.38	4.45	0.07	0.06
Tb	bdl	0.32	0.66	0.05	0.02	bdl	0.53	0.03	bdl	0.13	0.10	0.17	0.46	1.08	bdl	bdl
Dy	bdl	2.12	4.67	0.54	0.15	1.23	3.06	bdl	0.49	0.91	bdl	1.10	3.01	6.30	0.01	bdl
Ho	0.04	0.43	0.83	bdl	0.03	bdl	0.61	0.04	0.12	0.20	bdl	0.23	0.57	1.11	bdl	0.01
Er	0.15	1.08	2.19	0.31	0.12	0.67	1.45	bdl	0.34	0.55	0.34	bdl	1.65	5.36	0.07	0.05
Tm	bdl	0.16	0.31	0.12	bdl	0.10	0.23	0.02	bdl	0.10	0.07	0.09	0.22	bdl	0.01	bdl

Yb	0.22	0.94	2.04	bdl	0.12	0.61	1.54	0.16	bdl	0.54	bdl	0.56	1.39	bdl	0.12	0.08
Lu	0.05	0.13	0.24	0.02	0.02	0.09	0.20	0.02	0.04	0.08	0.09	0.08	0.20	1.10	0.01	bdl
Hf	0.15	0.49	1.32	1.08	0.04	0.42	1.01	0.07	0.18	0.15	0.52	0.32	2.38	3.54	0.29	bdl
Ta	0.01	0.02	0.07	0.02	bdl	0.04	0.07	0.02	0.03	0.01	0.07	0.01	0.19	1.75	bdl	0.02
Pb	0.10	0.05	0.10	0.40	0.02	0.09	0.07	0.04	0.06	bdl	bdl	0.06	0.11	25	0.03	0.03
Th	0.02	0.02	0.03	0.02	bdl	0.04	0.12	0.03	0.01	0.01	0.14	0.04	0.06	6.25	0.02	0.01
U	0.03	0.01	0.04	0.05	bdl	0.03	0.02	0.01	0.02	0.01	bdl	0.03	0.05	6.43	0.01	0.01

bdl = below detection limits

Table 4.4. Temperature estimates (°C) for Ouassé peridotites and pyroxenites. Calculations were made considering the core analysis of each grain and pressure conditions of 1 GPa.

	$T_{REE\text{-}Px}$[a]	$T_{REE\text{-}Cpx\text{-}Pl}$[b]	$T_{Ca\text{-}in\text{-}Opx}$[c]	T_{Ta98}[d]	T_{BK90}[c]	$T_{Amp\text{-}Pl}$[e]	$T_{Ol\text{-}Spl}$[f]	$T_{Ca\text{-}in\text{-}Ol}$[g]
Harzburgite OU2								
porphyroclast			956				747	
neoblast			923	883	892		721	
Harzburgite OU3								
porphyroclast			973					
neoblast			945	923	934		721	
Harzburgite OU7A								
porphyroclast			923				728	
Amp-websterite OU1								
medium- to coarse-grained pyroxenes	1251 ± 37		990	958	923			
granoblastic assemblage		1310 ± 14	997	992	946	970		
Amp-websterite OU4								
medium- to coarse-grained pyroxenes	1264 ± 50		965	941	927			
granoblastic assemblage	1249 ± 52		971	927	914			
Orthopyroxenite OU5A								
medium- to coarse-grained pyroxenes			924					
granoblastic assemblage			932	894	911			
Amp-websterite OU7B			993	970	965			
Orthopyroxenite OU8			869				865	861

[a]= Liang et al. (2013)

[b]= Sun and Liang (2017)

[c]= Brey and Köhler (1990)

[d]= Taylor 1998

[e]= Holland and Blundy (1994)

[f]= Jianping et al. (1995)

[g]= De Hoog et al. (2010)

Table 4.5. Summary of $^{40}Ar/^{39}Ar$ results for hornblende analysis

				Plateau Age					Isochron Age			Integrated age		
Sample	Irrad	min	Calculation	n	$\%^{39}Ar$	MSWD	Age(Ma)	± 1s	$^{40}Ar/^{36}Ar$ ± 1s	Age(Ma)	± 1s	n	Age(Ma)	± 1s
OU7B	NM-312A Hornblende		WMA	10	97.0	0.44	**56.05**	**± 0.17**	297.3 ± 4.4	55.87	± 0.47	12	56.57	± 0.24
OU1	NM-312A Hornblende		WMA	12	100.0	0.50	**56.01**	**± 0.19**	295.4 ± 0.8	56.03	± 0.22	12	55.98	± 0.30

Irradiation = NM-312A

WMA = Weighted mean age

Table 4.6. Trace elements compositions and Mg# values of calculated liquids in equilibrium with clinopyroxenes from Ouassé pyroxenites.

Sample	OU1	OU4	OU5A	OU7B
Rock type	Amp-websterite	Amp-websterite	Orthopyroxenite	Amp-websterite
Ti	3040	2355	1211	1662
V	115	64	70	87
Rb	448	566	491	253
Ba	212	352	565	162
Th	122	176	28	182
U	23	53	33	53
Nb	3.99	6.19	5.45	4.91
La	7.34	8.35	4.11	20
Ce	29	28	8.28	56
Pb	0.80	1.12	0.81	0.88
Pr	4.22	3.54	0.80	5.88
Sr	157	194	95	222
Nd	22	15	3.99	21
Sm	6.12	3.55	0.82	3.84
Zr	70	61	26	78
Hf	2.07	1.65	0.71	1.25
Eu	1.17	0.97	0.34	0.76
Gd	5.02	3.39	0.88	3.04
Dy	4.79	2.78	1.11	2.49
Y	21	12	5.96	11
Er	2.79	1.74	0.88	1.22
Yb	2.18	1.42	0.74	1.30
Lu	0.29	0.21	0.08	0.20
Sr/Y	7.38	16	16	21
La/Yb	3.36	5.88	5.53	16
Mg#	58	67	80	69

Chapter 5

5.1. Concluding remarks

The present PhD Thesis focused on mantle sequences from the External Ligurian and New Caledonia ophiolites. The External Ligurian ophiolites expose a lithospheric mantle of subcontinental origin that underwent a decompression evolution during the Mesozoic rifting stage that preceded the opening of the Jurassic Western Tethys basin. The New Caledonia ophiolites expose a lithospheric mantle of oceanic nature that experienced melt extraction in a forearc environment during the Late Eocene subduction phase. Despite these differences, both studied mantle sections are characterized by a variety of pyroxenite layers. In addition, large-scale lithospheric shear zones were detected both in the External Ligurian (Monte Sant'Agostino) and New Caledonia (Bogota Peninsula Shear Zone) ophiolites. The Monte Sant'Agostino shear zone accommodated the deformation of the subcontinental mantle during a rifting-related exhumation event. The Bogota Peninsula Shear Zone has been reinterpreted as a paleotransform fault developed during the subduction phase.

Besides the specific objectives of each case study, the results of the Thesis could be read in terms of the heterogeneities exhibited by the mantle sequences. Listed below some observations (abbreviations: EL = External Ligurian case study; NC = New Caledonia case study):

- EL: Considering the studied mantle bodies (Monte Gavi and Monte Sant'Agostino) and the others case studies reported in the literature, the Thesis has shown a heterogeneous rifting-related plagioclase-facies evolution, characterized by presence or absence of mylonitic to ultramylonitic deformation, and presence or absence of melt-rock reaction events.
- EL: The Monte Gavi mantle body documents the occurrence of a plagioclase-facies melt impregnation event in the late Triassic. The melt impregnation event recorded by the Monte Nero mantle body conversely most likely developed in the middle-late Jurassic. These age differences highlight the polyphase nature of the rifting-related mantle evolution, which presumably occurred in a time span of ~60 Ma.
- NC: The studied mantle sequence (near Ouassé, Bogota Peninsula) offers an extreme pyroxenite heterogeneity within few hundred meters. These pyroxenites provide evidence for: (i) the presence of compositionally diverse subduction-related magmas, and (ii) a variable geochemical contribution of the sinking slab in the forearc mantle.